Diss. ETH No. 27012

Secondary ion emission in MeV-SIMS

A thesis submitted to attain the degree of

Doctor of Sciences of ETH Zurich

(Dr. sc. ETH Zurich)

presented by

Klaus-Ulrich Miltenberger

MSc ETH Physics, ETH Zurich

born on 24.07.1991

citizen of the Federal Republic of Germany

accepted on the recommendation of

Prof. Dr. Hans-Arno Synal, examiner

Prof. Dr. Rainer Wallny, co-examiner

Prof. Dr. Primož Pelicon, co-examiner

Dr. Max Doebeli, co-examiner

2020

Contents

Abstract 1

Zusammefassung 3

Acknowledgements 5

1. Introduction 9

1.1. A comparison of imaging techniques for molecular sample characterization . . 9

1.2. The emergence of MeV-SIMS 11

1.3. Studying secondary ion desorption: a motivation 13

1.4. Outline and structure of the present work 14

2. Secondary ion emission in SIMS 17

2.1. Energy loss processes in matter 17

2.2. Secondary ion desorption mechanisms 20

2.3. Brief overview of theoretical models for sputtering 25

3. MeV-SIMS at ETH Zurich: The CHIMP setup 31

3.1. Layout of the TANDEM accelerator facility 31

3.2. Preparation of the primary ion beam 33

3.2.1. Collimation using a glass capillary 33

3.2.2. Collimation using micrometer apertures 36

3.3. Initial setup: Positive mass spectrometer with electron start 37

3.3.1. The measurement chamber 37

3.3.2. The positive ion ToF mass spectrometer 40

3.3.3. The extraction field geometry and operating parameters 42

3.3.4. pToF performance and mass resolution . . . 44
3.4. Upgraded setup: Simultaneous dual polarity ToF mass spectrometer with electron start . . . 46
3.4.1. The negative ion ToF mass spectrometer and changes to the positive ion ToF mass spectrometer . . . 48
3.4.2. Simulation of extraction field and secondary electron separation . . . 50
3.4.3. Experimental extraction field, electron separation and operating parameters . . . 55
3.4.4. pToF and nToF performance and mass resolution . . . 57

4. Molecular imaging 61
4.1. Large scale imaging of a GaAs wafer . . . 61
4.2. Line scan lateral resolution measurements . . . 64
4.3. Sputter damage visualization on a homogenous sample . . . 66

5. Secondary ion yield and fragmentation 69
5.1. Samples and yield measurements within the framework of the IAEA CRP . . . 70
5.2. Methodology and primary ion species . . . 77
5.2.1. Exploring stopping power regimes using a range of atomic and cluster primary ion beams . . . 77
5.2.2. Performing the measurements . . . 79
5.2.3. Data analysis: Mass spectra calibration and yield determination . . . 81
5.3. Total secondary ion yield . . . 82
5.3.1. Scaling with primary ion velocity . . . 83
5.3.2. Scaling with electronic stopping power . . . 88
5.4. Peak yields and fragmentation . . . 91
5.4.1. Scaling of individual peak yields with electronic stopping power . . . 93
5.4.2. Fragmentation behaviour with electronic and nuclear stopping . . . 99

5.5. Cluster ions 109
5.5.1. Secondary ion yield scaling with electronic stopping per cluster constituent: cluster effects in MeV-SIMS 109
5.5.2. Fragmentation induced by primary cluster ions 113

6. Dual polarity secondary ion mass spectrometry 119
6.1. Accessing all the ions from two different samples 119
6.2. Event correlation analysis: simultaneous emission of multiple ions 121
6.3. Positive and negative secondary ion yields 127

7. Summary and conclusion 131

8. Outlook 135

Appendix 137

A. Technical improvements and modifications to the CHIMP setup 137

B. Production and characterization of glass capillaries 139

C. Compilation of experimental yield and fragmentation data 142
C.1. GID interpolation and error estimate 142
C.2. Mass spectra calibration and peak fitting 143
C.3. Additional peak yields and fragmentation data 146

Bibliography 155

Contributions 169

Abstract

Secondary ion mass spectrometry (SIMS) is one of the leading imaging mass spectrometry techniques used to analyse local sample composition with applications ranging from semiconductor technology via metallurgy, geology and art analysis to the forensic sciences, pharmaceutical development as well as life science, biology and medicine. However the growing interest in the ability to analyse the distribution of increasingly larger molecular species provides a challenge for conventional keV-SIMS.

In recent years, the potential of using swift heavy ion beams with energies in the MeV range has been explored after initial studies observed a significant enhancement in the emission of large molecular secondary ions. Consequently the new analytical technique of MeV-SIMS was developed with ion beam analysis laboratories all over the world setting up dedicated instruments. The main focus of this research is to establish the analytical technique and apply it to a wide range of research questions. Therefore, the potential of capillary collimated MeV-SIMS for molecular imaging is explored and demonstrated in the first part of this thesis. Nevertheless, a lot is still to be gained from a better in-depth knowledge of the underlying processes of secondary ion desorption and ionization, which are until now not well understood.

The current work provides the basis for this improved understanding by exploring secondary ion yields over an unprecedented wide range of primary ion beam parameters. In addition to energetic monoatomic primary ions, differently sized cluster projectiles consisting of light and heavier constituents are employed. The results confirm a complex dependence of the secondary ion emission processes on the stopping power characteristics of the primary ion. Increased electronic and decreased nuclear stopping power enhance the observed yields significantly before a levelling off due to a saturation effect. This yield increase is not equal for fragment and full-mass molecular secondary ions, resulting in a significant reduction of fragmentation observed in the secondary ion mass spectra. The use of cluster ions ad-

ditionally reduces fragmentation of secondary ions strongly and by studying secondary ion yields as a function of primary cluster size, non-linear cluster effects are observed for the first time in MeV-SIMS. These cluster effects likely originate from the collective impact of the constituents and also show a saturation with increasing cluster size. The observations are compatible with a phenomenological model of secondary ion emission: In this model, molecular ions are emitted primarily from an outer *ultratrack* region by sputtering induced through energy deposition via electronic stopping power (electronic sputtering) and mediated by secondary δ-electrons. In contrast, increased fragmentation and nuclear stopping cause the emission of smaller ions from an inner *infratrack* region.

To extend these studies performed with positive secondary ions, the Capillary Heavy Ion MeV-SIMS Probe (CHIMP) was developed into a novel dual polarity mass spectrometer instrument with an electron start capability by simultaneous detection of secondary electrons, negative and positive ions. A first study reveals highly interesting effects: The ratio of corresponding positive and negative ion yields, which is heavily biased for monoatomic primary ions, approaches parity when employing primary cluster ions of increasing size. Additionally the emission of multiple secondary ions from a single projectile impact is also promoted by the use of larger primary cluster ions. The upgraded CHIMP setup at the TANDEM accelerator facility therefore provides a unique platform for future in-depth studies to shed more light on the processes of secondary ion emission.

Zusammenfassung

Sekundärionenmassenspektrometrie (SIMS) ist eine der führenden Techniken der bildgebenden Massenspektrometrie, die zur ortsaufgelösten Analyse der Zusammensetzung einer Probe verwendet wird. Ihre Anwendungen reichen von der Halbleitertechnologie über Metallurgie, Geologie und der Analyse von Kunstwerken bis zur Forensik, pharmazeutischen Entwicklung und den Lebenswissenschaften, der Biologie und Medizin. Allerdings stellt das wachsende Interesse an der Analyse von Molekülen zunehmender Grösse eine Herausforderung für konventionelle keV-SIMS dar.

In den letzten Jahren wurde die Verwendung schneller, schwerer Ionenstrahlen mit MeV-Energien untersucht, nachdem erste Studien eine deutliche Steigerung der Emission von grossen, molekularen Sekundärionen beobachtet hatten. Daraufhin wurde die neue Analysemethode der MeV-SIMS entwickelt und weltweit richten Ionenstrahlanalytiklabore entsprechende Instrumente ein. Das Hauptaugenmerk der Forschung liegt auf der Etablierung der Methode und ihrer Anwendung auf ein breites Spektrum von Forschungsfragen. Daher untersucht der erste Teil dieser Arbeit MeV-SIMS in Verbindung mit Ionenstrahlkollimation mittels einer Glaskapillare und zeigt das Potential dieser Technik zur molekularen Bildgebung auf. Allerdings kann durch eine detaillierte Kenntnis der zugrundeliegenden Desorptions- und Ionisationsprozesse für Sekundärionen, die bisher nicht gut verstanden sind, immer noch sehr viel gewonnen werden.

Die vorliegende Arbeit liefert die Grundlage für dieses bessere Verständnis, indem die Sekundärionenausbeute über einen bisher unerreicht grossen Bereich von Primärionenparametern untersucht wird. Zusätzlich zu energetischen monoatomaren Primärionen werden auch Clusterprojektile aus leichten und schwereren Konstituenten verwendet. Die Resultate bestätigen eine komplexe Abhängigkeit der Sekundärionenemissionsprozesse von der Bremscharakteristik des Primärions. Erhöhte elektronische und verminderte nukleare Brem-

swirkung erhöhen die beobachtete Ausbeute signifikant, bevor sie aufgrund eines Sättigungseffektes abflacht. Dieser Ausbeuteanstieg ist nicht gleich stark für Fragmente und molekulare Sekundärionen voller Masse, sodass eine deutliche Reduktion der Fragmentation in den Sekundärionenspektren beobachtet wird. Die zusätzliche Verwendung von Clusterionen vermindert die Fragmentation der Sekundärionen deutlich. Durch die Untersuchung der Sekundärionenausbeute als Funktion der Primärclustergrösse werden erstmals nicht-lineare Clustereffekte in MeV-SIMS beobachtet. Diese Clustereffekte entstehen vermutlich aufgrund des kollektiven Einschlags der Konstituenten und weisen ebenfalls eine Sättigung mit zunehmender Clustergrösse auf. Die Beobachtungen sind kompatibel mit einem phenomenologischen Modell der Sekundärionenemission: In diesem Modell werden molekulare Ionen primär durch Sputtern aus einer äusseren *ultratrack* Region und aufgrund der Energiedeposition durch elektronische Bremswirkung (elektronisches Sputtern) - vermittelt durch sekundäre δ-Elektronen - emittiert. Währenddessen verursachen erhöhte Fragmentation und nukleare Bremswirkung in einer inneren *infratrack* Region die Emission von kleineren Ionen.

Um diese Studien an positiven Sekundärionen zu ergänzen, wurde die Capillary Heavy Ion MeV-SIMS Probe (CHIMIP) zu einem neuartigen zweipoligen Massenspektrometer mit Elektronenstart durch simultane Detektion sekundärer Elektronen sowie negativer und positiver Ionen weiterentwickelt. Eine erste Untersuchung offenbart sehr interessante Effekte: Das Verhältnis von korrespondierenden positiven und negativen Ionenausbeuten, das für monoatomare Primärionen sehr unausgewogen ist, nähert sich der Parität an, wenn Primärclusterionen zunehmender Grösse verwendet werden. Auch wird die Emission von mehreren Sekundärionen von einem einzigen Projektileinschlag durch den Einsatz grösserer Primärclusterionen begünstigt. Das erweiterte CHIMP Instrument an der TANDEM Beschleunigeranlage stellt daher eine einzigartige Plattform dar, um mit zukünftigen detaillierten Studien Aufschluss über die Prozesse der Sekundärionenemission zu geben.

Thank you

This work would not have been possible without a wide range of help and support from many people around me. I would like to thank all of them at this point:

Prof. Dr. Hans-Arno Synal, who offered me the PhD position at the Laboratory of Ion Beam Physics after successful completion of my master thesis. The straightforward and motivating atmosphere and good working environment you create in the group is remarkable. I particularly valued the large degree of freedom while at the same time your door is always open for discussions.

Dr. Max Döbeli, who leads the Materials Science research at the Laboratory of Ion Beam Physics and was therefore my first contact to discuss my research. Thank you for all your advice and support, your clever ideas and ability to put observations into context. The discussions with you were always insightful - whether in the office or while resolving issues with or trying to optimize experimental parameters at the instrument.

Prof. Dr. Rainer Wallny and Prof. Dr. Primož Pelicon for readily agreeing to be co-examiners of this thesis and their interest in my work. Additional thanks go to Prof. Dr. Manfred Sigrist for offering to chair my doctoral examination.

Dr. Christof Vockenhuber, who initially introduced me into the world of Ion Beam Physics by supervising both my semester and later my master thesis. Your enthusiasm for experimental work was contagious - and even during my PhD I could always count on your support and differentiated point of view.

Nicolas Brehm for the long measurement days in the control room and accelerator hall and his efforts to automated the analysis of our measured mass spectra. The measurement data we collected together and your master thesis were very valuable contributions to this work.

Dr. Martina Schulte-Borchers and Dr. Marius Simon for their introduction to the MeV-SIMS setup as well as the production of capillaries for beam collimation. Both of your theses were highly useful - initially as an introduction and later on as a reference.

Dr. Boštjan Jenčič, who joined the Laboratory of Ion Beam Physics for a postdoc after finishing his PhD on MeV-SIMS at Jožef Stefan Institute in Ljubljana. Discussing the setup and technical challenges with you was very helpful and you were able to provide a different point of view on things.

Prof. Dr. Jiro Matsuo and his group at Kyoto University for providing samples - complete with reference spectra - for my measurements.

Jürg Thut for his good ideas and steady iterations on the design of the dual-polarity mass spectrometer. Your experience was extremely valuable in integrating the new setup into the existing instrument.

Rene Gruber, Philippe Vogel and Andras Wagner for their support and help in all technical things - especially the installation of the new mass spectrometer and the maintenance of the ion source and Tandem accelerator. Without you, my experiments would have been hardly possible. Thanks also to Simon Bühlmann and Rudolf Pfenninger for their electronics and software support.

Everyone who helped reading over this thesis: Thanks Max, Arno and Christof for your valuable suggestions and corrections as well as Anne-Marie, Daniele, Ewelina, Laura and Olivia for your careful proof reading.

The Swiss National Science Foundation (SNSF) for providing the funding for this PhD project (SNF project funding 175653 'New Developments in Ion Beam Physics').

A huge Thank You goes to the whole LIP team - you all made the last four years not only successful and productive, but also very enjoyable and memorable! Working in such a good atmosphere was a pleasure and the coffees - often with cake - and after-work beers provided welcome breaks. With many of you I also shared sports activities - from running, cycling, sailing, mountaineering and playing soccer in summer to skiing in winter and circuit training all year round! Thank you Reto, Daniele, Laura, Anne-Marie, Maxi, Ewelina, Sarah,

Chrissi, Matthias, Christof, Lukas, Marcus and Núria for the extensive and very complete sports program! Thank you Philipp, Nici, Melina, Noldi, Caro, Anita, Andras and Philippe for the many table soccer games. Thank you Olivia, Kristina and Susan for bringing not only rocks but also nice pictures from your excursions and thank you Lindita, Silvia, Maria, Mantana, Negar and Irka for the good atmosphere in the coffee breaks.

Thanks go also to my friends and colleagues inside and outside ETH and at AMP: You were always interested in my work and open to discussions during lunch breaks or visits of the laboratory. Trying to explain things to you often helped to maintain a broader view and put things into context.

Finally, my parents and my sister were always there for me throughout my entire studies at ETH Zurich: It means a lot to me that I can always count on your help, support and motivation in all matters. You encouraged me at all times and motivated me to strive higher in everything I do.

1. Introduction

Since the idea of imaging mass spectrometry had been introduced over 60 years ago by Castaing and Slodzian (1962), the field has experienced a tremendous development. Especially since the late 1990s there has been a strong effort to develop mass spectrometry techniques suited for imaging of biological samples: Imaging mass spectrometry which is able to map concentrations of not only atoms but also large molecules with a lateral resolution at the cell level holds significant promise for biomedical research. However, to be able to reach a high lateral resolution in the µm-range and at the same time detect heavy molecular species from the sample, an extremely efficient desorption and ionisation process is needed. Consequently, a wide range of analytical techniques have been developed and used to approach this goal.

1.1. A comparison of imaging techniques for molecular sample characterization

The most commonly used and advanced techniques for molecular concentration mapping are currently Desorption Electrospray Ionization (DESI, (Takáts et al. 2004)), Matrix Assisted Laser Desorption and Ionization (MALDI, (Laiko et al. 2002)) and several enhanced types of Secondary Ion Mass Spectrometry (SIMS). In the following these are briefly introduced and their advantages and shortcomings compared.

Desorption Electrospray Ionization (DESI)

DESI is the most recently developed imaging mass spectrometry technique of the three (Takáts et al. 2004) and combines the techniques of electrospray and desorption ionization: Energetic, charged electrosprayed solvent droplets are targeted at the sample and induce the release of molecules from the surface. The technique can be applied matrix-free under

atmospheric pressure and thus enables in-situ and real-time analysis. According to Cobice et al. (2015), a spatial resolution of several 100 µm is achieved in routine analysis, while nano-DESI promises to an increased resolution on the order of 10 µm (Laskin et al. 2012). Quantitative reproducibility on the order of 20 % can be achieved although differences in experimental design frequently introduce a significant variability (Gurdak et al. 2014). The technique is largely independent from differences in ionization yields, however it can not be used for molecules that are strongly bound to the sample substrate and very small volatile molecules (Cobice et al. 2015).

Matrix Assisted Laser Desorption and Ionization (MALDI)

Introduced by Karas and Hillenkamp (1988), MALDI is probably the most widely used molecular imaging technique today due to its unique ability to detect very large molecules over a mass range up to 25 kDa (non-imaging MALDI can routinely detect even larger molecules). The technique requires considerable sample preparation since the sample needs to be coated either with a homogeneous layer or droplets of a matrix material before it is then scanned with a focussed pulsed laser beam. The matrix material absorbs the laser energy, leading to the ablation of both the applied matrix and the sample material below. Due to the additionally applied matrix material and its influence on the desorption and ionization yield, quantification is rather difficult requiring calibration with internal standards, which is possible to some extent. The technique can be applied under ambient pressure (Laiko et al. 2002), although most setups require a transfer of the sample into vacuum. Typically laser spot sizes on the order of 20 µm to 100 µm are used. Under special conditions a focus down to around 7 µm was reported by Holle et al. (2006), however such small focus sizes significantly limit the sensitivity of the technique and spatial resolution is also influenced by the applied matrix layer.

Secondary Ion Mass Spectrometry (SIMS)

As the first imaging mass spectrometry technique, SIMS was initially mostly used as an analysis tool in the semiconductor industry - but rather fast it was also applied to study biologically relevant sample materials (Benninghoven and Sichtermann 1978). In its conventional form a low energy (keV) primary ion beam is focussed on and scanned across the sample. The impact of the primary ions and their energy deposition in the sample material induces desorption of secondary ions from the sample surface. SIMS can reach a very high spatial resolution down to about 50 nm and as a matrix-free technique does not require any sample preparation. Like in MALDI, matrix effects can strongly influence the sputter yields and ionization probabilities. But the characteristics of the keV-SIMS desorption process lead to significant fragmentation, such that the mass range of detectable secondary ions is typically limited to <1 kDa. This is the reason why in recent years several modified SIMS techniques were developed with the goal to enhance secondary ion yields of larger molecular ions: Notable are here cluster-SIMS (Cheng and Winograd 2006) as well as metal-assisted (Delcorte and Bertrand 2004) and matrix-enhanced SIMS (Delcorte 2006). These techniques managed to significantly increase the mass range of detectable molecules (Heeren et al. 2006), however both metal-assisted and matrix-enhanced SIMS again introduce the need for sample preparation and all of the modified SIMS techniques are not suitable for analysis under ambient pressure conditions.

1.2. The emergence of MeV-SIMS

The first use of MeV primary ions for SIMS dates back almost 50 years (Torgerson, Skowronski, and Macfarlane 1974), when Torgerson et al. used ^{252}Cf fission fragments to desorb positive and negative ions from the aminoacids arginine and cystine and observed intense quasi-molecular signatures in the measured Time-of-Flight (ToF) mass spectra. Only two years later, they published their findings in more detail (Macfarlane and Torgerson 1976) and coined the term Plasma Desorption Mass Spectrometry (PDMS) for their new technique. The observed very high yields of molecular secondary ions were unexpected and could not be

explained by the existing sputter theories, specifically the collision cascade model (Sigmund 1969) used to estimate yields in nuclear sputtering. It therefore became clear, that the desorption mechanism present in PDMS had to be drastically different: In keV-SIMS secondary atoms and ions are ejected due to direct nuclear collisions between primary ions and the atoms of the solid and their corresponding momentum transfer. This regime, in which the collision cascade model is able to reliably predict secondary ion yields is however only valid for velocities of the primary ions below the Bohr velocity of the electrons in the sample material: $v_{PI} < v_{Bohr}$. For significantly faster primary ions ($v_{PI} >> v_{Bohr}$), the energy is primarily deposited via electronic energy loss into the electronic subsystem of the sample material within the few monolayers of the sample. The resulting desorption phenomena therefore are rather complex and depend on the actual energy density, the deposition rate and the energy relaxation times of the electronic subsystem. Therefore a range of experimental studies on the newly discovered 'electronic sputtering' phenomenon were conducted by studying the influence of different physical parameters of monomer and cluster primary ion beams on the sputtering process. Besides primary ion velocity and primary ion energy, also the influence of energy loss, the charge state, the effective charge and the incidence angle on secondary desorption yields and damage cross sections were studied. Based on the experimental results there was also some effort to follow up with theoretical models to explain these phenomena or predict the experimental observations. Comprehensive reviews of both experimental data and theoretical frameworks were given by Wien (1989) and Daya et al. (1997). However the complexity of the interaction still occludes the understanding and especially the influence of primary cluster ions is poorly understood.

Nevertheless the earlier findings were revisited in recent years when researchers from Kyoto university working on cluster-SIMS realized the potential of MeV primary ions for molecular SIMS (Nakata et al. 2008). They appropriately named the new technique MeV-SIMS and within a few years research at a range of different laboratories all over the world was established. The expressed goal is to apply the unprecedented high molecular desorption yields and the already widely proven imaging capabilities of ion beam analysis techniques to

develop MeV-SIMS into a new and powerful analytical technique (Jones 2012). Since then it could be shown that MeV-SIMS provides a unique combination of performance characteristics when compared to most other techniques currently used for imaging mass spectrometry: The technique inherits the extreme surface sensitivity and high spatial resolution of SIMS, while fragmentation is considerably lower than in conventional keV-SIMS with the damage inflicted onto the sample being very limited and far lower than for MALDI. Additionally, the energetic primary ion beam can be extracted into air, allowing ambient pressure in-situ analysis as it is possible with DESI and MALDI. Moreover, MeV-SIMS can also be simultaneously combined with other IBA techniques like Particle Induced X-ray Emission (PIXE) and Rutherford Backscattering Spectrometry (RBS) into a single measurement, providing additional quantitative information about the sample composition.

1.3. Studying secondary ion desorption: a motivation

The recent activity in the field has yielded some impressive results achieved by the application of MeV-SIMS for studies in the life sciences, forensics (Bailey et al. 2010), in research on liquid interfaces (Seki et al. 2016), biological samples (Jenčič, Jeromel, et al. 2016) including single cells (Siketić et al. 2015) and modern paint analysis (Bogdanović Radović et al. 2017). However the underlying processes of desorption and ionization are still not well explained and a convincing argument can be made that a better knowledge of these processes could extend and enhance the performance of the technique as an analytical tool significantly.

The goal of this thesis is therefore to systematically explore the emission of secondary ions under bombardment with heavy primary ions with MeV energies. The acquired data lays a foundation for a better understanding of the desorption process in MeV-SIMS and therefore a possible improvement of the quantitativeness of the technique for a large variety of sample materials. Of specific interest is how secondary ion yields depend on the electronic and nuclear stopping power of the specific projectile ions used.

While cluster ions can be used to extend the possible stopping power regimes of the primary

ion projectile, it is also of high interest whether and how the relative secondary ion yields are influenced by the use of primary cluster ions with MeV energies: In keV-SIMS significant non-linear cluster effects were observed in the measured secondary ion yield due to collective effects of the cluster constituents (Guillermier et al. 2006).

Additionally it should be highly instructive to study the statistics of the correlated emission of several secondary ions and electrons from a single primary ion impact. Especially interesting should be to compare positive and negative ion spectra and individual correlations between the ones desorbed by a specific impact, since this offers the possibility to better understand and partly decouple the effects of desorption and ionization. Finally the compression of the distribution of deposited energy close to the sample surface achieved by the use of primary MeV cluster ions and the resulting highly exited material state from which secondary ions are desorbed holds the possibility of strongly reduced matrix effects in MeV-SIMS, which usually limit the quantitativeness of conventional SIMS.

1.4. Outline and structure of the present work

The secondary ion yield data collected during the past four years with the MeV-SIMS setup CHIMP at ETH Zurich are primary achievements of this thesis. Therefore the measurement setup and the upgrades to it that were implemented during that time period as well as some of the relevant technical details are described. The main focus is however to demonstrate and illustrate the most significant and important features of secondary ion emission in MeV-SIMS identified from the sizeable collection of measurements that have been acquired.

In **Chapter 1** a brief introduction into the most important techniques available for mass spectrometry imaging is given. After a brief comparison of the three established techniques DESI, MALDI and conventional keV-SIMS, the emerging technique of MeV-SIMS is introduced. Finally a motivation to study and understand the underlying secondary ion desorption and ionization processes is given by outlining the potential for MeV-SIMS as an quantitative analytical technique.

The basics of secondary ion emission in SIMS are summarized in **Chapter 2**, where initially the possible processes of energy deposition by the primary projectile in the target are described. The parameters characterising secondary ion emission are discussed and the most important experimental results from the last 50 years in the field are briefly reviewed, before a phenomenological overview of the most relevant theoretical frameworks is provided.

The Capillary Heavy Ion MeV-SIMS Probe (CHIMP) developed at ETH Zurich is presented in **Chapter 3**. This setup is specifically suited for yield studies and was significantly upgraded from a single polarity (positive) secondary ion Time-of-Flight spectrometer with infinite-stop electron start to a dual polarity system capable to detect secondary electrons, negative and positive secondary ions. Both the initial and upgraded setups are described including a brief overview of the TANDEM accelerator facility at which both setups are installed and a description of the glass capillary setup used to collimate the heavy and energetic primary ion beams.

To showcase the capabilities of MeV-SIMS in molecular imaging as well as the potential of primary beam collimation down to a beamsize on the order of a few µm, **Chapter 4** showcases three different molecular imaging studies performed at the CHIMP setup.

Secondary ion yield measurements performed with the initial single polarity CHIMP setup are discussed in **Chapter 5**. The sample materials analysed are introduced and their mass spectra are characterized before the overall methodology and the primary ion species used are detailed. The acquired data is then presented in different frameworks and dependencies. Initially the focus is on the scaling of total secondary ion yields, but later the mass spectra are broken down to look at yields and relative intensities of individual mass peaks. This enables the study of fragmentation in the desorption process. Lastly, the secondary ion yield data acquired with primary cluster ion beams is specifically analysed to identify possible cluster effects and the impact of cluster size on secondary ion fragmentation characteristics.

First dual polarity MeV-SIMS measurements completed with the new upgraded CHIMP setup are then presented in **Chapter 6**. After reproducing the spectra of the used samples the data is analysed with a focus on two specific issues: Event correlation analysis is used to

study the effect of primary cluster size on the simultaneous emission of multiple ions from a single projectile impact and a comparison of simultaneously measured positive and negative secondary ion yields is performed.

To conclude, **Chapter 7** summarizes the main characteristics identified in the secondary ion yield data and traces them back to the initially discussed secondary ion emission processes.

Last but not least an outlook is given in **Chapter 8** on the future potential of the upgraded dual-polarity setup CHIMP and possible studies that are enabled by its unique design. The possible knowledge gain on secondary ion emission processes and its impact regarding the power of MeV-SIMS as an analytical technique are outlined.

2. Secondary ion emission in SIMS

Secondary ion emission in SIMS is a rather complex process and not completely understood yet. Therefore this chapter gives an overview of the most important experimental studies and theoretical models. Readers that already have a good understanding of the topic or those that want to focus on the core results of the present thesis can initially skip this chapter, although they might want to revisit parts of it at a later for a better context. To begin, Section 2.1 will give an introduction into the processes by which energy is deposited into the sample material by an impacting primary ion. Based on this deposition of energy, then Section 2.2 will first discuss secondary ion desorption from the sample in general, before focusing specifically on electronic sputtering by reviewing experimental results from the last 50 years. Finally, in Section 2.3 the theoretical models developed to reproduce and predict the observed behaviour will be discussed.

2.1. Energy loss processes in matter

As soon as the primary ion reaches the sample surface and begins to move through matter, it interacts with the surrounding material. Through these interactions the primary ion loses energy and slows down. Based on how the energy is transferred into the sample material, three distinct energy loss processes for fast particles are distinguished:

- Nuclear energy loss due to interactions between the ion and the screened or unscreened nuclei of the sample atoms.
- Electronic energy loss due to interactions between the ion and bound or unbound sample electrons.
- Radiative energy loss (Bremsstrahlung) due to rapid deceleration of the ion within the sample material.

The contributions of all three energy loss processes are usually characterized by the specific energy loss rate or stopping power $\frac{dE}{dx}$ of an ion in the specific sample material. The total energy loss of a particle in matter can thus be given by:

$$\frac{dE}{dx} = \left(\frac{dE}{dx}\right)_{nuc} + \left(\frac{dE}{dx}\right)_{el} + \left(\frac{dE}{dx}\right)_{rad} \tag{2.1}$$

Based on the predominant contribution to the total stopping power of a particle in matter, three stopping power regimes can be distinguished, since the strength of all three energy loss processes for a given combination of primary ion species and sample is primarily dependent on the ion velocity relative to the sample material:

For velocities slower than the Bohr velocity (approximating the velocity of the atomic electrons) $v_0 = 2.188 \cdot 10^8\,\mathrm{cm\,s^{-1}}$, nuclear stopping dominates (Keinonen 2005). At these low velocities, ions predominantly interact with the target nuclei via elastic collisions, usually resulting in a strong deflection of the primary ion path, a relatively high energy loss per individual collision and the displacement of atoms in the sample material. With increasing energy of the primary ion the amount of nuclear stopping decreases rapidly.

In the case of faster ions with velocities significantly higher than the Bohr velocity, electronic stopping is the main effect. Here the energy is directly deposited in the electronic subsystem by inelastic collisions of the ion with bound electrons, leading to excitation and even ionization. Due to its significantly higher mass compared to the electron the primary ion is only deflected slightly from its initial trajectory, loses a much smaller amount of energy per collision and the displacement of an atom within the sample material is rather unlikely.

Finally, radiative energy loss however becomes only relevant for light particles at very high (relativistic) velocities and can therefore be neglected for all further discussions concerning SIMS with monomer or cluster primary ions with energies below 100 MeV as used in this thesis.

Therefore only the nuclear and electronic stopping regime are distinguished, which are relevant for keV- respectively MeV-SIMS: For illustration in figure 2.1 the nuclear and electronic

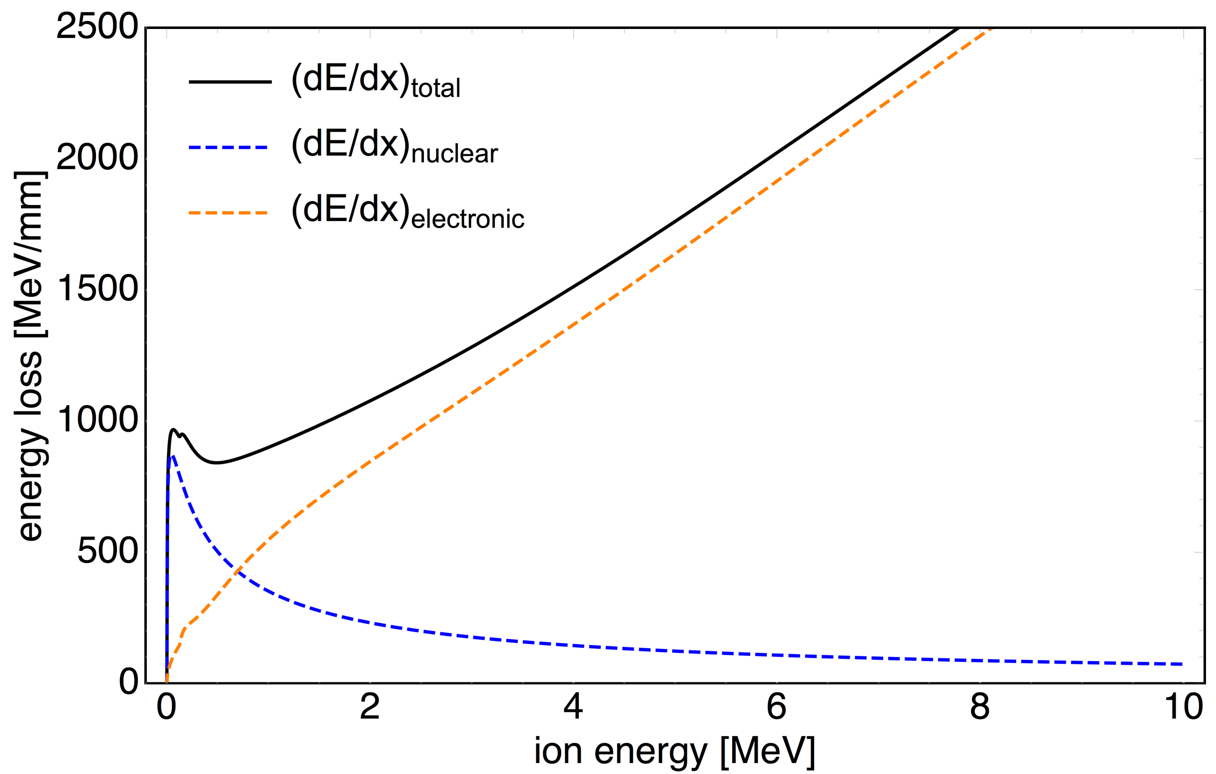

Figure 2.1.: Nuclear, electronic and total stopping power of ^{63}Cu monoatomic primary ion in arginine.

stopping power - as well as their sum - as calculated by SRIM (Ziegler, Biersack, and Littmark 1985) are plotted for monoatomic ^{63}Cu primary ions with an energy of up to 10 MeV in arginine. Nuclear stopping dominates at very low energies, before it reaches its maximum at a primary ion energy of a few ten keV and decreases with approximately $\frac{1}{E}$ at higher energies. Meanwhile the electronic energy loss increases fast and becomes the major contribution to the total energy loss at a primary ion energy of a few hundred keV. It continues to increase continuously from there on - electronic stopping is roughly proportional to the ion velocity for $0.1 \cdot v_0 \leq v \leq Z_{PI}^{3/2} \cdot v_0$ (Nastasi et al. 2014) - and therefore outweighs the nuclear energy loss by orders of magnitude for primary ion energies of several MeV. For faster ions with $v > Z_{PI}^{3/2} \cdot v_0$, the electronic stopping power decreases again proportional to $\left(\frac{Z_{PI}}{v}\right)^2$ (Nastasi et al. 2014).

Apart from its dependence on velocity of the primary ion, the stopping also strongly depends on the atomic numbers of the incident ion Z_{PI} and the sample atoms Z_S: While for higher-Z ions nuclear energy loss is more dominant at low energies of up to a few MeV, for lower-Z ions the electronic energy loss in this energy regions is already higher and therefore gets relevant at even lower primary ion energies.

2.2. Secondary ion desorption mechanisms

There are two separate fundamental parameters that determine the secondary ion current I_m of an ion species m: The actual sputter yield Y_m and the ionization probability $\alpha^{\pm}$ which determines how many of the desorbed secondary particles also get ionized into positive or negative charge state, respectively. Overall the experimentally measured secondary ion current is defined using the following SIMS-equation, where I_{PI} denotes the primary ion particle current, θ_m the fractional concentration of the species m in the analysed material and ϵ the detection efficiency of the used analysis system:

$$I_m^{\pm} = I_{PI} \cdot Y_m \cdot \alpha^{\pm} \cdot \theta_m \cdot \epsilon \qquad (2.2)$$

According to the distinction between nuclear and electronic stopping regime, one can also differentiate at least two vastly distinct mechanisms of secondary ion desorption. These were indentified early on by a nuclear respectively electronic branch of the measured secondary ion yields (Albers et al. 1982).

In conventional SIMS (or keV-SIMS) primary beam energies are usually in the range of several ten keV with commonly used primary ion species such as O, Ar, Ga, Cs, monoatomic Bi or Au_n, Bi_n and C_{60} cluster ions. With these experimental parameters the energy loss in the sample material is primarily nuclear energy loss. Repeated nuclear interactions result in collision cascades within the sample material. Some of these cascades return to the sample surface and particles can be ejected if the energy they receive in an outward directed collision is higher than the surface binding energy of the sample material. Some of these particles can also be ionized upon leaving the sample material, resulting in negative or positive secondary ions that can be extracted by the application of an electric field for analysis.

The primary ion energy threshold for this *nuclear* or *collisional sputtering* is on the order of 20 eV to 40 eV, with a maximal secondary ion yield at around 5 keV to 50 keV. Vickerman (2009) notes that in this regime secondary particles are emitted within approx. 10 nm from the primary particle impact and final collision energies are on the order of 20 eV, such that $>95\,\%$ of the emitted secondary particles originate from the top two monolayers of the sample. In the early days of SIMS, this surface sensitivity remained mostly unused. Most analyses were done destructively with a high primary particle fluence to analyse the elemental composition of the sample material as a function of depth by sputtering away and thereby removing the sample material.

This regime is therefore called *dynamic SIMS* - in contrast to the *static SIMS* regime developed in the 1970s (Benninghoven 1971) in which very low primary particle fluences ($<1 \cdot 10^{12}\,\mathrm{p\,cm^{-2}}$) are used to acquire a mass spectrum before the surface of the sample is noticeably affected by sputter damage. Finally, the use of cluster ions leads to significantly increased secondary ion yields especially from molecular materials and therefore increases the sensitivity of the technique.

Additionally, the damage inflicted to the sample material by larger clusters seems to be much reduced, such that the term of *molecular SIMS* was introduced (Benninghoven 1971).

Conversely, the predominant sputtering mechanism in Plasma Desorption Mass Spectrometry (PDMS) and MeV-SIMS with much higher primary beam energies in the MeV range is *electronic sputtering*. The energy is primarily deposited by electronic energy loss into the electronic subsystem of the sample material by excitation of bound electrons, ionization, energy transfer to free electrons and thus general heating. In order to remove an atom or molecule from the sample surface, bonds have to be broken and energy has to be transferred or converted from the electronic system to kinetic energy of the sputtered particle. This can be mediated in a number of different ways, making the desorption and sputtering effect dependent on the energy deposition rate and its relation to the timescales of energy relaxation of the electronic subsystem. This makes the desorption and ionization process rather complex - a few theoretical models will be discussed in more detail in chapter 2.3.

A subcategory of electronic sputtering is *potential sputtering*, in which the potential energy of multiple charged projectiles is transferred to the electronic subsystem of the sample material specifically by recombination during the impact, leading to a strong dependence of the secondary ion yield on the primary ion charge state. Due to the liberation of potential energy of the projectiles, potential sputtering can already occur at kinetic primary ion energies well below the usual sputtering threshold of the material.

Finally, in addition to these two mechanisms of so-called physical sputtering, *chemical sputtering* employs specific primary ion species to break or soften bonds at the surface of the sample material. This can lead to the formation of weakly bound or volatile molecules that are then desorbed without the need of an additional kinetic energy transfer. The technique is therefore often employed in static SIMS to enhance the non-destructive desorption of molecular secondary ions.

Experimental results have shown early on that electronic sputtering especially for desorption and ionization of heavy molecular species is extremely efficient and yields several orders of

magnitude higher than those from nuclear sputtering are achievable (P. Haff and L. Seiberling 1981). Thus, in the 1980s a range of experimental studies were carried out to explore and better understand the increased sputter yields as well as to characterize their behaviour with regards to angular emission and velocity distribution. One of the first studies was published by Håkansson, Johansson, et al. (1981) and found that molecular ion yields increase rapidly by over two orders of magnitude with primary ion velocity in the range of $0.2\,\mathrm{cm\,ns^{-1}}$ to $0.3\,\mathrm{cm\,ns^{-1}}$. The yield as a funciton of incidence angle were also found to follow a $cos(\vartheta)^{-n}$ dependence with $n > 2$. In another paper Håkansson, Jayasinghe, et al. (1981) studied the dependence of secondary ion yields on the charge state of the incident primary ion and found yields increasing with higher charge states, while the fragmentation patterns observed in the mass spectra stayed unchanged. Dück et al. (1982) found yields to be roughly proportional to the charge state of the primary ion and Voit et al. (1983) concluded that the desorbed secondary molecular ions have to originate from the sample surface or a thin layer below which seems to be thinner than the depth needed for the primary ion to reach its equilibrium charge state in the sample material. A few years later Salehpour et al. (1986) measured the total yield of desorbed particles and found that most of them are neutrals, with ions only making up about 1 ‰ of the ejected material. Following up on the earlier studies, Säve et al. (1987) used a range of different primary ions at the same velocity to vary the energy density deposited in the ion track. They found yields increasing with the layer thickness of the sample material on a substrate with a saturation layer thickness of 8 nm to 20 nm, while the general shape of the yield curves with layer thickness is independent of the specific stopping power of the primary ion used (and therefore the energy density in the track). For thin films insulating substrates provided higher secondary ion yields than conducting ones. Especially notable is that Hedin, Håkansson, Salehpour, et al. (1987) used a collector based method to measure a scaling of the desorbed neutral yield with rouhgly $\left(\frac{dE}{dx}\right)^3$, while the positive and negative ion yields varied approximately with $\frac{dE}{dx}$ and $\left(\frac{dE}{dx}\right)^2$, respectively.

However Becker et al. (1986) observed in a study utilizing very heavy primary ion beams that this scaling does not continue beyond the velocity corresponding to maximum total yield.

Therefore yields for primary ions positioned on opposite sides of the Bragg peak but with the same specific stopping power are not identical, which allowed the conclusion that there is no simple relationship between energy loss and secondary ion yields. The authors address this by noting that ion production is only a small effect since most of the material is ejected in neutral state and potentially masking the nature of the underlying desorption process.

After these initial studies it took almost two decades before these remarkable characteristics of electronic sputtering sparked widespread new interest again: Around the turn of the 21st century cluster ions became more and more widely used in conventional (keV-)SIMS instruments due to the increase in secondary ion yields for molecular materials. Their use consequently significantly increased the sensitivity of the technique and its potential for applications in the biological sciences. Large cluster ions not only increased the secondary ion yield but also seemed to inflict less damage to the sample material (Ninomiya et al. 2007). Not much later Nakata et al. (2008) performed comparison measurements of arginine samples using 10 keV Ar^+ and 2 MeV $Cu_2{}^+$ citing the older PDMS work (Torgerson, Skowronski, and Macfarlane 1974) and found that not only molecular ion desorption is increased, but that also fragmentation seemed to decrease with increasing incident energy. Recognizing the potential of this behaviour Nakata et al. (2009) developed the molecular imaging mass spectrometry technique which they named MeV-SIMS and reported increases in molecular positive and negative ion yields of $>10^3$ compared with keV-SIMS and even substantially higher than in cluster-SIMS. These studies immediately triggered new activities and several ion beam analysis laboratories all over the world started to build dedicated MeV-SIMS imaging setups with the goal to develop and establish a new powerful technique for molecular imaging (Jones, Palitsin, and Webb 2010; Nakajima, Nagano, et al. 2014; Tadić et al. 2014; Jeromel et al. 2014; Eller, Cottereau, et al. 2015; Meinerzhagen et al. 2016; Schulte-Borchers et al. 2016)). Most of these efforts were soon coordinated and gathered under the quickly established IAEA CRP F11019 on 'Development of Molecular Concentration Mapping Techniques Using MeV Focussed Ion Beams'.

The primary focus of the new research is to develop the technique for molecular imaging, combine it with other simultaneous ion beam analysis techniques like Rutherford BackScattering (RBS), Particle-Induced X-Ray Emission (PIXE) and Scanning Transmission Ion Microscopy (STIM), and to apply it in a broad range of fields. Therefore only a few studies investigating the fundamental desorption process were published until now: Jones, Palitsin, and Webb (2010) and Stoytschew, Bogdanović Radović, Demarche, et al. (2016) both observed leucine yields scaling with primary ion velocity similarly to the electronic stopping power of the incident ion, although they mention that measured yields are strongly dependent on the charge state and surface topology of the sample. Jones, Matsuo, et al. (2011) did a comparison with two similar MeV-SIMS beams (performed at different setups) and several widely-used keV-SIMS beams and observed structurally similar secondary ion mass spectra, however with significantly higher yields and less fragmentation in the high-mass region in case of the MeV-SIMS measurements. Finally Nakajima, Miyashita, et al. (2014) performed MeV-SIMS measurements on ionic liquids and concluded from comparison of secondary ion intensities with the surface structure that SIMS employing electronic sputtering provides excellent surface sensitivity on the order of single monolayers - comparable to SIMS techniques utilizing nuclear sputtering.

2.3. Brief overview of theoretical models for sputtering

It had been realized early (Griffith et al. 1980; P. Haff and L. Seiberling 1981), that the collision cascade model for nuclear sputtering as developed by Sigmund (1969) was not applicable for electronic sputtering with yields frequently underestimated by orders of magnitude. To this day, the very fast and highly non-equilibrium processes involved in electronic sputtering are poorly described, despite there being many different theoretical approaches. A comprehensive overview of the theoretical concepts involved was compiled by Wien (1989), distinguishing between six classes of models (which are however not mutually exclusive and can have considerable overlap):

- Transition state theory considers the transfer of excitation energy via intermediate states to exothermic final states of the atomic system that then lead to the ejection of particles.
- Coulomb explosion models describe the desorption in terms of an coulomb repulsion driven explosion of the positively ionized core region along the track of the projectile. This induces a low energy atomic collision cascade creating a radially expanding shock wave that leads to ablation at the surface of the sample material.
- Thermal spike models characterize the highly energized core region along the projectile track with its steep energy density gradient by temperature and consider the formation of a plasma. Secondary ion desorption then occurs as an evaporation or sublimation process from this core or the neighbouring regions driven by heat conduction.
- Expansion models depict the expansion of excited molecules or an assembly of atoms and the subsequent pressure enacted on the material lattice or neighbouring molecules. Directly at the surface of the sample material this expansion can even lead to self-repulsion and desorption of the molecule.
- Excitation models consider the possible desorption via decay of individual excitations into repulsive states, which in the high-energy regime can be populated for example by high frequency perturbations of a generated electron plasma.
- Grain models attempt to attribute the occasionally significant differences in experimentally measured yields to grains or microcrystals in the sample material, which are desorbed as a whole if the deposited energy is large enough to evaporate all grain atoms collectively.

The earliest treatment of electronic stopping was in the context of a thermal spike model inducing evaporative sputtering (Johnson and Evatt 1980; Toulemonde, Paumier, and Dufour 1993; Toulemonde, Assmann, Dufour, et al. 2012). They considered that a significant part of the stopping power deposited in the electronic subsystem of the material is converted

into heat, resulting in a localized temperature spike within the sample material, activating an evaporative desorption process with subsequent cooling by conduction. Later models applied fluid dynamics to explain electronic sputtering in terms of a correlated pressure pulse or shock wave within the sample material (Bitensky and Parilis 1987; Reimann 1995) and many models require a critical energy density (L. E. Seiberling, Griffith, and Tombrello 1980) or pressure (Fenyö and Johnson 1992) to activate secondary ion desorption. As demonstrated by Jakas, Bringa, and Johnson (2002), the strong temperature and density dependence especially in the vicinity of the sample surface - which is usually not well represented in standard models considering targets of infinite dimensions - limits their applicability to predict quantitative yields. In addition to the semi-analytical models, molecular dynamics (MD) simulations based on thermal spike models were used to reproduce some of the experimentally obtained data results on sputtering yields (H. M. Urbassek 1997; Fenyö and Johnson 1992; Bringa and Johnson 2000).

An overview of the more recent theoretical approaches and comparison with experimental data was given by Daya et al. (1997): The sputtering is characterized as a very complex interaction by which positive and negative fragments and even intact molecular and cluster ions and neutrals are ejected quickly after the impact of the incident primary ion. It is mentioned that the sputtering yield of neutral secondary particles scales approximately with $\propto \left(\frac{dE}{dx}\right)^3$, with the cubic scaling being in line with the predictions of a pressure pulse model. Point of origin information suggests that at least the positive fragment ions orginate from the crater regions of the ion impacts. However the widths of those craters scale with $\propto \left(\frac{dE}{dx}\right)^{0.5}$, which is more in line with a thermally activated and dispersive evaporation process. Positive and negative fragment ions do seem to behave differently with regard to their respective radial velocity distributions suggesting a non-equilibrium ejection pattern directed away from the incident ion path for the positive ions and a thermal signature in the ejection pattern of the negative ions. Daya et al. (1997) conclude that each individual impact induces processes which can be characterized partly by an evaporative spike and partly by a pressure pulse.

A similar view had already been presented with the analytical model of Johnson, B. U. R.

Sundqvist, et al. (1989), where the summing of impulses lead to a two-stage model in which an initially heavily disturbed system can be described by a coulomb explosion model, before a correlated response of the sample material emerges after some time when the extremely high excitation density energizes also the surrounding region of the impact site. However the resulting yield scaling with $\propto \left(\frac{dE}{dx}\right)^3$ at very high $\left(\frac{dE}{dx}\right)$ is at odds with more recent molecular dynamics simulations which rather suggest a roughly linear scaling (Gutierres et al. 2017).

To make comparisons with measured data even more difficult, most of the theoretical models focus on the desorption effect and largely neglect the ionization process, while most of the experimental data describes charged particle yields and therefore a convolution of both processes. Additionally, fragmentation effects are intertwined with the ejection processes and additionally change the yield of secondary ion species. It is expected (Lima et al. 2016; Papaléo et al. 1996) that the degree of fragmentation increases with the transient local energy density in the ion track, suggesting that larger molecular secondary ions are more likely to originate from the outer regions of the primary ion track in the sample material.

From an outside phenomenological perspective, a picture as shown in figure 2.2 emerges: A single primary ion impacts the sample surface and produces a track with a diameter on the order of 10 nm, in which a significant amount of energy is deposited into the electronic subsystem of the sample material at extremely short ($< 10^{-15}$ s) timescales.

Within the core region around the nuclear track, the so-called *infratrack* with a diameter of a few nm this results in a very intense ionisation and excitation due to direct coulomb interaction with the projectile ion. The size of this infratrack region depends primarily on the primary particle velocity. Additionally, high energy electrons (δ-electrons) are generated in this region by close distance collisions with the projectile ion. These carry the excitation radially outwards into the surrounding material and produce subsequently secondary electrons in the *ultratrack*. The size of this outer zone is determined by the maximal projected range of the δ-electrons in the sample material and the electronic excitation density should decrease roughly $\propto \frac{1}{r^2}$. The very high resulting energy density in the ion track and its steep gradient potentially induce material responses manifesting in both thermal- and pressure-like effects.

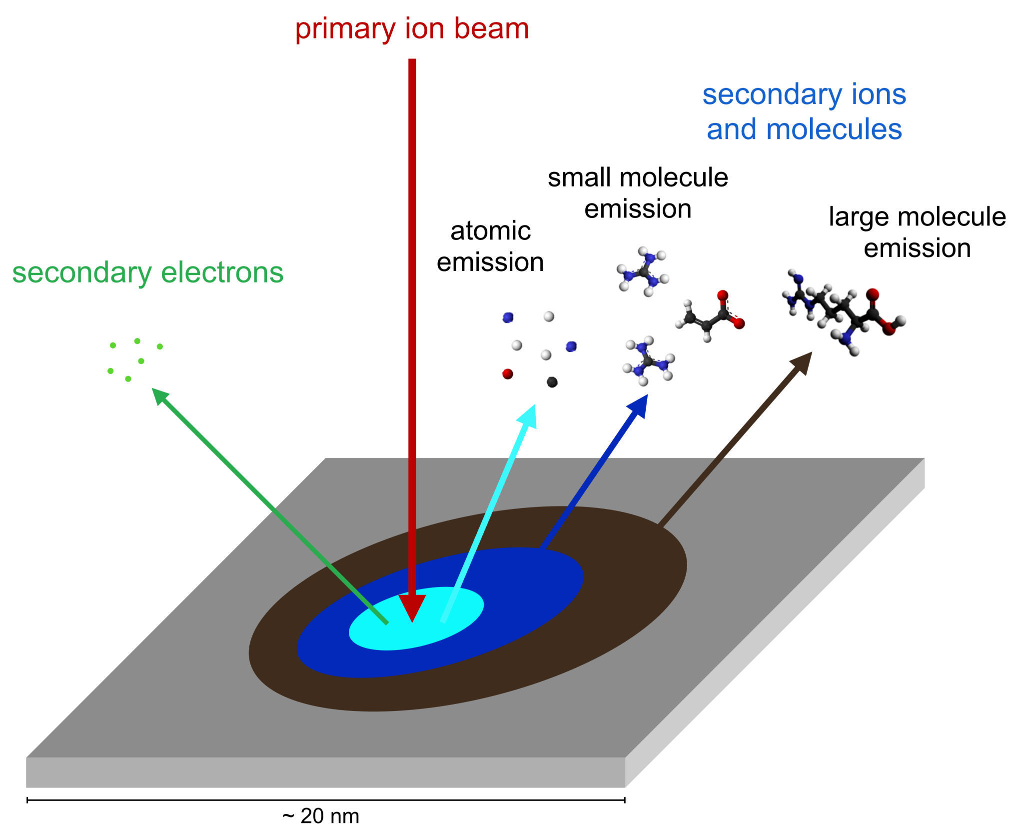

Figure 2.2.: Secondary ion and electron desorption in MeV-SIMS (figure design after Johnson and B. U. R. Sundqvist (1992)).

The contribution of each specific effect is most likely strongly dependent on the type and properties of the sample material, however collectively they lead to the desorption - and for a fraction of the ejected material also to ionization - of secondary particles. These range from electrons, monomer atoms and small fragment molecules via larger and full-mass molecules all the way up to even chunks and clusters of molecules originating from the sample material. A significant fraction of the ejected material seems to originate from within the infratrack respectively the crater region that is formed on the sample surface where the strong ionization and nuclear collisions leads to strong fragmentation of the secondary ions. But it is likely that larger molecular particles are primarily originating from the outer ultratrack regions further away from the primary ion impact site, where fragmentation effects are assumed to be less dominant. There the desorption of larger molecules and clusters is enabled by a combination of electronic excitation weakening the intramolecular bindings and atomic movement (due to a material response like a pressure pulse, collision cascade or coulomb explosion) providing the kinetic energy to overcome the remaining adhesion and desorb intact molecules and clusters from the surface.

3. MeV-SIMS at ETH Zurich: The CHIMP setup

The **C**apillary **H**eavy **I**on **M**eV-SIMS **P**robe (CHIMP) setup is installed at the 6MV TANDEM accelerator facility at the Laboratory of Ion Beam Physics at ETH Zurich. It was originally designed and built in the years 2015/2016 within the scope of the PhD thesis 'MeV-SIMS based on a capillary microprobe for molecular imaging' (Schulte-Borchers 2016). Since the setup has been significantly modified and upgraded throughout the work of this thesis, in the following a rather general overview of the accelerator facility (Section 3.1) and the preparation of the primary ion beam (Section 3.2) will be given before two specific setups will be discussed in more detail: In Section 3.3 the status of the setup in spring of 2018 is described. This setup has been used for most of the yield and fragmentation measurements discussed in Chapter 5 (some improvements with respect to the initial setup as existing in 2016 are discussed in Appendix A). Secondly in Section 3.4 the upgraded setup with dual ToF mass spectrometers for simultaneous detection of electrons as well as positive and negative secondary ions is described. This represents also the current status of the Dual-CHIMP setup.

3.1. Layout of the TANDEM accelerator facility

A schematic overview of the 6 MV TANDEM accelerator facility is shown in figure 3.1: The facility is equipped with a high-current Cs sputter ion source (HCS) which provides a wide range of atomic and molecular ion beams. The extracted beam is analyzed on the low energy (LE) end of the accelerator by a 45° electrostatic analyzer and the 90° LE magnet. The 90° LE magnet chamber is additionally equipped with an electrostatic switching system ($f_{max} = 333\,\text{Hz}$), which can be used to sweep the beam across downstream slits to provide a pulsed primary ion beam. The beam is then focussed by two einzel lenses and a quadrupole

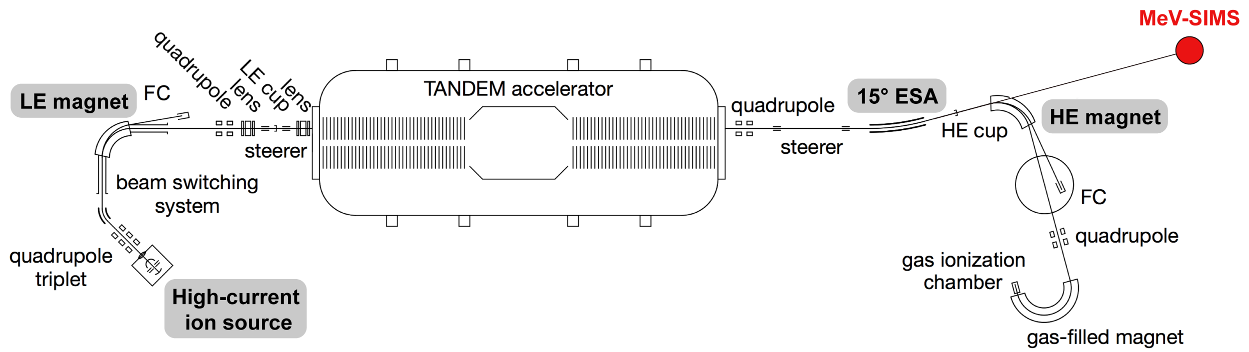

Figure 3.1.: Schematic of the 6 MV TANDEM accelertor facility at ETH Zurich.

lens into the tandem accelerator. On the high energy (HE) end of the accelerator, the beam focus can be adjusted using a second electrostatic quadrupole lens system, before it is analysed by a 15° electrostatic analyzer (ESA). The MeV-SIMS chamber is located at the 0° port of the following 90° HE magnet used for accelerator mass spectrometry (AMS). Thus, all HE beam guiding and analysis components are only acting with respect to the E/q ratio of the ions.

This rather unique setup of the accelerator facility enables the use of a wide range of different primary ion beams at the CHIMP MeV-SIMS setup: At the low energy spectrometer the mass of the primary ions is only limited by the maximum magnetic field of the LE magnet ($\frac{m \cdot E}{q^2} < 15\,000\,\mathrm{u} \times \mathrm{keV}/e^2$). To deflect the heavy C_{60} cluster ions in charge state $q_{LE} = 1-$ the HCS source extraction energy is reduced to 20 keV. Since the high energy end of the accelerator only consists of electrostatic ion optical elements, large and heavy molecular or cluster ions can be accelerated and subsequently guided to the MeV-SIMS setup. The final collimation and attenuation of the primary ion beam in front of the sample by means of apertures and/or tapered glass capillaries is also independent of mass and energy of the ions. Therefore the use of primary monoatomic ions with energies of close to 80 MeV or cluster ions with energies of up to 15 MeV is possible. The maximum energy achievable for cluster ions is limited due to the capability of the 15° HE ESA to deflect ions in charge state $q_{HE} = 2+$, which is the highest realistically achievable charge state for many cluster primary ions.

3.2. Preparation of the primary ion beam

The beam focus at the high energy end of the accelerator is primarily determined by the Terminal Voltage (TV) of the Tandem accelerator and the setting of the einzel lenses and HE quadrupole focussing elements. For operation in the MeV-SIMS chamber, the focal point of the beam is shifted downstream from its usual position right after the 15° ESA to a pair of slits located 0.5 m upstream of the MeV-SIMS measurement chamber (Figure 3.1). Since the beam still has to pass a ±1.5 mm slit opening located at the 15° measurement chamber 5 m upstream of the capillary, this constrains the beam divergence significantly: In case of a micron sized capillary opening in front of the sample, the maximum angle of directly transmitted ions is always below 0.3 mrad (Miltenberger et al. 2017). A retractable Faraday Cup enables tuning of the primary ion beam at this point and the beam-halo signal picked up by a second pair of slits can be fed back into the TV controller of the Tandem accelerator for beam stabilization.

To obtain a micrometer sized primary ion beam, a collimator within the CHIMP measurement chamber itself is available. Two different approaches have been used within the scope of this work: collimation using a glass capillary as well as collimation using a pair of micrometer sized apertures.

3.2.1. Collimation using a glass capillary

The technique of ion beam collimation with a glass capillary is relatively straightforward and inexpensive. For ion beams of MeV energy the use of a capillary-based microbeam was first reported by Folkard et al. (1995). In the following years the technique gained some attention and was applied to produce a microbeam for a wide range of different ion beam analysis and modification techniques like PIXE, NRA, RBS, STIM, irradiations and proton beam writing (Hasegawa, Shiba, et al. 2008; Hasegawa, Jaiyen, et al. 2011; Nebiki, Yamamoto, et al. 2003; Nebiki, Kabir, and Narusawa 2006; Nebiki, Sekiba, et al. 2008; Sekiba et al. 2008; Fujita, Ishii, and Ogawa 2009; Fujita, Ishii, and Ogawa 2011; Ikeda, Kanai, Iwai, et al. 2011).

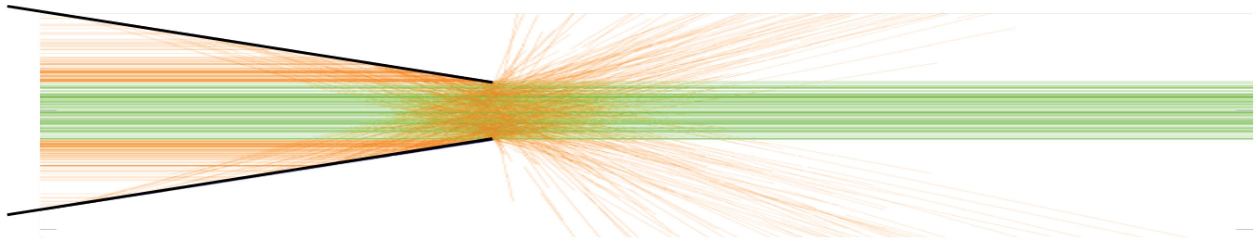

Figure 3.2.: Simulated transmission of MeV ions through a tapered glass capillary (Simon 2013).

All of these studies used comparably light primary ions like protons, He or N. The first, and very comprehensive study of heavy ion collimation with glass capillaries was done by Simon, Döbeli, et al. (2012). The comparison with Monte-Carlo simulations concluded that the main effect is a collimation of the primary ion beam by the glass capillary and that there is no additional focussing effect (compare Figure 3.2). This means that for capillaries with outlet diameters on the order of µm, the intensity of the ion beam is reduced from a particle current of p µA down to p fA. However this does not represent a problem for efficient IBA techniques like PIXE and MeV-SIMS which need only a very small amount of primary beam.

The collimation effect is completely independent of the mass and energy of the primary ion beam being collimated, so the technique is ideally suited to work with a wide range of very heavy and energetic (cluster) ions.

The transmitted ion beam consists mainly of the central beam component and an additional beam halo that originates from ions scattered at the inner capillary walls, which thus depends on the specific shape of the capillary. Due to the absence of any guiding or focussing effect the central beam component of the transmitted ion beam has a very low divergence (transmission through a typical capillary is only possible over a range of 0.2° around the beam axis), while the influence of the halo with higher divergence and generally much lower intensity can be reduced by an increased distance between the capillary outlet and the analysed sample. For high energy light ions and thin capillaries a transmission through the sidewalls at the tip of the capillary is in principle possible, but this can be recognised by measuring the energy spectrum of the transmitted ion beam and is generally not a problem for heavier ions.

Additionally, a capillary with sufficiently small outlet diameter can also be used as a vacuum-

air interface by means of differential pumping and therefore represents a very suitable candidate for ambient-pressure microprobes (Simon, Döbeli, et al. 2012).

For the scope of this work a range of self-manufactured glass capillaries were used. Starting from commercially available straight constant bore borosilicate glass capillaries, they were drawn into a tapered shape with a vertical puller instrument and finally cut at the capillary outlet with a microforge. The detailed production process is described in Appendix B.

The capillaries used for the measurements in this thesis feature a range of different outlet diameters from 250 µm (a straight, unpulled capillary) down to approx. 5 µm, while capillaries with outlet diameters as low as 2 µm could be successfully produced. The transmission capabilities of all capillaries were tested by measuring the energy spectrum of MeV protons transmitted through the capillary into air at a dedicated beam station with a silicon PIN diode detector before installation in the MeV-SIMS setup (see Appendix B for example spectra).

To get a good transmission it is critical to be able to adjust and align the capillary to be collinear to the incoming primary ion beam. In the CHIMP measurement chamber this was solved by mounting the capillaries into a screw mount seated on top of an angular adjustable positioner stack. The stack consists of a piezo goniometer (ECGt5050, attocube systems AG, Haar, Germany) and a rotator (ECR5050, attocube systems AG, Haar, Germany) which allow to tilt the capillary in both vertical (goniometer) and horizontal (rotator) direction.

Meanwhile the capillary mount is positioned such that the capillary entry occupies the pivot point and thus stays fixed relative to the measurement chamber and beamline. The capillary can then be pre-aligned using either a laser beam inflected by a mirror into the beamline or using a beam axis telescope when the transmission detector is removed. This optical alignment is usually accurate enough to transmit at least a small fraction of the ion beam in the transmission detector, so that the fine tuning can be done by maximising the count rate of an actual ion beam in the transmission gas ionisation detector (GID).

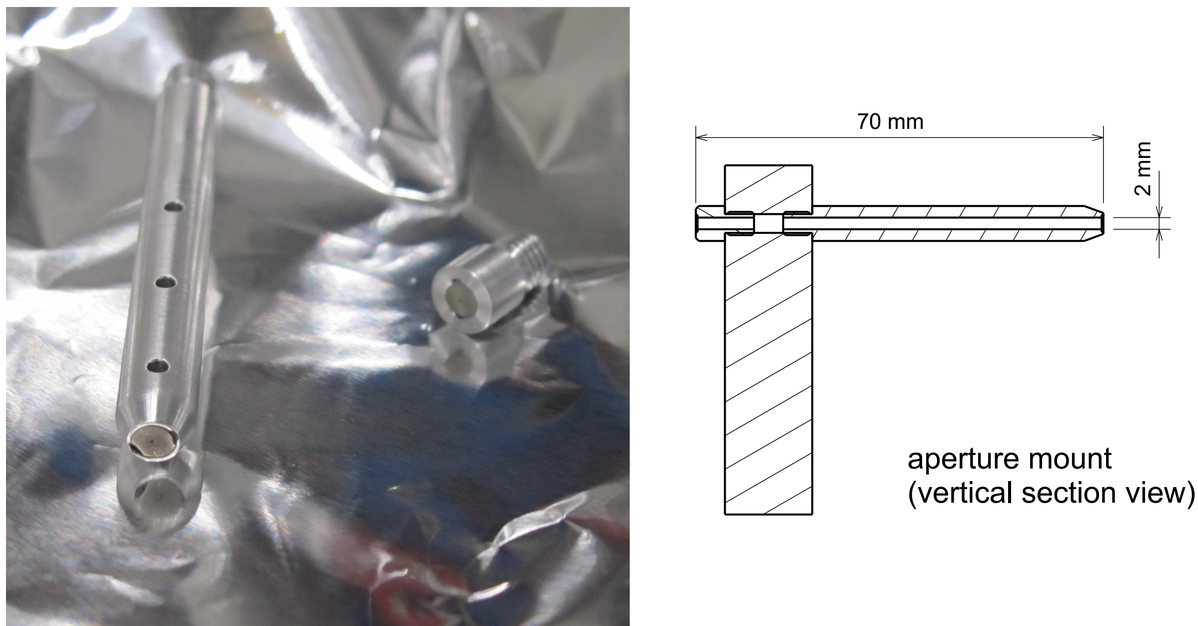

Figure 3.3.: Image of 250 µm apertures mounted on two-part beam tubes and sectional view of the assembled mount.

3.2.2. Collimation using micrometer apertures

Collimation of an ion beam with apertures is actually the most straightforward possibility, although slit scattering can significantly deteriorate the quality of the transmitted beam. Nevertheless, it has been demonstrated (Nobiling et al. 1975) that collimation of MeV ions to micrometer sized beams with very low divergence and excellent beam quality is possible with a properly designed setup.

For the purpose of the described MeV-SIMS setup, a set of two molybdenum micrometer apertures as used in electron microscopes were used (Plano GmbH, Wetzlar, Germany). The apertures have only a thickness of about 0.1mm (which should minimize slit-scattering) and are readily available down to diameters of 10 µm. They were then mounted on two small tubes that can be screwed into the existing screw mount that is also used for the capillaries (see Figure 3.3). This positions the apertures at a distance of 7 cm apart from each other, such that scattered ions from the first aperture are stopped by the second one. The whole mount can once again be positioned using the goniometer and rotator stack to align the set of apertures with the incoming beam direction.

3.3. Initial setup: Positive mass spectrometer with electron start

The setup of the CHIMP measurement chamber in spring of 2018 is schematically shown in figure 3.4. This setup is mechanically largely identical with the status as described in Schulte-Borchers (2016) and Schulte-Borchers et al. (2016). However, several changes were made to the high voltage configuration at the positive ion ToF mass spectrometer and additional mechanical shields have been installed to prevent electrons from the beamline and slits to enter the CHIMP measurement chamber.

3.3.1. The measurement chamber

The measurement chamber is of cylindrical form with a large top and bottom flange to access the setup. Centered inside the chamber the sample holder is mounted on a *x*-*y* piezo sample stage that consists of two linear positioners (ANPx321NUM, attocube systems AG, Haar, Germany) connected using an L-shaped joint to enable 2D movement of the sample in horizontal and vertical direction within a fixed plane oriented normal to the incident ion beam. The sample holder itself accepts samples mounted on an omicron-type flag style sample plate.

To change the sample, the complete sample holder stack including the piezo stages can be moved out of the primary ion beam on a manually driven linear stage. In the off-center position, the sample can be gripped using the pincer of a Dual Shaft Wobblestick (Ferrovac GmbH, Zurich, Switzerland) and transfered to a five-sample magazine located inside the main measurement chamber. The magazin itself can be moved into a separate entry lock vacuum chamber using a Sample Transporter (Ferrovac GmbH, Zurich, Switzerland). This entry lock chamber is segregated from the main measurement chamber by a vacuum valve and equipped with its own turbomolecular pump, such that it can be vented and evacuated independently to load samples into the sample magazine.

The primary ion beam passes two pairs of slits and a rectractable Faraday Cup before it

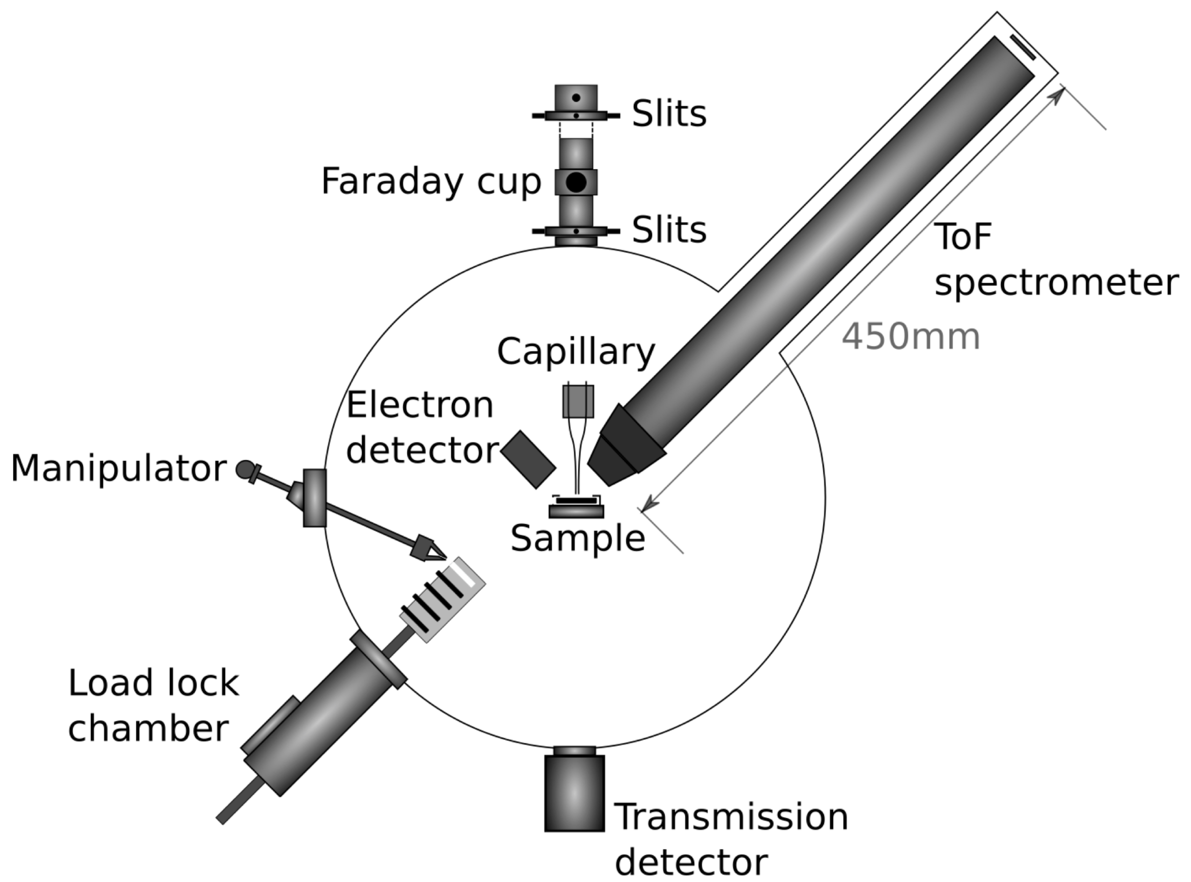

Figure 3.4.: The CHIMP measurement chamber viewed top-down with the primary ion beam entering from the top (Schulte-Borchers 2016).

enters the chamber through the flange depicted at the top of Figure 3.4. It can then be collimated using either a tapered glass capillary or a set of apertures mounted inside the measurement chamber as discussed in Section 3.2. Both can be interchangeably mounted on a piezo stage stack to adjust their pointing direction to be parallel to the incident primary ion beam.

Finally the measurement chamber is equipped with two particle detectors (in addition to the positive ion ToF mass spectrometer mounted in 45° backscattering geometry): a Gas Ionization Chamber (GIC) detector in tranmission geometry and an electron Channeltron detector.

Transmission Gas Ionization Chamber detector

The Gas Ionization Chamber (GIC) detector is mounted in transmission geometry directly behind the sample mount. The detector volume is separated from the chamber vacuum by a 50 nm, $4 \times 4\,\mathrm{mm}^2$ SiN window and the whole detector can be moved in x (horizontal) and y (vertical) direction with respect to the beam axis. Based on the very low beam divergence one can thus assume that a very large fraction (>95 %) of the primary beam ions are detected in the GIC detector when utilizing a capillary or microapertures for collimation. Therefore, the GIC was used throughout all measurements to quantify the incident primary ion count rate while the sample is moved out of the beam using the linear sample stage. Additionally it can be also used to measure primary ions transmitted through a thin sample.

Electron Channeltron detector

On the right hand side of the sample (when seen in primary ion beam direction) an electron Channeltron detector (model KBL505, Dr. Sjuts Optotechnik GmbH, Göttingen, Germany) is mounted in 45° backscattering geometry to detect secondary electrons emitted from the sample upon impact of a primary ion. A positive high voltage is applied to the $5 \times 5\,\mathrm{mm}^2$ Channeltron inlet such that secondary electrons emitted with low energies are extracted from the volume in front of the sample towards the detector.

3.3.2. The positive ion ToF mass spectrometer

The positive ion ToF spectrometer (pToF) was home-built and features a two-stage extraction with two pairs of electrostatic steerers in horizontal and vertical direction to direct the ions onto the positive ion micro-channel plate stop detector (pMCP). It is mounted mirror-symmetrically to the electron detector on the left hand side of the sample (seen in primary ion beam direction) under an angle of 45° in backscattering geometry. This arrangement enables the operation of the ToF spectrometer in several different modes as described in Schulte-Borchers et al. (2016): Either with a pulsed primary ion beam with the ToF start signal provided by the pulsing signal or with a continuous primary ion beam. In the second case the Channeltron detector (eCT) provides the ToF start signal origniating from secondary electrons. For thin samples the ToF can even be started using the signals of transmitted primary ions in the GIC detector.

Mechanical and electrical design

Mechanically the positive ion ToF is separated in three different segments (see Figure 3.5): The first segment is mounted inside the actual measurement chamber and consists of a two-stage extraction cone with respective applied voltages Cone 1 and Cone 2. Generally the negative high voltage applied to Cone 1 counteracts the high voltage applied to the electron detector mounted on the opposite side of the incoming beam to enable the extraction of both negative electrons and positive ions from the impact point on the sample surface. Extracted ions are then accelerated to the second part of the extraction (Cone 2) with the voltage also applied to a field-forming wire grid and aperture placed between the two sections. Afterwards the ions pass a pair of electrostatic deflector plates set up in vertical and horizontal direction and are steered onto a straight path into the ToF flight tube. A simulation of the electrostatic field configuration is shown in Figure 3.5 (left).

The second part of the spectrometer, consisting of the field free flight tube of 455 mm length, is mounted inside a CF100 extension vacuum tube connected to the measurement

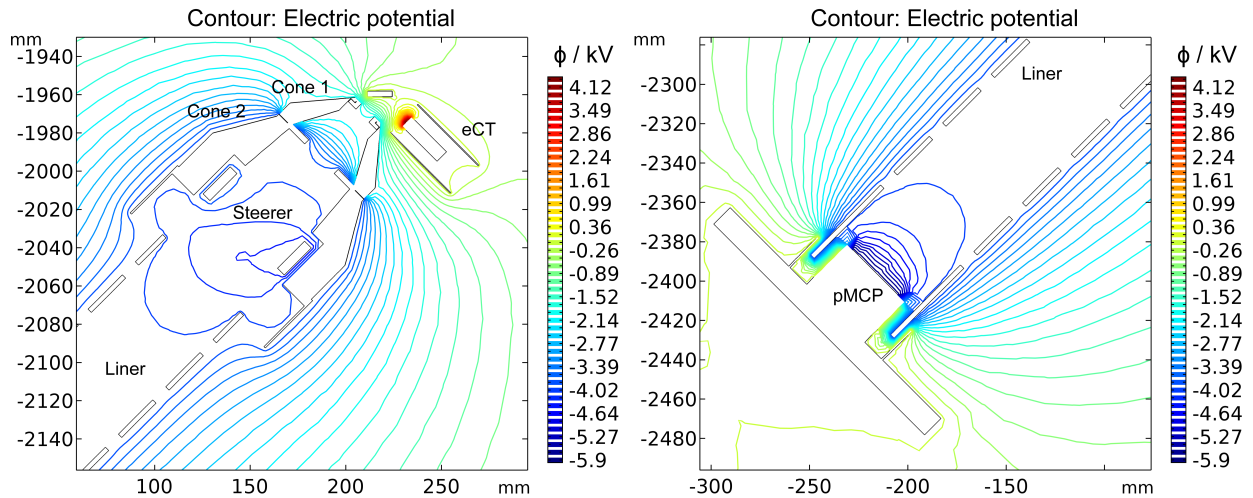

Figure 3.5.: Simulation of electric potential configuration in the extraction region (left) and around the MCP (right) of the pToF mass spectrometer generated with Comsol Multiphysics.

chamber. The ion ToF path is enclosed by an electrostatic liner (insulated from the grounded vacuum chamber) with a negative high voltage applied. Finally, the spectrometer is terminated by the ToF stop detector consisting of a dual MCP stack in Chevron configuration (two MCPs type F1094-01, Hamamatsu Photonics K.K., Hamamatsu, Japan). It is mounted directly onto a CF100 flange with the required electrical feedthroughs (signal, pMCP front and pMCP back). The front side of the MCP stack is set a few hundred volts higher than the Liner voltage to focus and accelerate the ions to slightly higher energies just before impacting the MCP and thus increasing detection yield (see Figure 3.5 (right)). The back side of the MCP stack is accordingly set to a lower negative voltage to obtain the required signal gain, while the signal anode is at ground potential.

Signal processing and data acquisition

The signals of the electron detector and pToF MCP detectors are fed into a fast timing amplifier (NIM Model 612 AM, LeCroy Research Systems Corp., Spring Valley (NY), USA), while the signals of the GID detector are amplified using an integrated preamplifier and NIM main amplifier/SCA module. Afterwards the amplified signals of all three detectors (and the optional beam pulsing signal) are converted to timing signals using a constant fraction discriminator (NIM Model 935, Ortec Ametek Inc., Oak Ridge (TN), USA). Finally, the

resulting logical NIM pulses are fed into a fast four-channel digitizer (DT5751, Caen S.p.A., Viareggio, Italy) working in DPP-PSD (Digital Pulse Processing for Charge Integration and Pulse Shape Discrimination) mode. The digitizer issues a time stamp with an intrinsic time resolution of 1 ns for each event once the input channel voltage exceeds a certain threshold. The event data is buffered internally and then read out periodically by the measurement PC connected via USB, running a custom LabView DAQ software. This setup enables the simultaneous and independent aquisition of events across all of the connected channels, which can then be analysed and correlated both, online during the measurement but also (by using the event time-stamp data recorded in listfile format) offline after the measurement is completed.

For the analysis of the acquired data the detector channel that is used as a start for the calculation of the ToF mass spectra can be selected either from the primary beam pulsing, the secondary electron signal or transmission GIC signal. Typically a specific start signal from that channel is selected and then matched up with all possible stop signals within a fixed coincidence time window. The coincidence time has to be chosen short enough that random coincidences are not significantly contributing to the background of the ToF spectrum. However this is not a problem when working with the very low primary ion count rates of a few kHz transmitted through a micrometer aperture or capillary: Coincidence time intervals of 10 μs to 100 μs still provide a decent signal to background ratio in the ToF mass spectra. Additionally, the recording of all events from all available detector channels enables the study of time correlation spectra as well as an estimation of the performance and relative efficiency of the different detectors.

3.3.3. The extraction field geometry and operating parameters

Already from the design of the measurement system it had been clear that with a simultaneous extraction of secondary electrons and positive ions, it would be critical to strike the right balance in setting and tuning the electric extraction fields for both. Since the sample is on

pToF	Cone 1	-1.60 kV	Cone 2	-4.00 kV
	Steerer X1	-3.90 kV	Steerer X2	-4.10 kV
	Steerer Y1	-3.80 kV	Steerer Y2	-4.20 kV
	Liner	-4.00 kV		
	pMCP front	-6.00 kV	pMCP back	-4.00 kV
eDet	eCT front	4.40 kV	eCT back	6.20 kV

Table 3.1.: Operating voltages of the pToF mass spectrometer and eCT channeltron detector.

ground potential, high voltages are applied to both the eCT detector and the pToF extraction cone. In general, these need to be balanced in a way that particles of both polarities emitted by impacting primary ions from the sample surface with very low energies - usual estimates range from 0 eV to 6 eV (Widdiyasekera, Håkansson, and B. U. R. Sundqvist 1988) - are extracted with sufficient efficiency. This also implies that close to the actual impact region on the surface the electric field is very small, resulting in a very high influence of the initial emission characteristics (energy and direction) on the actually measured time of flight of the particle in the spectrometer since the slow moving particles can stay for a significant time in the low-field region.

For all of the measurements referenced in this work (unless specifically mentioned), the high voltages were applied as listed in Table 3.1. From the electric field simulation depicted in Figure 3.5 (left) it is obvious that the applied extraction field is actually not perfectly symmetrical. This specific extraction regime was rather chosen to experimentally optimize extraction efficiencies for both electrons and positive ions while at the same time optimizing mass resolution of the positive ion mass spectrometer under the given geometrical and electronic conditions. As a result, the extraction field at the point of impact on the sample surface was biased towards the ToF extraction cone, improving extraction of positive secondary ions. This results in a more direct and faster extraction for the positive ions while deteriorating the extraction field for the electrons, which are first accelerated along the sample surface towards the right. However, due to their much lower mass and higher applied voltage at the

eCT detector, the impact of an non-optimal extraction geometry on their already very short flight time is much lower than for the flight time of the positive ions.

3.3.4. pToF performance and mass resolution

The performance of the pToF mass spectrometer in terms of time respectively mass resolution and extraction efficiencies is mainly governed by the electric extraction field geometry defined by the extraction voltages applied to the pToF cones and the Channeltron electron detector. The tuning of these voltages is therefore a highly non-trivial multiparameter optimization problem in which a certain compromise between mass resolution and extraction efficiencies has to be targeted. Additionally, operation in the primary beam pulsing and transmission GIC signal start modes results in inferior time and mass resolution when compared to the fast electron start mode due to the pulse length of the pulsing signal respectively the slow signals of the GIC detector (Schulte-Borchers et al. 2016).

The initial analytical optimization and simulations performed to validate the spectrometer design as well as the first experimental verification were discussed in detail by Schulte-Borchers (2016). In summary, while the analytical description of the mass spectrometer should yield a mass resolution on the order of $m/\Delta m \approx 2000$, the SIMION simulations conclude that the actual mass resolution achievable in the current setup is severely limited by the initial kinetic energy spread and emission angle of the secondary ions. Ions ejected with higher initial kinetic energy will experience the lowest flight times in the mass spectrometer, while initially slower positive ions or those ejected towards the positively biased electron detector will experience a delayed extraction from the low field zone around the impact point on the sample. Based on SIMION simulations and assuming initial kinetic energies uniformly distributed between 0 eV to 5 eV and a cone shaped initial velocity distribution along the sample surface normal the realistic mass resolution of the spectrometer in electron start mode had been estimated to be around $m/\Delta m \approx 45$. The validity of these simulations was largely confirmed experimentally with measured mass resolution values on the order of $m/\Delta m \approx 60 - 107$ for optimized

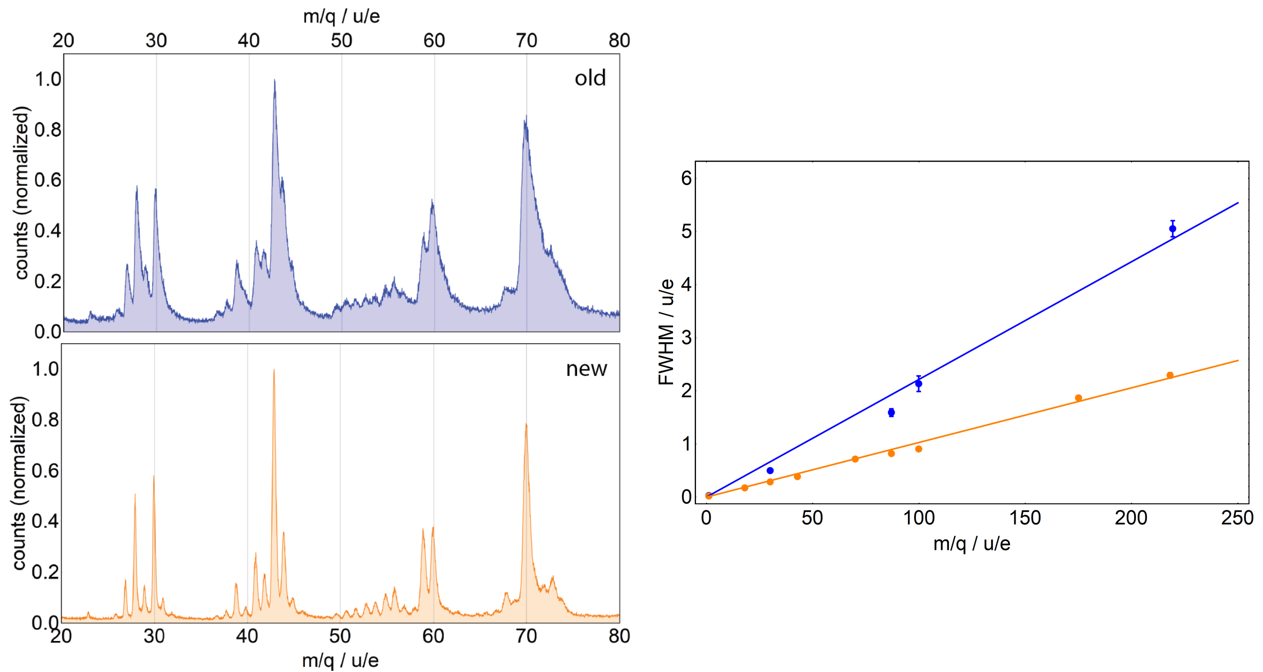

Figure 3.6.: Left: Mass spectra of Arginine recorded with the old and new settings. Right: FWHM of peaks in the mass spectra plotted vs. peak position. The mass resolution with the new settings was determined using a linear fit $m/\delta m \approx 100$ (orange line).

spectrometer parameters on various different samples (Schulte-Borchers 2016). The sample dependent increase in mass resolution observed is likely due to different energy and angular distributions of the emitted secondary ions.

For the measurements performed in the scope of this thesis, mass spectrometer parameter optimization was performed on the arginine sample, since its spectrum exhibits a range of well separated peaks in the mass range between 0 u to 250 u. Initial mass resolution was on the order of $m/\Delta m \approx 45$ and could be improved to $m/\Delta m \approx 100$ by detailed analysis and modification of the electrical ToF setup (see figure 3.6). The modifications performed are described in more detail in Appendix A. The resulting optimized parameters as given in Table 3.1 were used for all following measurements.

3.4. Upgraded setup: Simultaneous dual polarity ToF mass spectrometer with electron start

To study and characterize the secondary ion and electron desorption mechanisms in MeV-SIMS in more detail and especially observe the dependence of positive and negative secondary ion yields from inorganic samples and their behaviour with primary ion cluster size, a novel Dual-ToF spectrometer setup was designed and installed at the ETH Zurich CHIMP setup in fall 2019. The new instrument features two symmetrically arranged linear ToF mass spectrometers for the simultaneous detection of both positive and negative secondary ions originating from the sample.

Only two other dual-polarity simultaneous extraction setups have been reported until now, with one being developed by Tsai et al. (2006) for use with MALDI and the second developed and installed in cooperation with Hiden Analytical (Chater et al. 2014) at a conventional FIB-SIMS instrument. To be able to extract secondary ions of both polarities towards opposite sides under an angle of 45° to the surface normal with both good efficiency and sufficiently small time-of-flight variations, the electric extraction field geometry of the CHIMP setup had to be changed and optimized. The resulting symmetric field distribution is similar to the one used in the FIB-SIMS instrument designed and described by Chater et al. (2014). However, in contrast to both of the above mentioned systems, the setup presented here not only enables the simultaneous extraction of negative and positve secondary ions but also the detection of secondary electrons by separating them from ions in the negative ion ToF spectrometer. This design makes it possible to still use the secondary electrons to generate a start signal for both ToF spectrometers.

A schematic view of the upgraded Dual-ToF spectrometer setup inside the modified CHIMP chamber as of spring 2020 is given in figure 3.7. In comparison to the initial CHIMP setup as described in Chapter 3.3, the entire sample handling and positioning hardware with entry lock, sample magazine, sample manipulator, linear stage and piezo x-y stage remained largely unchanged with the exception of slight modifications to the sample mount itself to improve

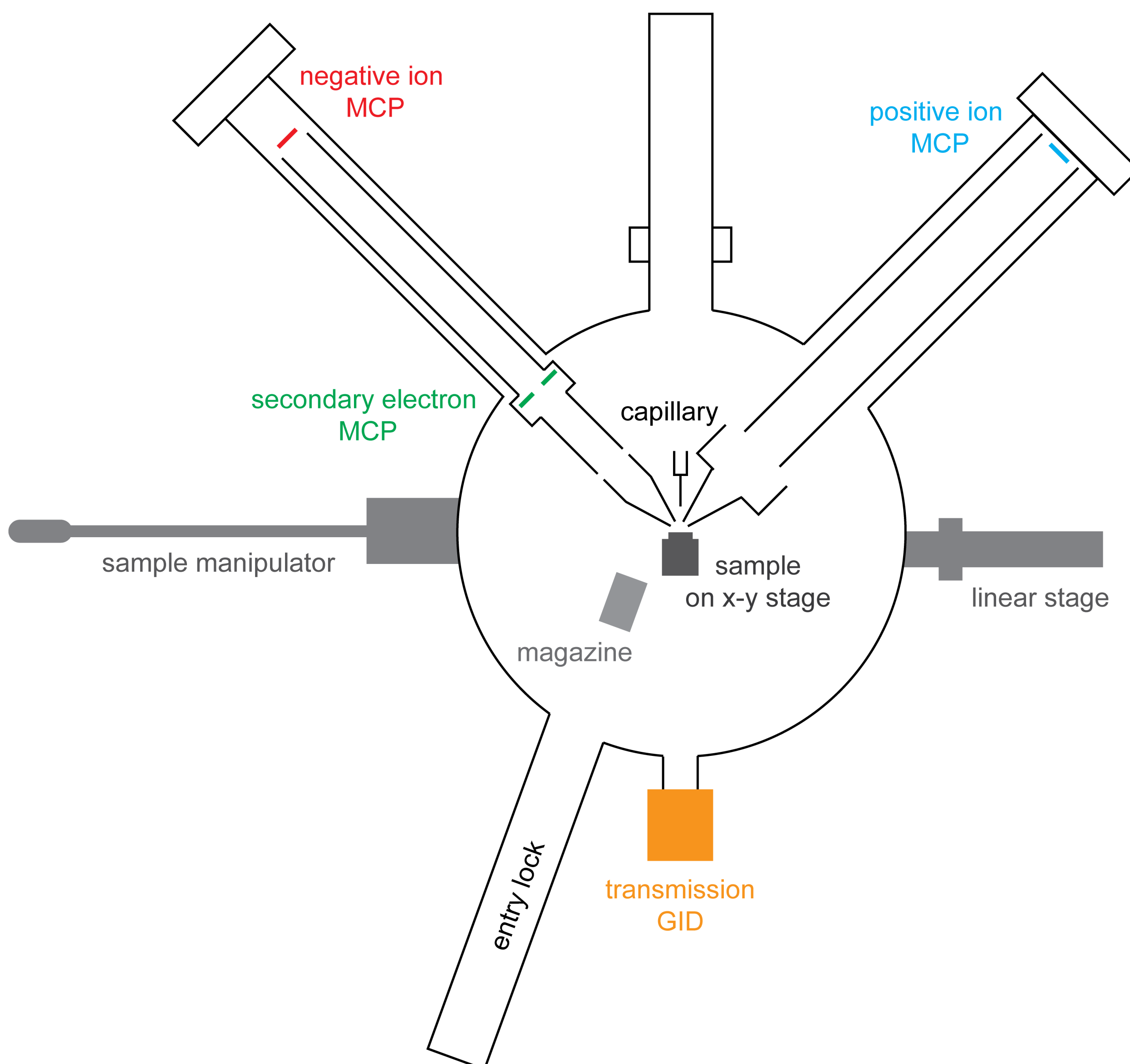

Figure 3.7.: Schematic view of the dual polarity CHIMP setup.

the extraction field geometry. The capillary mount, primary beam shielding and transmission GIC detector also remained unchanged.

The most significant change was the complete removal of the Channeltron electron detector assembly on the positively biased side of the sample. It was replaced by a newly designed linear ToF mass spectrometer. The flight path length was chosen similar to the existing positive ion ToF spectrometer to keep the overall footprint of the CHIMP setup compact and since the overall flight path length is more than sufficient to not limit the flight time resolution of the spectrometer. However the extraction cone geometry was changed to allow for

a more efficient extraction of secondary particles from the impact region of the sample with a symmetric electric extraction field. This also required the refitting of a new corresponding extraction cone design to the positive ion ToF spectrometer to create a mirror-symmetrical extraction region.

3.4.1. The negative ion ToF mass spectrometer and changes to the positive ion ToF mass spectrometer

The negative ion ToF spectrometer was home-built and designed conceptually similarly to the already existing positive ion ToF spectrometer: All the operation modes (pulsed primary beam start, secondary electron start and GIC transmission start) are in principle still available and actually turned out to be very helpful during setup and tuning of the delicate symmetric extraction.

Mechanical and electrical design

Like the existing pToF, the negative ion ToF spectrometer also features a pair of electrostatic steerers in horizontal and vertical direction as well as an einzel-lens formed by the potential difference between the extraction Cone 2 and the ToF liner. However the extraction for both spectrometers was redesigned symmetrically and with the two extraction Cones 1 and 2 concentrically arranged within each other such that a lens effect would improve the extraction field geometry in front of the sample. A CAD render of the cut-open CHIMP measurement chamber is shown in figure 3.8 and provides a good impression of the modified setup.

However a different mechanical design was used: In contrast to the existing positive ion ToF spectrometer the new negative ion ToF spectrometer was constructed such that the whole ToF liner assembly including the extraction cone assembly can be removed as one piece through the corresponding CF65 flange of the CHIMP measurement chamber. To enable a fine positioning of the nToF extraction cone with respect to the sample and pToF extraction cone, the negative mass spectrometer liner is fixed inside the measurement chamber with an

x-y adjustable mounting bracket which also supplies the contacts for the Cone 1 and Cone 2 potentials. At the base of this mouting bracket the optional 15° angled electromagnet coil for electron separation can be mounted. The extraction cones and the nToF liner are connected rigidly using an external shell, with the different components electrically insulated by concentrically aligned ceramic beads. The electrostatic steerer plates are cylindrical half shells and integrated into the first part of the small-diameter ToF liner tube, before it connects to the second part extending into an CF65 extension crosspiece of the measurement chamber via the integrated electron MCP housing. The electron detector consists of a dual annular MCP stack in Chevron configuration (two MCPs type PS34099 with 50 mm outside diameter and 15 mm center hole diameter, Photonis Scientific Inc., Sturbridge, MA, USA) mounted inside an insulating cup. To not disturb the flight path of the negative ions passing through the MCP center hole it is covered with a metal insert held on the liner potential. The whole detector assembly is integrated into a single piece connecting the first and second part of the ToF liner flight tube which is mounted isolated from the grounded vacuum chamber. At the end of the nToF mass spectrometer, the stop detector consists of another dual MCP stack in Chevron configuration (two MCPs type F1094-01, Hamamatsu Photonics K.K., Hamamatsu, Japan) and is mounted directly onto a CF100 flange. Signals from both positively biased detectors are coupled out from the high voltage and transfered to ground potential via high voltage capacitors.

Changes to the signal processing and data acquisition

No fundamental changes were made to the signal processing: The decoupled signals of both, the new eMCP electron detector and the nMCP ToF stop detector, are treated identically to the pToF MCP signal by first amplifying them using a fast timing amplifier before they are detected using a constant fraction discriminator. The logical NIM pulse timing signals of all four channels (eMCP, nMCP, pMCP and transmission GIC resp. beam pulsing) are fed into the same four-channel digitizer. So in comparison to the initial single-polarity CHIMP setup one additional detector channel (the nMCP stop detector) is acquired and the LabView DAQ

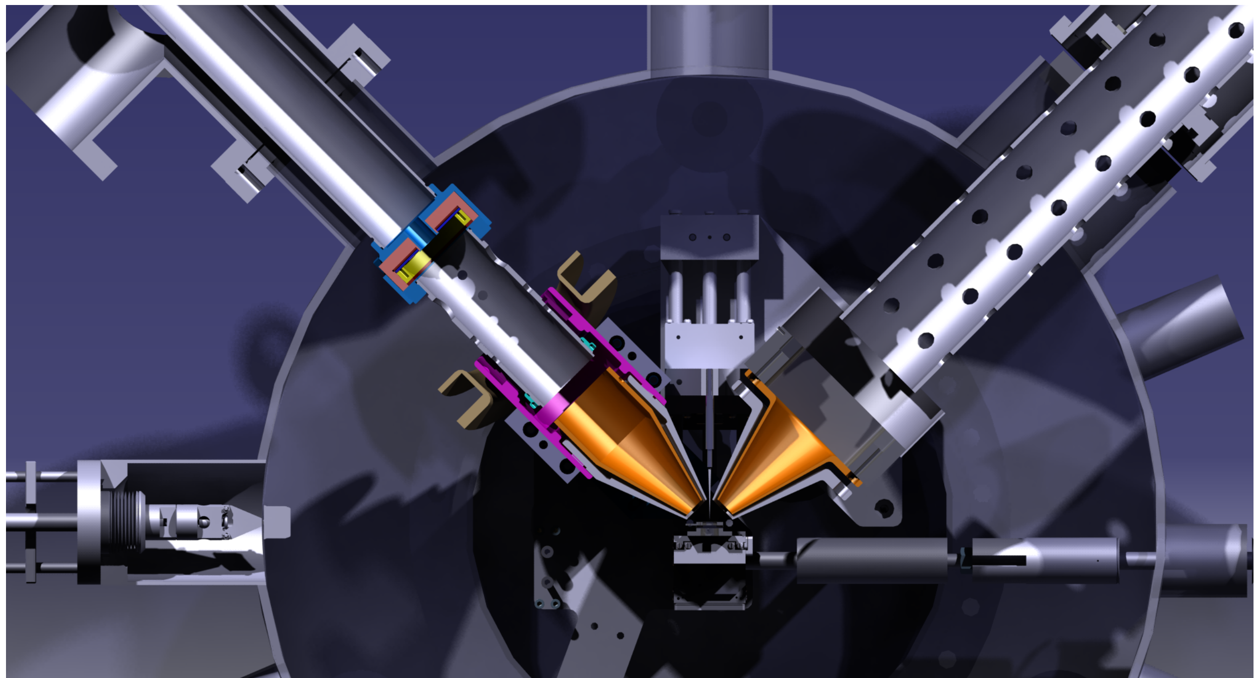

Figure 3.8.: CAD render of the CHIMP chamber with dual mirror-symmetrically arranged mass spectrometers.

software was changed accordingly. Using the event time-stamp data in offline mode it is therefore possible to analyse event correlations between all four separate detector channels, which proved to be quite beneficial during initial setup and tuning of the extraction for the new dual-polarity ToF setup, especially for optimizing and verifying a good electron / negative ion separation. During routine analysis again a single start signal is chosen and then matched up with all possible positive and negative stop signals within a fixed coincidence time window to obtain both positive and negative secondary ion mass spectra.

3.4.2. Simulation of extraction field and secondary electron separation

The two specific requirements of (i) symmetric extraction and (ii) separation of electrons and negative ions are the most notable features of the new DualToF system, requiring careful simulation and optimization and therefore are briefly discussed in the following.

Symmetric extraction geometry

Already from the simulation of the operating conditions of the initial pToF spectrometer (see Figure 3.5) it was apparent that the electric field created in the extraction region was not perfectly symmetrical with regard to the point of primary ion impact on the sample but rather biased towards the positive extraction i.e. the pToF spectrometer. In single-polarity operation this configuration provided two key benefits: Secondary electrons would be actively pushed away from the region in front of the impact point on the sample surface and towards the Channeltron electron detector. This boosted the secondary electron extraction efficiency and therefore the coincidence count rate of the secondary ion spectrum. Additionally, the biased extraction results in a rather homogeneous extraction field configuration towards the pToF spectrometer with almost parallel electric potential lines. This ensures a rather direct and uniform extraction of the (heavier) positive secondary ions from the region in front of the impact point on the sample and therefore minimizes the flight time variations caused by the initial kinetic energy distribution of the emitted secondary ions.

However for the modified CHIMP setup with extraction of both positive and negative secondary ions towards opposite sides of the sample, such a biased extraction would severely limit both efficiency and mass resolution of one of the two mass spectrometers. Therefore, the goal had to be to achieve an almost perfectly symmetrical electric field configuration that still provides a reasonably good extraction of secondary ions from the region in front of the primary ion impact point on the sample. To achieve this the extraction cone geometry of both ToF spectrometers was changed to a design with concentrically arranged cones such that the higher extraction potential applied to the inner cone reaches through the outer cone opening and shapes a convex extraction field in the region between the sample and extraction cone. This also results in a einzel lens effect which can be used to already pre-focus the secondary ions and should increase the extraction efficiency for ions emitted with a broad initial velocity distribution. A 2D simulation of the resulting electric potential in the extraction region in front of the sample performed with Comsol Multiphysics is shown in Figure 3.9.

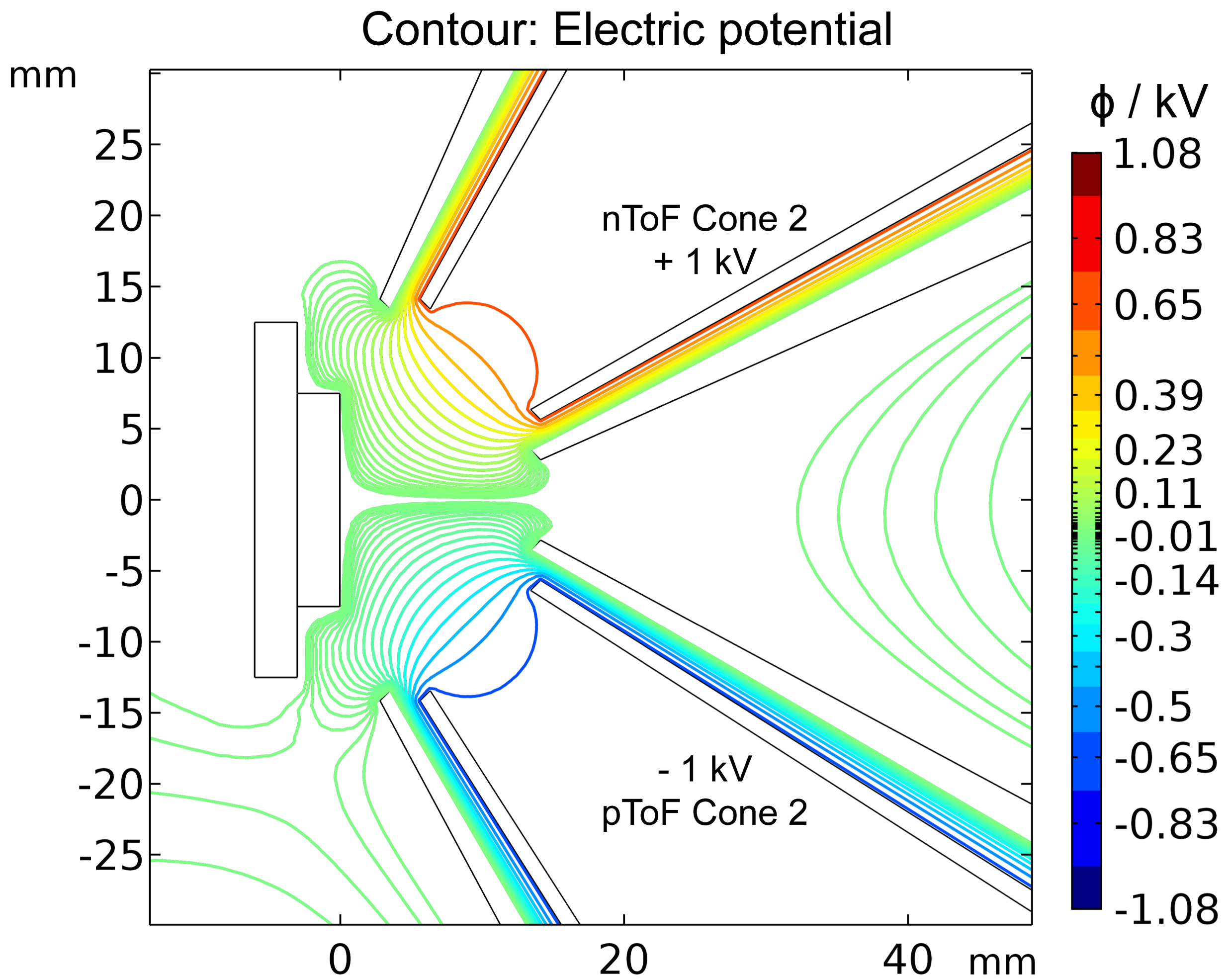

Figure 3.9.: 2D electric potential simulation of the extraction region in front of the sample stage.

Separation of electrons and negative ions

To distinguish secondary electrons emitted from the sample surface from negative secondary ions a spatial deflection of the (much lighter and faster) electrons inside the negative ion ToF spectrometer (nToF) was chosen. In this design, the secondary electrons and negative ions are extracted together from the region in front of the sample through the nToF extraction cone assembly. Therefore they both experience the same extraction field and should have similar extraction efficiencies as long as there are no significant magnetic fields present. After the focussing einzel lens formed by the potential difference between inner extraction cone and ToF liner, the electrons are separated from the negative ions by means of an externally applied magnetic field. The electrons are then deflected onto the annular MCP electron detector (eMCP).

The functionality of the chosen design was verified using the particle tracing simulation module available in Comsol Multiphysics. An exemplary particle tracing simulation is shown in figure 3.10. Through simulations it was determined that influence of the earth magnetic field at the spectrometer location at ETH Zurich would be sufficient to provide good separation of the secondary electron and negative ion beam in the plane of the annular MCP detector (see figure 3.10). However, to be able to tune the electron separation, two additional mechanisms were planned: The generation of an additional external magnetic field by either the application of a set of permanent magnets on the outside of the nToF flange or by means of a concentric coil positioned around the nToF and tilted 15° with respect to the negative ion flight path. The application of an electric current to the electromagnet would result in a deflection of the secondary electrons onto a spiralling trajectory around the nToF central axis, with the diameter and pitch controlled by the magnitude of the magnetic field applied. Meanwhile the influence of the small magnetic field on the path of the significantly heavier negative secondary ions would be negligible, resulting in a tunable separation of the secondary electrons and detection on the annular MCP electron detector.

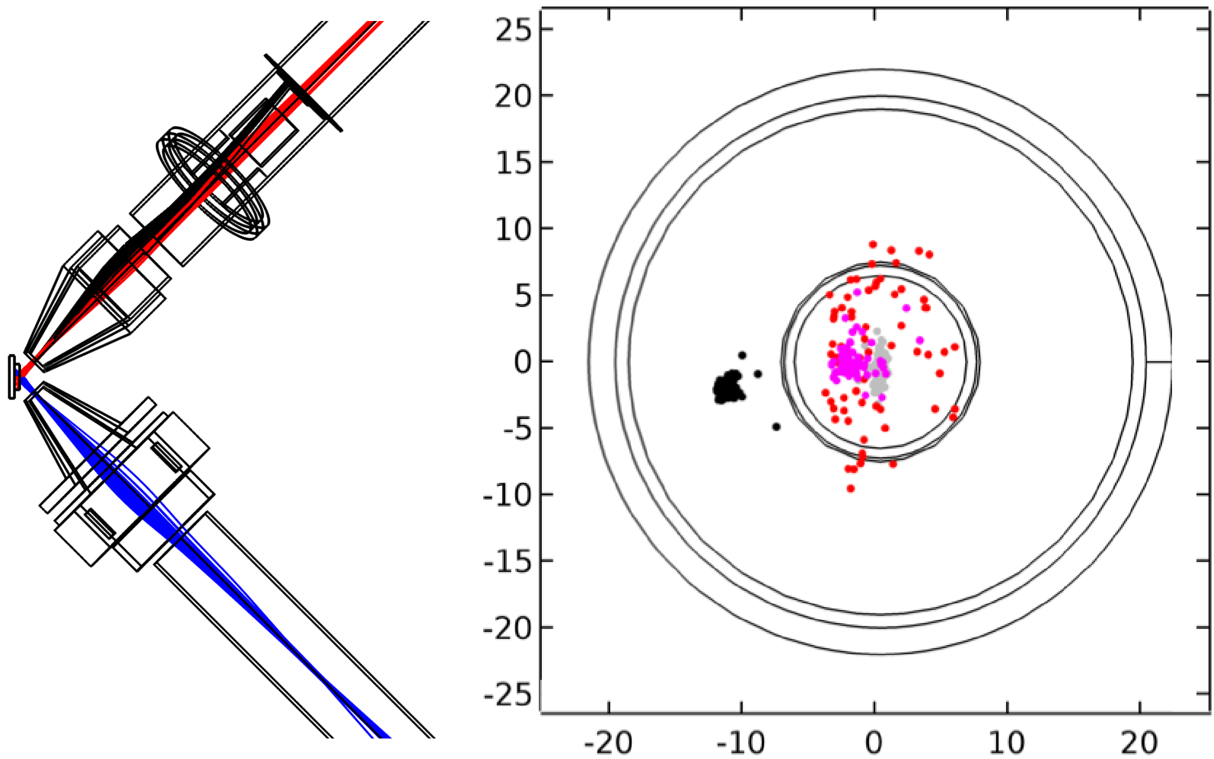

Figure 3.10.: Left: Simulated secondary electron (black), positive (blue) and negative ion (red) trajectories in the dual ToF mass spectrometers. Right: Simulated beam positions and separation within the negative ion ToF spectrometer: plotted are the positions of simulated secondary electrons in the eMCP plane (black), and of negative ions in the eMCP plane (pink) as well as in the nMCP plane located at the end of the spectrometer (red). The electron positions at the entrance of the nToF spectrometer are shown in gray.

3.4.3. Experimental extraction field, electron separation and operating parameters

Considering that fine tuning of the extraction fields was already critical to enable operation of the initial positive ion ToF mass spectrometer with electron start, it is even more so for the simultaneous extraction of electrons as well as negative and positive ions as already discussed in Chapter 3.4.2. The sample and its mount remain on ground potential and (theoretically symmetrical) high voltages are applied to both symmetrically designed and aligned ToF extraction cones to collect the low energy charged secondary particles ejected from the sample surface. However in reality, the alignment of both ToF extraction cones is at best accurate to a fraction of a millimeter and a good extraction efficiency for the secondary electrons is disproportionally important, since their detection on the eMCP detector provides the needed start signal for both polarity ToF spectra.

Therefore the final operating parameters for the dual-polarity setup used for all of the yield measurements referenced in this work (unless specifically mentioned, validation and test measurements were partly acquired with slightly different preliminary settings) as listed in Table 3.2 are not perfectly symmetrical. In fact it proved to be beneficial to bias the extraction towards positive extraction voltages and thus towards the negative polarity spectrometer.

Additionally, it was determined through simulations that the limited width of the sample and the shape of the originally used omicron-type sample mount, in which the sample is mounted slightly recessed, degrade the electric extraction field at the sample surface significantly. While this problem could be overcome in the initial pToF setup by biasing of the extraction, it is much more critical for the modified dual-polarity setup. Therefore, the sample mounting was changed and samples are now mounted from the back such that the sample surface sits flat with respect to the surrounding sample mount. Additionally a thin (30 µm) and wide (50 mm) grounded stainless steel shielding with cut-out aperture is mounted on top of the sample to shape the extraction fields towards both extraction cones. This maintains the symmetry of the electric extraction field - which is now significantly more important than in

pToF	Cone 1	-0.90 kV	Cone 2	-4.50 kV
	Steerer X1	-6.30 kV	Steerer X2	-6.00 kV
	Steerer Y1	-6.50 kV	Steerer Y2	-6.50 kV
	Liner	-4.75 kV		
	pMCP front	-6.30 kV	pMCP back	-4.50 kV
nToF	Cone 1	1.80 kV	Cone 2	4.50 kV
	Steerer X1	4.95 kV	Steerer X2	4.80 kV
	Steerer Y1	4.80 kV	Steerer Y2	4.80 kV
	Liner	4.75 kV		
	eMCP front	4.00 kV	eMCP back	5.80 kV
	pMCP front	4.00 kV	pMCP back	5.60 kV

Table 3.2.: Operating voltages of the pToF and nToF mass spectrometers

the initial single polarity extraction - when the sample is not centrally positioned with respect to the two extraction cones. The effect on the electrostatic field distribution in the region directly in front of the sample surface can be easily noticed in Figure 3.11.

Finally to tune the electron separation, the straightforward and easy to modify solution of mounting additional permanent magnets on the nToF flange of the CHIMP measurement chamber was used: While deflection of the secondary electrons just based on the earth magnetic field was already sufficient to obtain a suitable start signal and to enable basic operation of the mass spectrometer, the start event rate on the eMCP detector could be increased by roughly a factor of 2 to 3 through the additional magnetic field applied. Without the applications of magnets, a small but distinct peak at a very low flight time of roughly 25 ns in the negative ion ToF spectrum could be observed, indicating that a few secondary electrons were still passing through the annular eMCP detector hole and were detected on the nMCP stop detector. This electron-electron correlation peak is not longer present with the additional permanent magents applied.

The application of an external magnetic field by means of the optionally installable 15° tilted concentric coil promises an even better control of the secondary electron separation

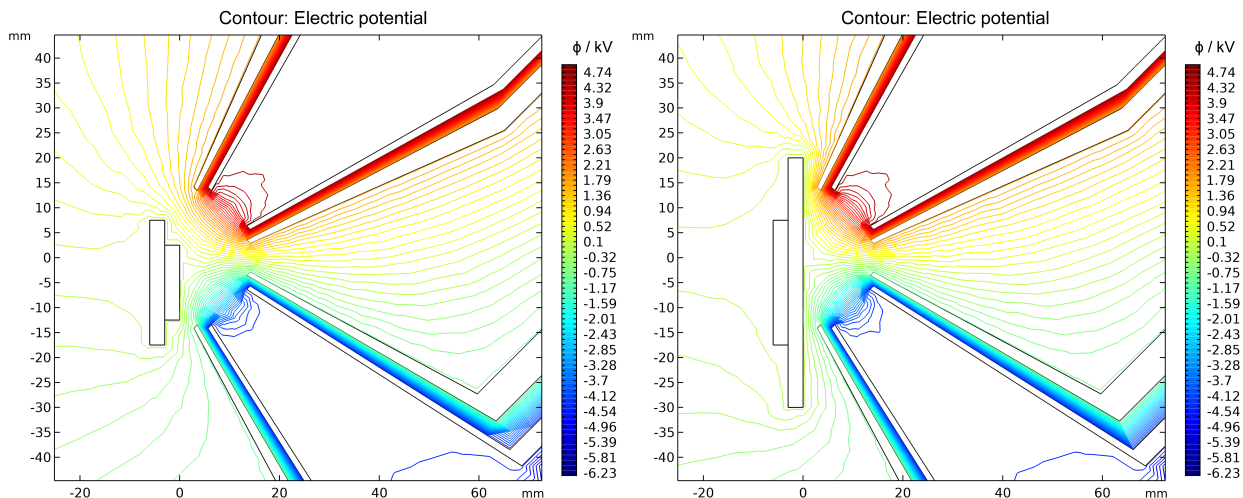

Figure 3.11.: 2D electric potential simulation (with voltages as listed in Table 3.2) of the extraction region in front of the 5 mm offset sample stage with initial narrow sample mount (left) and with modified wide sample shield that additionally forms the extraction field (right).

within the nToF spectrometer.

3.4.4. pToF and nToF performance and mass resolution

Due to the dependence and influence of the extraction field geometry on the ion flight time and therefore also mass resolution, the performance of the pToF and nToF mass spectrometers is strongly coupled. By biasing the extraction voltages towards one polarity of secondary ions, the mass resolution of the corresponding mass spectrum can be significantly enhanced, however the mass resolution of the other polarity mass spectrum will suffer accordingly. Additionally the extraction efficiencies will change, which is especially critical for the secondary electron extraction, on which both ToF spectra depend on for their start signal.

First ion flight simulations performed using the particle tracing module in Comsol Multiphysics suggested that a mass resolution on the order of the initially installed pToF instrument, so in the region of $m/\Delta m \approx 45$ would be realistic for both mass spectra. However, while tuning the instrument it was discovered that a bias of the outer extraction voltages towards the negative ion ToF is advantageous in order to achieve reasonable count rates. Additionally the sample, which is slightly recessed into its mount, disturbed the extraction field enough to impact the practically achievable mass resolution. For specific combinations

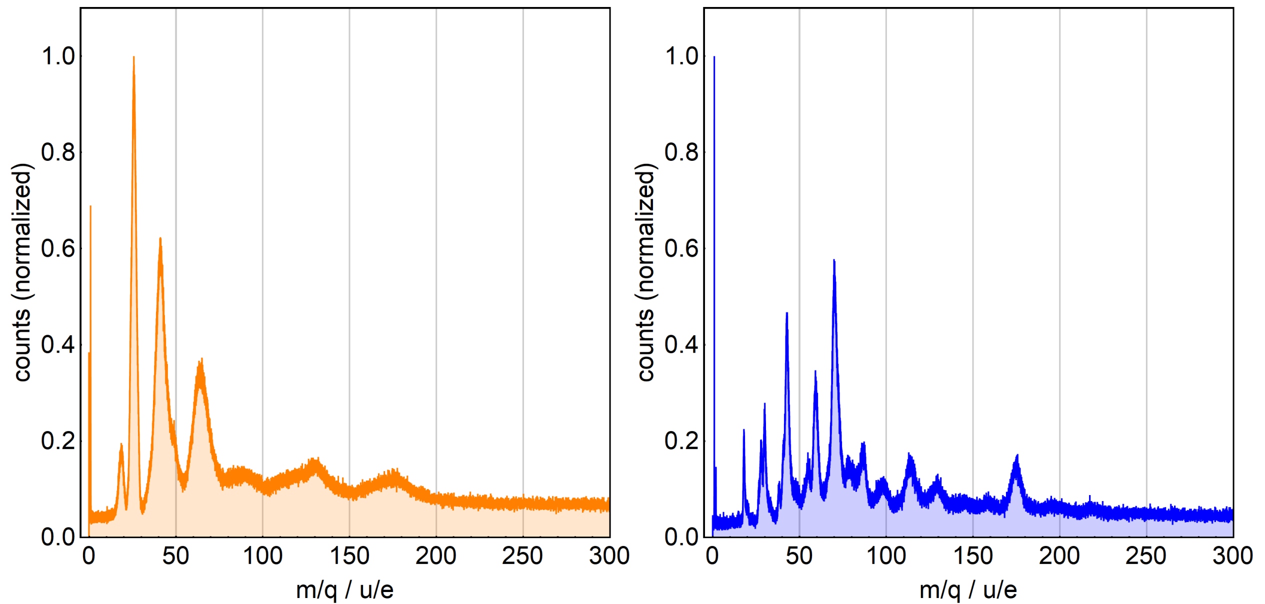

Figure 3.12.: Negative (left) and positive (right) spectra of 28 MeV ^{197}Au on Arginine. These two spectra were acquired with a slightly modified tuning of the ToF mass spectrometers when compared to the settings given in Table 3.2, resulting in lower mass resolution in the negative ion mass spectrum (left).

of extraction voltages even a distinct separation of flight paths in the extraction region could be observed, resulting in a double-peak splitting of low-mass peaks like ^{1}H or ^{16}O in the mass spectra. It could be confirmed by additional simulations that this effect can likely be explained by secondary ions that are emitted towards the oppositely biased extraction cone, which are then decelerated and deflected back in the electric field before they are extracted towards the corresponding ToF spectrometer with a time delay of roughly 800 ns to 900 ns. Therefore the fine tuning of the extraction voltages requires a lot of care and repeated checks to avoid conditions like these.

For the measurements presented in this thesis, mass spectrometer optimization was performed both on an arginine and an NaCl sample (both spin-coated on clean Si-wafers), since the spectra of both samples exhibit well separated and identifiable mass peaks. Spectra acquired from the arginine sample using a 28 MeV ^{197}Au primary ion beam are shown in Figure 3.12, exhibiting a mass resolution of roughly $m/\Delta m \approx 17$ in the pToF and $m/\Delta m \approx 13$ in the nToF spectra. These figures provide a rough estimate, since due to the rather low mass resolution and the overlapping of especially the heavier mass peaks in combination with

their non-symmetric shape the determination of their FWHM is not straightforward. For the resulting optimized parameters as given in Table 3.2, which were used for the following measurements, it is therefore reasonable to assume a mass resolution on the order of $m/\Delta m \approx 10 - 20$ for both positive and negative mass spectra. Achieved mass resolution with the current setup is however also dependent on the sample surface structure in case of not perfectly flat samples and in the outer regions of the sample influenced by the slightly protruding sample shield aperture. If special care is taken to account for these issues, mass resolution is therefore sufficient to resolve the peaks or peak groups of monomer secondary ions and small molecular secondary ions from simple compounds. To significantly improve mass resolution and mitigate the mentioned effects, the sample mounting mechanism could be revised to a new design, such that the field-shaping sample shield can be integrated in a way that alignes it perfectly flat with the surface of the sample.

4. Molecular imaging

A range of imaging tests were performed on the initial setup as described in Section 3.3. A variety of biological samples and lithografically produced inorganic structures were used as samples. The results have been published (Miltenberger et al. 2017) and the first and second part of this chapter will largely follow the presentation of the paper by first showcasing large scale imaging of a GaAs wafer structure which was also used to determine the lateral resolution of the setup. Finally in the third part, the visualization of sputter damage accumulated on a homogeneously spin-coated Arginine sample wafer is demonstrated.

4.1. Large scale imaging of a GaAs wafer

To demonstrate the ability to image large-scale samples a metallic Al/Au contact structure on GaAs was used. The sample was provided by M. Oppliger and A. Stockklauser in the Quantum Device Lab group of Prof. A. Wallraff at ETH Zurich. As the primary beam ^{127}I ions at 15 MeV were utilized in combination with a capillary of approx. 5 µm outlet diameter. The resulting primary beam current was around 1 pfA. The acquired image is shown in Figure 4.1, with the intensity of peaks in the mass regions between $40 - 47u/e$, $70 - 75u/e$ and 143/152 u/e selected. These mass regions were pragmatically chosen by inspecting spectra originating both from the metallic Al/Au contact pads and from regions in between the pads. Therefore the atomic or molecular peaks associated with these mass regions have not been exactly identified - prominent candidates would be the PDMS (polydimethylsiloxane) monomer (74 u/e) and dimer (148 u/e) as well as Ga, As and GaAs. PDMS is nearly ubiquitous in all kinds of plastic labware and can be found on most samples if no special effort is taken to avoid contamination throughout the whole sample preparation process (Keller et al. 2008). Since MeV-SIMS probes only the top few molecular layers of the sample surface, it is specifically susceptible to observe such surface contaminations.

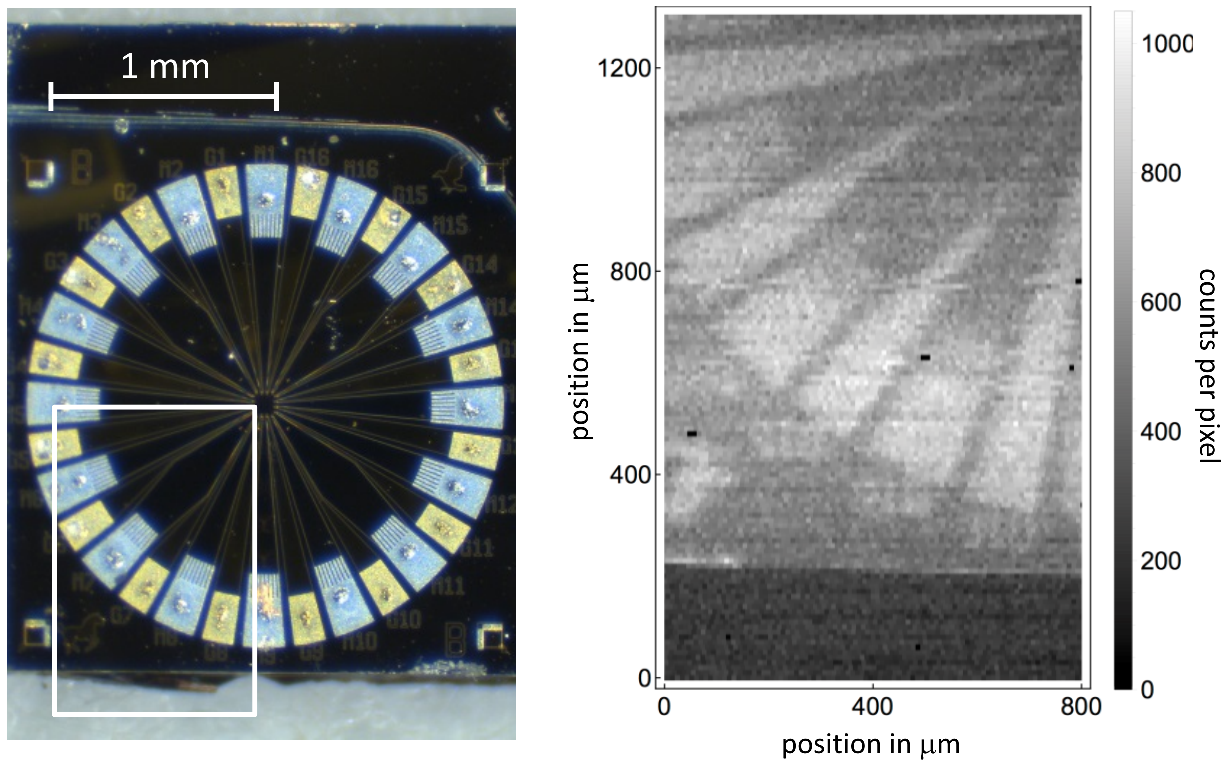

Figure 4.1.: Al/Au metallic contact structure on GaAs. Left: optical micrograph. Right: MeV-SIMS raster image of the marked rectangular region taken with a 15 MeV iodine ion beam and a capillary of 5 µm outlet diameter. The intensity of three secondary mass peak groups is imaged. (Miltenberger et al. 2017).

During the measurement the sample was continuously scanned form left to right along horizontal lines with a velocity of about $10\,\mu\text{m}\,\text{s}^{-1}$. According to the expected lateral resolution the vertical distance between lines was chosen at $10\,\mu\text{m}$. The acquired data was then re-binned into time intervals of 1s duration, which corresponds to a lateral movement in horizontal direction of also $10\,\mu\text{m}$ to obtain square pixels of approx. $10\,\mu\text{m} \times 10\,\mu\text{m}$. This procedure is also reflected in the imaging errors that can be identified in the image upon closer inspection: There are a few horizontal lines that seem to be offset with respect to their neighbouring lines (e.g. at a vertical position of $750\,\mu\text{m}$) which is caused by non-uniform movement of the positioner resp. variations of its velocity. This behaviour could be largely mitigated later on by additionally recording the position continuously and a corresponding calibration of the positioner velocity. The black pixels with missing data were caused by beam instabilities of the Tandem accelerator resulting in a temporary loss of primary beam current on the sample. The coincidence rate in the ToF spectrometer was in the range between 3 kHz to 4 kHz depending on the local surface composition, resulting in individual pixel mass spectra with between $3 \cdot 10^3$ and $4 \cdot 10^4$ entries. The total measurement time for an image of $1.4 \cdot 10^4$ pixels was $1.5 \cdot 10^4\,\text{s}$ which is slightly over 4 h. The image shown in Fig. 4.1 was cropped down to $1.0 \cdot 10^4$ pixels. The measurement time overhead for repositioning of the sample during raster scanning therefore was about $1.5 \cdot 10^3\,\text{s}$ or approximately 10 % of the total measurement time. This could be further reduced by optimization of the scanning algorithm, for example by scanning in a horizontal meandering pattern. In comparison to conventional focusing and raster scanning of the primary beam this does therefore not present a significant drawback. However using sample raster scanning results in a sequential data acquisition for each pixel and in the current implementation only one single frame is taken during the whole measurement. This represents a disadvantage compared to fast beam scanning, which can be set up to acquire many frames with lower statistics that are then summed up to create the final image and therefore allow for a 'preview' of the total field of view. A similar effect could be achieved by implementing a different scanning pattern like scanning only every other line in the first mapping across the imaged area and then filling

in the missing lines in a second mapping. Such an interlaced scanning procedure would not significantly increase the total overhead time spent for positioning.

4.2. Line scan lateral resolution measurements

To determine the achievable lateral resolution one has to inspect the acquired image more closely: The sharpest identifiable features in Figure 4.1 (right) are between 1 and 2 pixels wide, which suggests an apparent lateral resolution on the order of 10 μm to 20 μm.

This was more thoroughly quantified by performing a separate line scan in vertical direciton across the edge of the GaAs chip in discrete steps of 1 μm. For each pixel a spectrum was acquired for 5 s with a primary ion rate of approx. 2 kHz. The intensities for each pixel position are plotted in Figure 4.2 and one clearly observes a significant change in normalized intensity by about 30 % when moving across the GaAs wafer edge at approx. 85 μm. The resulting intensity change was fitted with an error function (assuming a step-function due to the edge of the wafer convoluted with a gaussian beam profile). From this the lateral resolution - and thus also the approximate width of the primary ion beam when hitting the sample - was estimated to be (9.8 ± 2.3) μm (FWHM).

Thus the observed lateral resolution at 50 mm distance from the capillary tip is only slightly bigger (by a factor of approximately 2) than the capillary outlet diameter of 5 μm. This is in agreement with expectations and confirms that the angular divergence of the collimated beam is very small (see estimate in Section 3.2). When employing smaller capillary diameters and decreasing working distance, a resolution around 1 μm (FWHM) should be within reach. However the distance of the capillary tip from the sample surface has to be balanced in any system employing a sophisticated secondary particle extraction: Although the sharp capillary tip can be shielded by a grounded metal shielding tube, the delicate electric extraction field might still be disturbed otherwise.

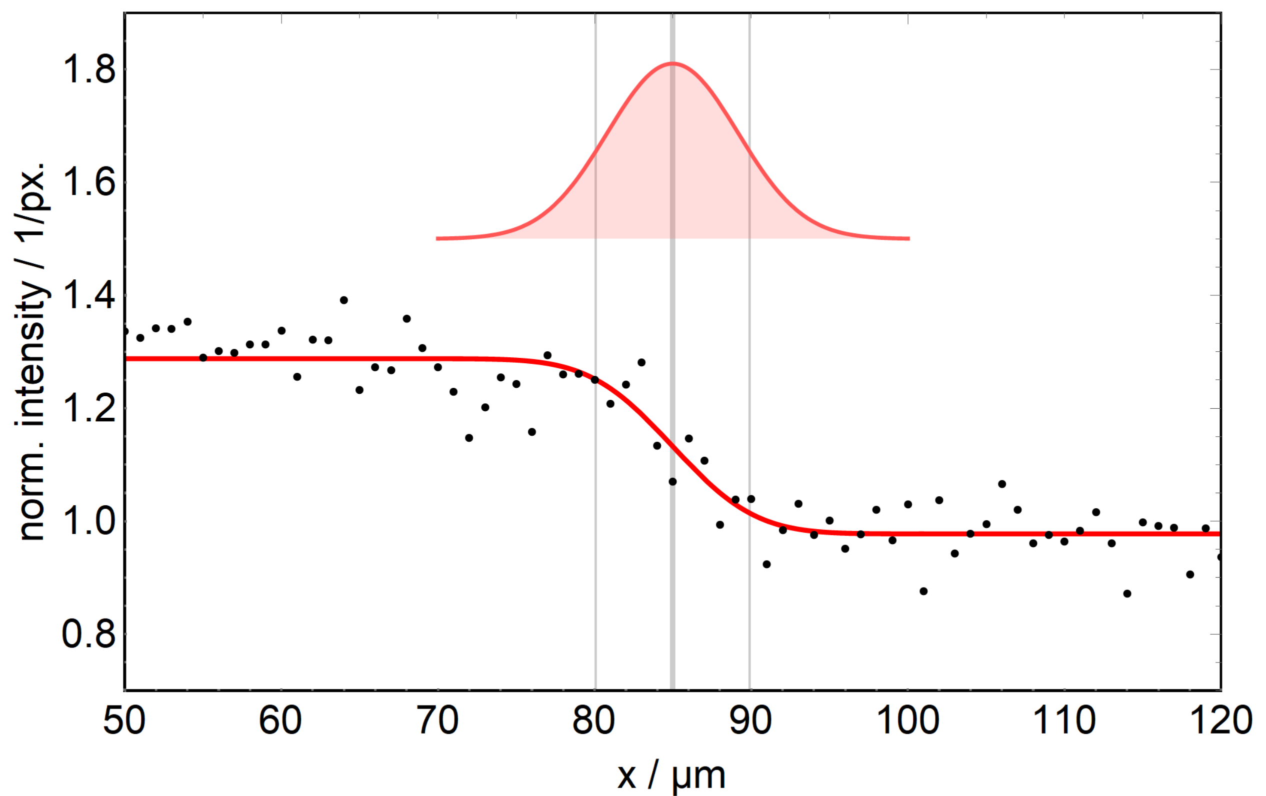

Figure 4.2.: MeV-SIMS line scan across the edge of the GaAs chip shown in Figure 4.1. The error function fitted to the intensity profile has a width of (9.8 ± 2.3) µm (FWHM). The capillary outlet diameter was 5 µm and a 15 MeV iodine primary beam was used. (Miltenberger et al. 2017).

4.3. Sputter damage visualization on a homogenous sample

Finally, the last measurement showcases the molecular imaging capabilites of MeV-SIMS and evaluates the reproducibility of our positioning setup (the sample is manually moved in and out of the beam with a linear stage). In general the very low primary ion currents used in our capillary microprobe setup do not inflict measurable damage during the time intervals of a single measurement (see Chapter 5.1). However we investigated sample damage on a single spot of one of the Arginine samples that was used over the course of several months repeatedly for beam setup and testing with a range of different ion beams. This was done both by point measurements on the spot itself and by imaging of the area around the damaged sample spot.

In Figure 4.3 the corresponding spectra and image are shown: On the left, three of the spectra acquired on the same spot with a 7 MeV Cu primary ion beam over the course of a time period of approximately three months are shown. All spectra are normalized to the intensity of the molecular Arginine $[M+H]^+$ ion at mass $m/q = 175u/e$. Accordingly, a slow change in relative peak intensities can be observed with especially the fragment peaks at masses $m/q = 43u/e$ and $m/q = 70u/e$ showing significant enhancement in the third spectrum. Below, a fourth spectrum shows a comparison spectrum acquired on the same day as the third spectrum, but on a different, previously unirradiated spot of the same sample which closely reproduces the initial spectrum. On the right hand side, Figure 4.3 shows the MeV-SIMS image acquired around the damaged measurement spot with 7 MeV Cu primary ions. For each pixel the intensity of the mentioned Arginine fragment peaks ($m/q = 43u/e$ and $m/q = 70u/e$) normalized to the intensity of the full molecular mass peak at $m/q = 175u/e$ was plotted. The 15 x 15 pixel image was recorded by acquiring discrete spectra over 10 s at points with a distance of 100 µm to each other. The resulting 100 µm × 100 µm pixels are representative since for all measurements a capillary with an outlet diameter of 250 µm was used, so the pixel size is still lower than the expected lateral resolution.

The resulting image shows a very clearly defined damage spot with significantly increased fragment peak intensities that show a very high contrast to the remaining image. This con-

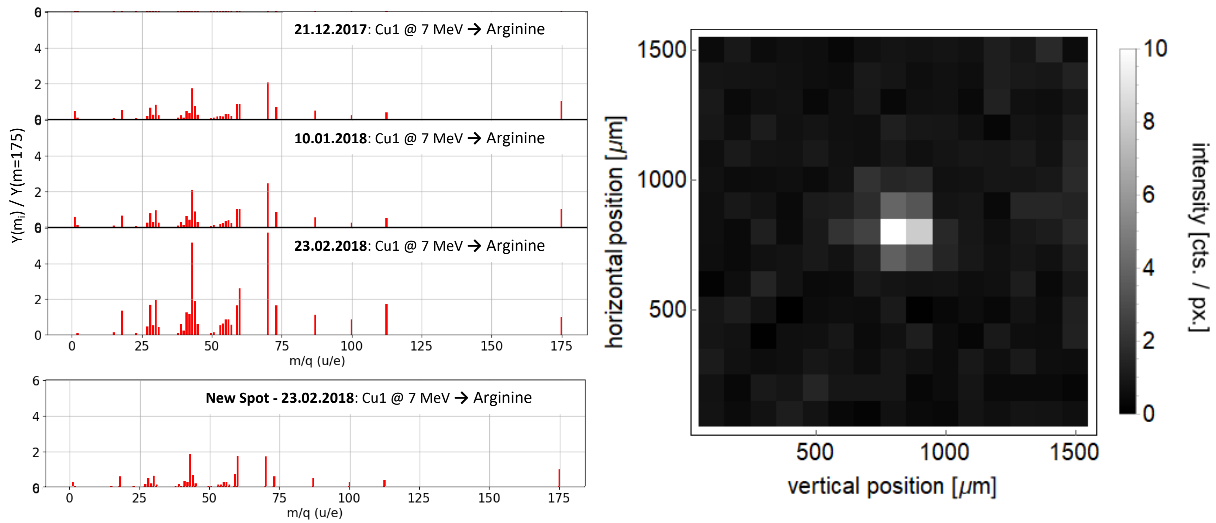

Figure 4.3.: Damage inflicted on Arginine sample over the course of several months by repeated tests and tuning measurements: MeV-SIMS spectra acquired over time (left) and MeV-SIMS image of Arginine fragment peak intensity around the damaged spot (right).

firms the reproducibility of our sample positioning - also between measurements and while changing samples multiple times in between - to a precision of at least 100 μm and demonstrates the remarkable power of molecular imaging with the CHIMP capillary microprobe setup. Furthermore the measurements display that even though the damage inflicted to the sample during a single measurement is negligible with primary particle currents in the pfA range, over time this damage accumulates and is certainly measureable after performing dozens of measurements on a single spot.

5. Secondary ion yield and fragmentation

To study the behaviour of secondary ion yields and fragmentation over a wide range of primary ion parameters, an extensive series of MeV-SIMS measurements were performed using the initial CHIMP setup described in Section 3.3. Most of the point-spectra (i.e. non-imaging) measurements for qualitative and quantitative comparison were acquired on a range of three samples that were supplied within the IAEA CRP (Coordinated Research Project) F11019 on the 'Development of Molecular Concentration Mapping Techniques using MeV Focused Ion Beams' running from 2014 to 2019. The corresponding substances arginine, leu-enkephalin and polyethylene glycol (PEG) were chosen as representative materials of specific interest to the potential field of application in the biological and molecular sciences. Therefore, and because of their distinctly different molecular structures and fragmentation patterns, they were also good candidates for the extended parameter studies presented here. Moreover the samples would be measured by laboratories participating in the CRP, so the corresponding spectra are widely familiar and can be used as points of comparison.

Therefore, in the first Section 5.1, the yield measurements done at ETH Zurich within the framework of the IAEA CRP will be described to introduce the different sample materials and their spectra, before the details of the methodology and ion species used are described in Section 5.2. Afterwards the remaining sections are each examining and discussing the measurement results in terms of a specific quantity: first absolute yields (Section 5.3), then relative peak yields and the observed fragmentation (Section 5.4), the influence of cluster ions and specifically their cluster size (Section 5.5).

5.1. Samples and yield measurements within the framework of the IAEA CRP

For the second round of the CRP MeV-SIMS round-robin test measurements three different organic sample materials were prepared by spin-coating by the group of Prof. Jiro Matsuo at Kyoto University (Japan). In Figure 5.1 the positive secondary ion mass spectra of all three samples recorded with a 7 MeV $^{197}Au^{1+}$ primary ion beam in spring of 2018 are reproduced.

- Arginine, $C_6H_{14}N_4O_2$, m=174 u, an α-amino acid takes over important functions in cell division, immune functions and hormone release. It is a non-volatile and a highly polar molecule often used for benchmarking and evaluating new mass spectrometric techniques. Secondary ion mass spectra have been acquired and analyzed with fission-fragment ionization mass spectrometry (Chait, Agosta, and Field 1981) already in the 1980s. All the main feature peaks listed in Table 5.1 were observed and relative intensities were calculated for the full-mass molecular peak $(M + H)^+$ at mass 175 u (the fractionation peak of ^{13}C at mass 175 u was included) as well as for the most significant fragment peaks at masses 30 u ($CH_2{=}NH_2^+$), 43 u ($CH_3N_2^+$) and 70 u ($C_4H_8N^+$). The relative intensities were calculated by normalizing the counts integrated in each mass peak to the total number of secondary ions in the spectrum (after the background correction was applied) and should thus be comparable to the 'percent of total ionization' values given by (Chait, Agosta, and Field 1981) and also listed in the table for comparison.

- Leu-enkephalin, $C_{28}H_{37}N_5O_7$, m=555.6 u, is a peptide neurotransmitter naturally occurring in many mammals, including humans. Here keV-SIMS spectra recorded by (Westmore, Ens, and Standing 1982) are used for comparison. Again the main feature peaks of the spectrum are listed in Table 5.2. The secondary ions are identified by means of their fragmentation categorization as given in Figure 5.2. Unfortunately, no relative intensities are available for the comparison spectra, so only the relative intensities as determined from the MeV-SIMS measurement are listed for the full-mass

molecular peak $(M + H)^+$ at mass 556.6 u as well as for the major fragment peaks at masses 30 u (a_2), 120 u (a_3), 136 u (a_1) and 278 u to 279 u (b_2 and d_2).

- Polyethylene glycol, $H[C_2H_4O]_n OH$, m=18 u+n×44 u, is a polyether compound often used in pharmaceutical products and biotechnological processes. As sample material a mixture of different polymer lengths with sodium trifluoroacetate (NaTFA) was used (PEG1000:PEG2000:PEG3000 = 1:1:2) : NaTFA = 1 : 1. For this specific mixture no other comparable literature spectra were available besides the reference SIMS spectra provided together with the samples. The ion identification is far from unambiguous, especially since we can only resolve the lower-mass region up to a few 100 u with our mass spectrometer and even there the available mass resolution is very limited. The given ion identifications were assigned in comparison with other fragmentation spectra (Hittle et al. 1994) of different polyglycols and under the consideration of the mixture with sodium trifluoroacetate. Relative peak intensities are listed for all the tabulated fragment peaks, including the atomic Na^+ ion peak at mass 23 amu, which contributes over one quarter of the counts to the spectrum.

For the round-robin yield comparison measurements done within the scope of the CRP in spring of 2017, the positive secondary ion mass spectrum of each sample was measured by scanning a 28 MeV $^{197}Au^{7+}$ beam over a homogeneous 200 μm × 200 μm fresh sample area with a total fluence of $1 \cdot 10^{10}\,\mathrm{p\,cm^{-2}}$. The sample area used was chosen with a distance of at least 1.5 mm from the outer edge of the sample silicon wafer and between subsequent analysis areas on the same sample a minimal spacing of at least 500 μm was employed. At the same time the incident primary ion fluence was determined by repeated measurements of the primary ion count rate with the GID transmission detector. The primary ion beam was attenuated to an initial count rate of 1 kHz, resulting in a measurement time of $4 \cdot 10^3$ s to reach the required total particle fluence. The 200 μm × 200 μm sample area was scanned once every 100 s, resulting in a total of 40 sequential frames.

The resulting average secondary ion yields for select characteristic molecular and fragment ion peaks are summarized in Table 5.4: Yields of prominent mass peaks are generally on

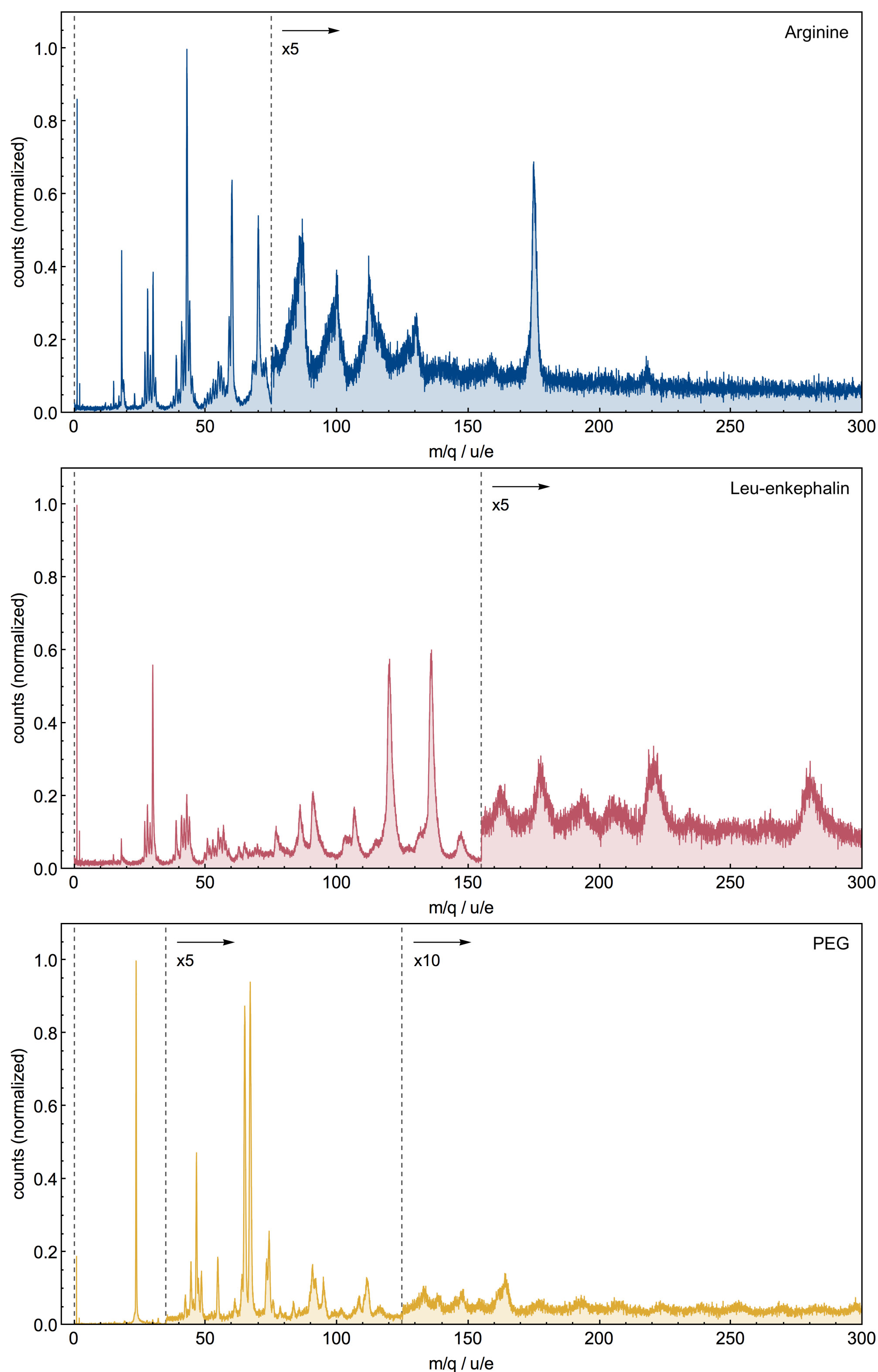

Figure 5.1.: MeV-SIMS positive ion spectra of CRP samples acquired with a 7 MeV $^{197}Au^{1+}$ primary ion beam. From top to bottom: Arginine, leu-enkephalin and polyethylene glycol (PEG).

Table 5.1.: Positive-ion spectrum of arginine, $C_6H_{14}N_4O_2$, m=174 u

m/z	ion	rel. intensity (Chait, Agosta, and Field 1981)	rel. intensity
18	${NH_4}^+$	7.5	
27		2.9	
28	$HCNH^+$	9.8	
30	$CH_2{=}{NH_2}^+$	8.1	3.22
41	$C_2H_3N^+$	3.1	
42	${CH_2N_2}^+$	2.8	
43	${CH_3N_2}^+$	14.3	9.71
44	${CH_4N_2}^+$	4.9	
59	${CH_5N_3}^+$	3.4	
60	${CH_6N_3}^+$	4.9	
70	$C_4H_8N^+$	11.6	7.57
87		1.6	
100	${C_4H_{10}N_3}^+$	0.6	
112		0.7	
129		0.2	
130	${C_5H_{14}N_4}^+$	0.7	
131		0.3	
175	$(M+1)^+$	3.7	2.89
176	$^{13}C(M+1)^+$	0.6	
197	$(M+Na)^+$	0.2	

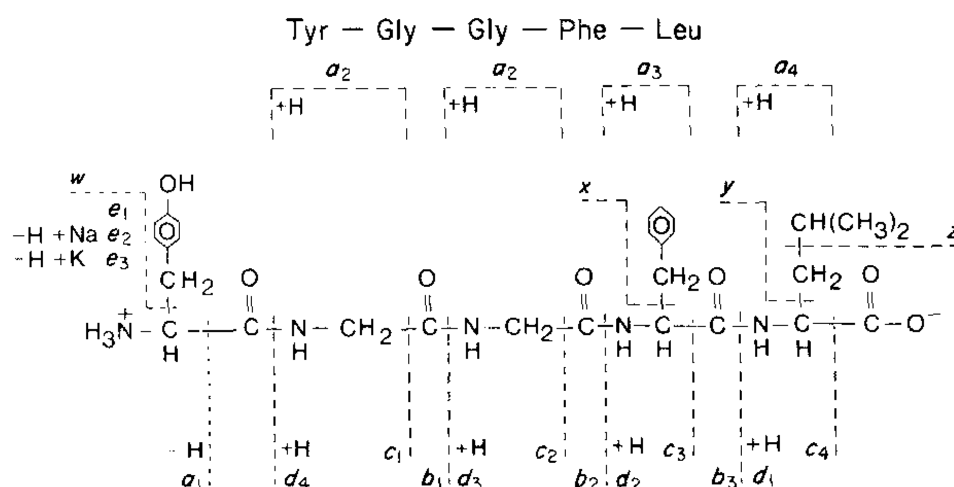

Figure 5.2.: Structure and positive ion fragmentation pattern of leu-enkephalin (Westmore, Ens, and Standing 1982).

Table 5.2.: Positive-ion spectrum of leu-enkephalin, $C_{28}H_{37}N_5O_7$, m=555.6 u

m/z	ion	rel. intensity
30	a_2	5.21
43	z	
57	y	
86	a_4	
91	x	
120	a_3	14.32
136	a_1	13.96
221	b_1	
278	b_2	1.53
279	d_2	
397	c_3	
556.6	$(M + H)^+$	0.06

Table 5.3.: Positive-ion spectrum of mixed PEG, $H\,[C_2H_4O]_n\,OH$, m=18 u+n×44 u

m/z	ion	rel. intensity
23	Na^+	28.31
45	$C_2H_4OH^+$	2.73
62	$HOC_2H_4OH^+$	7.45
64	$FC_2H_4OH^+$	8.60
107		2.05
158	$C_4H_5F_3O_3{}^+$	1.54

Table 5.4.: Average SI yields of different characteristic molecule and fragment peaks determined during CRP measurements.

sample	fluence	ion mass	yield
Arginine	$(1.02 \pm 0.03) \cdot 10^{10}$ ions cm^{-2}	175 u	0.015 ± 0.002
Leu-enkephalin	$(1.07 \pm 0.03) \cdot 10^{10}$ ions cm^{-2}	136 u	0.065 ± 0.003
PEG	$(1.00 \pm 0.03) \cdot 10^{10}$ ions cm^{-2}	64 u	0.038 ± 0.005

the order of percent, indicating the high efficiency of the MeV-SIMS desorption process. To observe the evolution of the secondary ion yields throughout the sputtering process, the spectra acquired in list-mode were separated into spectra representing individual passes over the scanned sample area which were individually analysed. The expectation would be that over time the incident primary ions induce damage to the sample material, resulting in slowly decreasing yields of the full mass molecule peaks and increasing yields of the fragment peaks. The resulting development of the observed secondary ion yields with increasing total primary ion fluence is plotted in Figure 5.3: For both the full-mass molecular arginine peak (m = 175 u) and the PEG fragment peak at mass m = 64 u), the yield stays constant within the uncertainties of the individual measurement points. For the leu-enkephalin fragment peak at mass m = 136 u however, the yield increases initially after starting the measurement, before it also levels off at a certain value (although with higher fluctuations). This possibly indicates a charge-up effect of the leu-enkephalin sample under the bombardment with positive primary ions, which leads to an increased emission of positive secondary ions. In summary it can be concluded that the relatively low fluences reached in the SIMS measurement are still well below the limit of static SIMS and not yet inducing measurable damage to the sample material. This bodes well for the sensitivity and damage characteristics of MeV-SIMS as a minimally destructive measurement technique, since the measurement times of $4 \cdot 10^3$ s reached here are significantly higher than usually necessary to acquire a secondary ion mass spectrum with decent statistics.

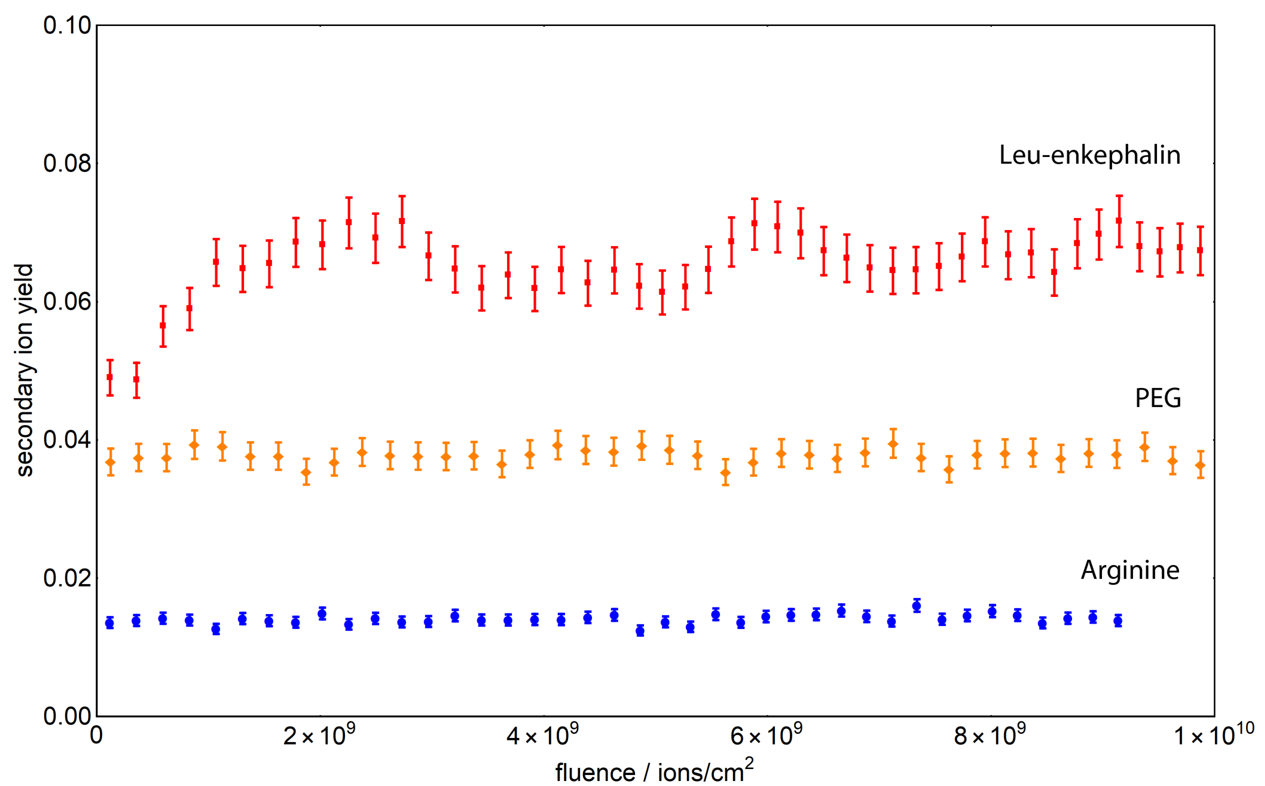

Figure 5.3.: Secondary ion yield of characteristic molecule and fragment peaks as listed in Table 5.4 as a function of total primary ion fluence.

5.2. Methodology and primary ion species

5.2.1. Exploring stopping power regimes using a range of atomic and cluster primary ion beams

To explore the mechanism of secondary ion desorption and ionization occurring in MeV-SIMS over a wide range of different primary ion beam regimes, systematic measurements were performed on arginine, leu-enkephalin and PEG. Monoatomic ion beams of ^{12}C, ^{63}Cu, ^{127}I and ^{197}Au as well as cluster ion beams of C_2, ..., C_5, C_{60} and Cu_2, ..., Cu_9 with energies ranging from 2 MeV to 70 MeV were used as primary ion species. These different ions span atomic numbers from Z = 6 to 79 and therefore exhibit different stopping power characteristics in the sample material: The specific nuclear and electronic stopping power of the monoatomic ion species used (as computed by SRIM (Ziegler, Biersack, and Littmark 1985)) over the energy range from 0 MeV to 100 MeV is plotted for arginine in Figure 5.4.

While for heavy ions like ^{197}Au and ^{127}I the electronic stopping power increases monotonically with increasing energy throughout the covered range, the electronic stopping power of ^{63}Cu ions approaches a maximum at an energy of around 60 MeV, which is then largely maintained. Conversely the electronic stopping power of ^{12}C already reaches its maximum at energies around 5 MeV and continuously falls from there on. For all ions, the nuclear stopping power in the sample material of arginine exhibits its maximum already at energies well below 2 MeV, such that it continuously drops with primary ion energy in the energy range in which measurements were performed.

Accordingly, the different energy loss specifics of the selected ion species allow to cover a wide range of possible stopping power regimes. This is shown in Figure 5.5, which plots the nuclear stopping power of the ions used against their electronic stopping power (in arginine). Each curve represents the specific stopping power ratio of the respective monoatomic ion at the sample surface, which varies with primary ion energy. Additionally data points represent the positions on these curves where measurements were taken. Finally, the data points for

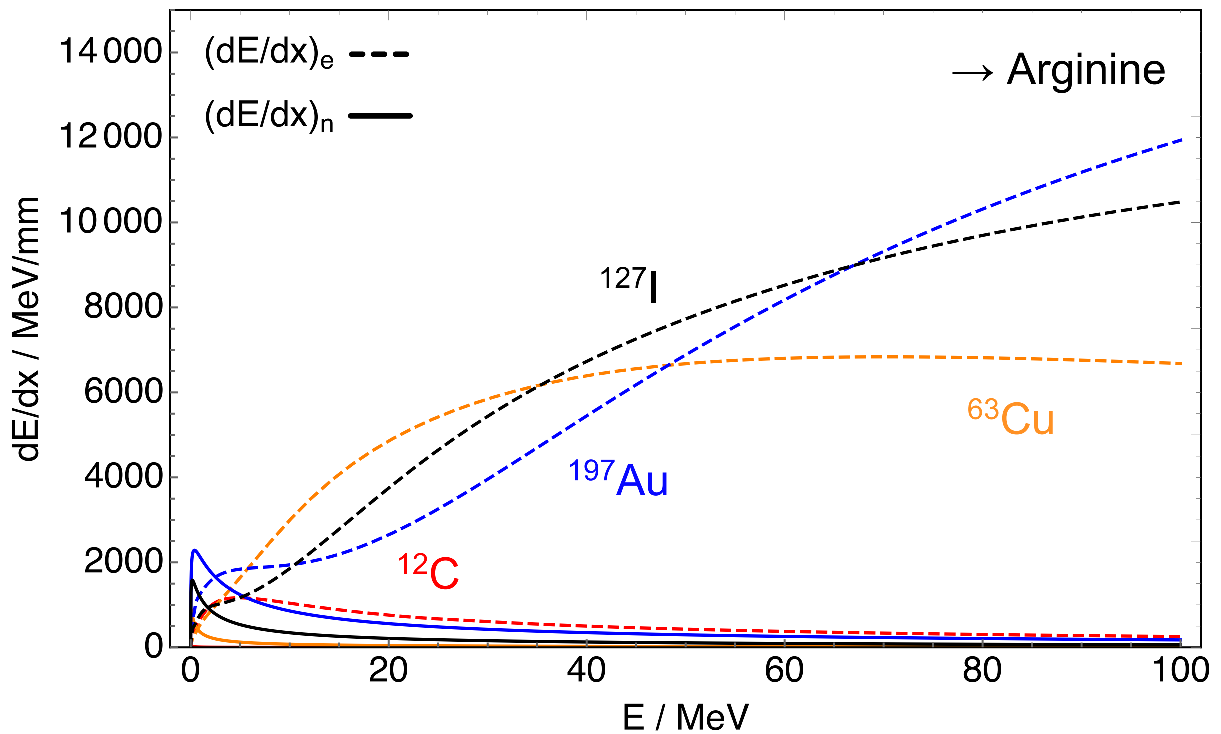

Figure 5.4.: Nuclear $(dE/dx)_n$ and electronic $(dE/dx)_e$ stopping power of monoatomic ions in arginine as computed by SRIM (Ziegler, Biersack, and Littmark 1985).

measurements which are not lying on one of the monoatomic curves represent measurements that were performed with the respective cluster ions Cu_n and C_n with n constituents. To obtain stopping power values for these cluster ions, a linear scaling was assumed by assigning the cluster ion of size n the same combined stopping power as n individual constituent ions each carrying a fractional energy of $1/n$ times the cluster ion energy i.e. excluding any collective effects in the energy loss process:

$$\left(\frac{dE}{dx}\right)_{el} C_n\,[X\text{MeV}] = n \cdot \left(\frac{dE}{dx}\right)_{el} C_1 \left[\frac{X}{n}\text{MeV}\right] \tag{5.1}$$

$$\left(\frac{dE}{dx}\right)_{nuc} C_n\,[X\text{MeV}] = n \cdot \left(\frac{dE}{dx}\right)_{nuc} C_1 \left[\frac{X}{n}\text{MeV}\right] \tag{5.2}$$

For measurements Cu_n cluster ions ranging from $^{127}Cu_2$ up to $^{567}Cu_9$ and C_n cluster ions ranging from $^{24}C_2$ up to $^{720}C_{60}$ have been used, all at a fixed energy of 7 MeV. As can clearly be seen in Figure 5.5, the use of these cluster ions significantly expands the range

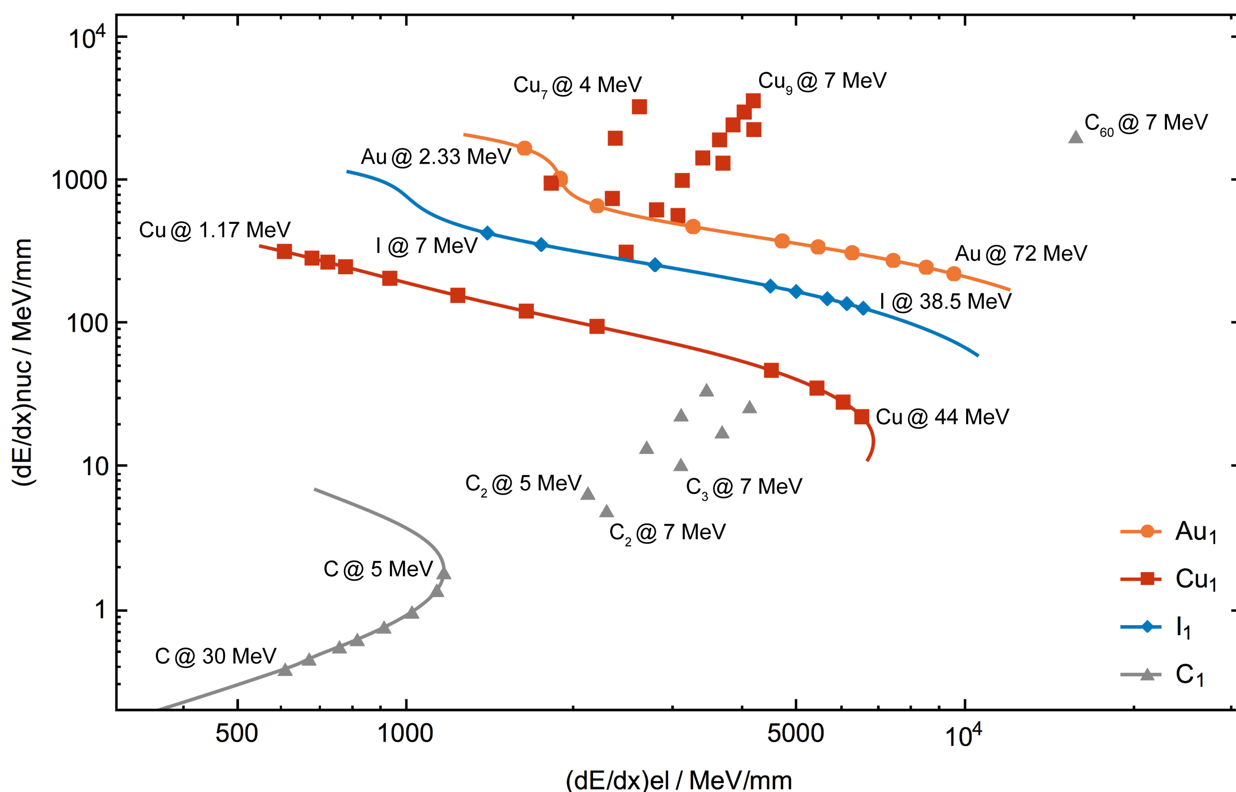

Figure 5.5.: Stopping power regime covered by positive secondary ion yield measurements in arginine performed at the CHIMP setup. The lines represent the specific stopping power ratio of the respective monoatomic ion, with the points indicating the positions where measurements were performed. The points representing measurements with cluster primary ion beams plot outside of the monoatomic curves and are positioned further to the upper right of the plot with increasing cluster size *n*.

of the explored stopping power regime by moving towards increasing nuclear and electronic stopping powers with increasing cluster size. One specific purpose of this study was therefore also to examine whether the assumed linear scaling with cluster size is mirrored in the actual secondary ion desorption and ionization yields or if collective effects are observed.

5.2.2. Performing the measurements

MeV-SIMS measurements were performed with most of the ion species and energies as shown in Figure 5.5 on all three of the samples: Arginine, leu-enkephalin and PEG. All measurements were performed as point-measurements, i.e. with the samples positioned at a fixed specific position. This position was changed regularly after a few measurements to avoid damage to

a specific spot on the surface that could induce changes to the secondary ion mass spectra (see discussion in Chapter 5.1). Measurements with a single primary ion beam were usually repeated at least twice on different days and with different sample positions to be able to verify their validity and assess the uncertainties introduced by changes in the tuning of the ion beam and possible in-homogeneities of the sample.

In total more than 600 individual measurements were done on all three samples combined, requiring a significant amount of beam time distributed over the time period from November 2017 to July 2019. During the whole measurement period, repeatedly test spectra were taken (usually at the beginning of a measurement day) to compare with previous results and ensure the validity and reproducibility of the results.

Unfortunately the small diameter ($d_{outlet} = 7\,\mu m$) imaging capillary, which was also used for some of the initial measurements with ^{129}I clogged up and stopped working at the end of November 2017. A new capillary with much larger outlet diameter of $d_{outlet} = 250\,\mu m$ was installed in view of the planned experiments with cluster ion beams which have much lower intensity and are more difficult to tune and focus. The significantly larger spot size on the sample resulted however in significantly lower secondary ion yields. This is due to the very delicate extraction geometry with electric fields extracting positive ions to one and negative electrons to the opposite side: If the spot size of the beam on the sample becomes significantly larger than the small region on the sample where an efficient extraction of both ions and electrons is feasible, one loses the secondary electrons or secondary ions ejected by impacts outside of this extraction zone. The resulting loss in secondary ion detection efficiency combined with the still accurate detection of the primary ion count rate results in reduced apparent secondary ion yields (approximately by a factor of 10). This effect can not be corrected for without detailed knowledge and analysis of the electric fields generating the extraction zone, the primary ion beam profile and the emission characteristics (energy and direction) of the secondary ions and electrons. Therefore the first mass spectra acquired using ^{127}I ions and the smaller outlet imaging capillary cannot be quantitatively compared to the later acquired spectra and are not used in the further yield analysis.

Each individual measurement was performed according to the same measurement protocol: The primary ion beam was tuned with the sample moved out of the beam path into the GID detector mounted in transmission geometry in the CHIMP chamber. The beam was then attenuated to achieve a primary ion count rate usually ranging between 1 kHz to 20 kHz in the GID detector, which was measured immediately before performing the MeV-SIMS measurement. Then the beam valve in front of the measurement chamber was closed and the sample moved into the beam path and positioned at the chosen sample position. Subsequently the beam valve was opened again and the secondary ion spectrum was acquired until sufficient statistics were achieved or the measurement duration exceeded reasonable time spans in case of low primary ion currents or low secondary ion yields. After finishing the spectra acquisition, the beam valve was closed again, the sample moved out of the beam and the primary ion count rate measured again using the GID detector to adjust for any beam drift or change of the beam current due to changing output of the ion source. Both GID measurements were then averaged and multiplied with the data acquisition time of the ToF mass spectrum to obtain the total number of primary ions incident on the sample (see Appendix C.1 for a discussion of this interpolation). The count rates and general quality of the acquired mass spectra (mass resolution, background) was checked online using the real-time updated spectra preview implemented within the LabView DAQ software. However the final analysis of all data like correlating events and calibration of the mass spectra was redone offline using the raw list-mode acquired event datasets for the different detector channels.

5.2.3. Data analysis: Mass spectra calibration and yield determination

The analysis procedure needed to extract useful yield data from the recorded events requires a process of several individual steps:

- In a first step, the events of different detector channels were correlated in the same way as described in Chapter 3.3.2 using identical Mathematica or Python timetagging scripts and the calculated events were histogrammed according to their respective ToF resulting in a flight-time spectrum.

- As a second step, these ToF spectra were mass calibrated. For each sample material a number of very distinct peaks was identified using literature spectra as well as reference spectra of identical samples measured at the labs of Kyoto University (Japan) and Ruđer Bošković Institute, (Zagreb, Croatia). The peak positions were then fitted with gaussian functions using an automated Mathematica script to determine a mass calibration function for each individual ToF spectrum. This calibration function was then applied to the respective ToF spectrum to obtain a mass spectrum.

- Finally, from the mass spectrum and the total number of primary ions incident on the sample the different yields (number of secondary ions per incident primary ion) were determined: For the total secondary ion yield, the counts over the whole mass spectrum were integrated, while for the mass-peak specific yields, select sample-dependent mass peaks (as listed in Chapter 5.1) were fitted using an exponentially modified gaussian peak function with added background offset. The number of secondary ion counts per mass peak were then calculated by integrating over the fit function with the background subtracted.

The individual steps are described in more detail within Appendix C.2, where also example calibration and peak-fit plots are provided.

5.3. Total secondary ion yield

To characterize the overall desorption and ionization process in MeV-SIMS with positive secondary ions, the total positive ion yields were determined for a range of different primary monoatomic ion beams with varying stopping regimes. At first the data will be analysed with respect to the total ion yield scaling with the primary ion velocity in Chapter 5.3.1. Subsequently the scaling with electronic stopping power of the primary ions is determined in Chapter 5.3.2.

5.3.1. Scaling with primary ion velocity

The experimental data are plotted in Figure 5.6 as a function of primary ion velocity for all three sample materials used. This dependency is of interest since the primary ion velocity directly determines the maximum velocity of the δ-electrons generated in the sample material ($v_{\delta,max} \approx 2 \cdot v_{PI}$), while their number depends on the effective nuclear charge Z_{eff} of the projectile. For comparison, in Figure 5.7 the electronic and nuclear stopping power of the respective monoatomic ion in the sample material are plotted over the same velocity range.

When looking at the compiled data, there appears to be a threshold velocity around $0.25\,\mathrm{cm\,ns^{-1}}$, above which secondary ion yields increase drastically with increasing electronic stopping. This is in line with previously reported findings (Håkansson, Jayasinghe, et al. 1981; Jones 2012). The yield curves for the different primary ions exhibit a similar velocity threshold as their respective stopping power curves, with the yields from the heavier ^{197}Au beam increasing already at lower velocities and faster with primary ion velocity than those of the lighter ^{63}Cu beam. The yield curve of the very light ^{12}C primary ion beams therefore is very flat and shows almost no variation between velocities of $1\,\mathrm{cm\,ns^{-1}}$ to $2\,\mathrm{cm\,ns^{-1}}$. This is in line with the also very flat electronic stopping power curve of ^{12}C in this velocity region.

Additionally the data for ^{63}Cu on arginine and PEG indicate increased secondary ion yields at much lower velocities, where nuclear stopping is the dominant interaction between primary ion and sample material. In the case of leu-enkephalin this effect is not apparent from the ^{63}Cu data available, since measurements at low enough velocities were not performed. This yield increase at velocities below $0.25\,\mathrm{cm\,ns^{-1}}$ can be interpreted by the effect of overlaying the two branches of nuclear and electronic yield functions identified by Albers et al. (1982): Since the total yield is determined by integrating counts over the whole mass spectrum, it does not distinguish between monoatomic and larger fragment and molecular secondary ions. However it is curious that there is no evidence of the nuclear stopping yield branch for the ^{197}Au data on both arginine and leu-enkephalin, despite ^{197}Au exhibiting a higher nuclear stopping than ^{63}Cu. Both are not directly comparable though, since ^{197}Au also exhibits

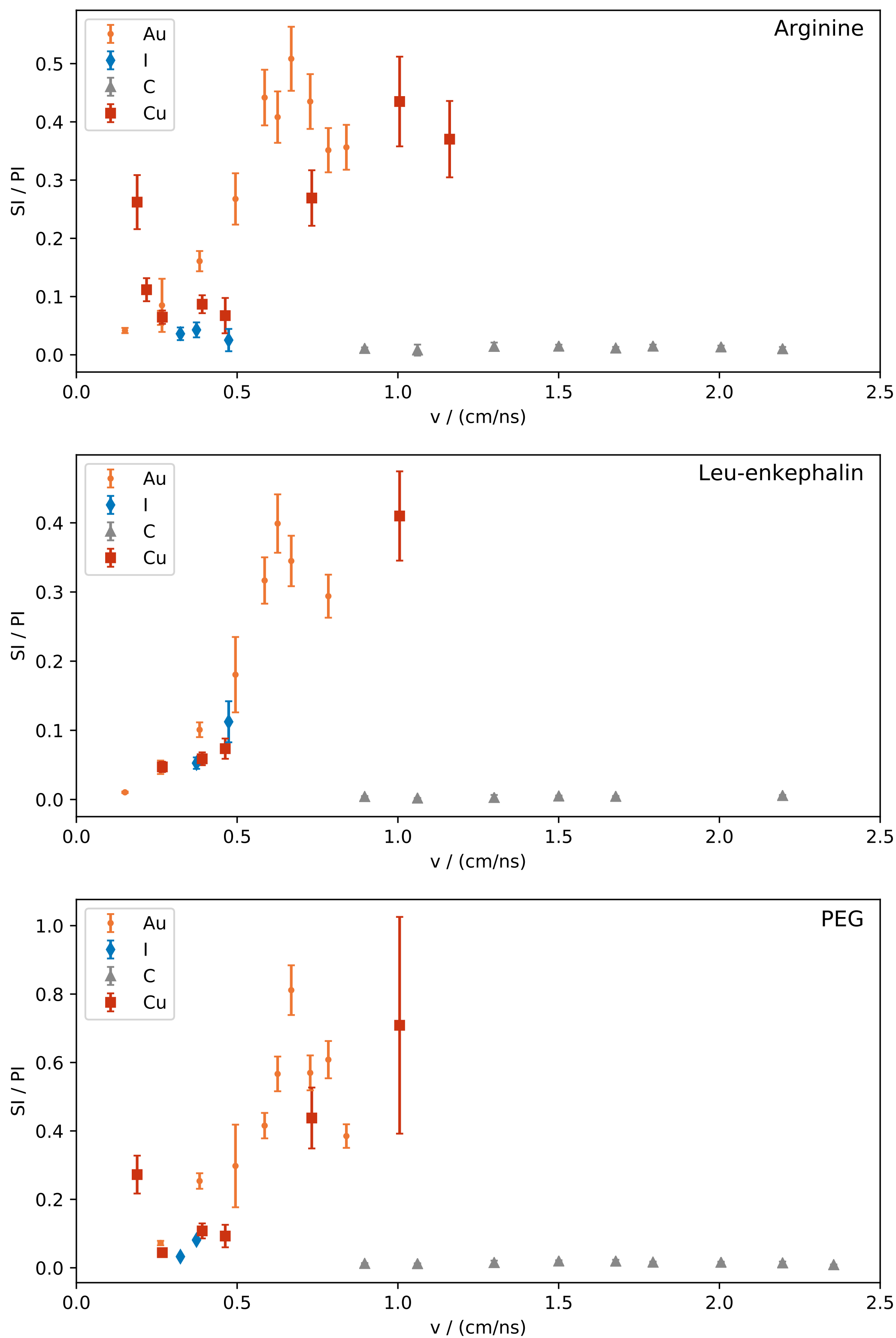

Figure 5.6.: Total secondary ion yield plotted vs. primary ion velocity measured from arginine (top), leu-enkephalin (center) and PEG (bottom) using a range of monoatomic ion beams.

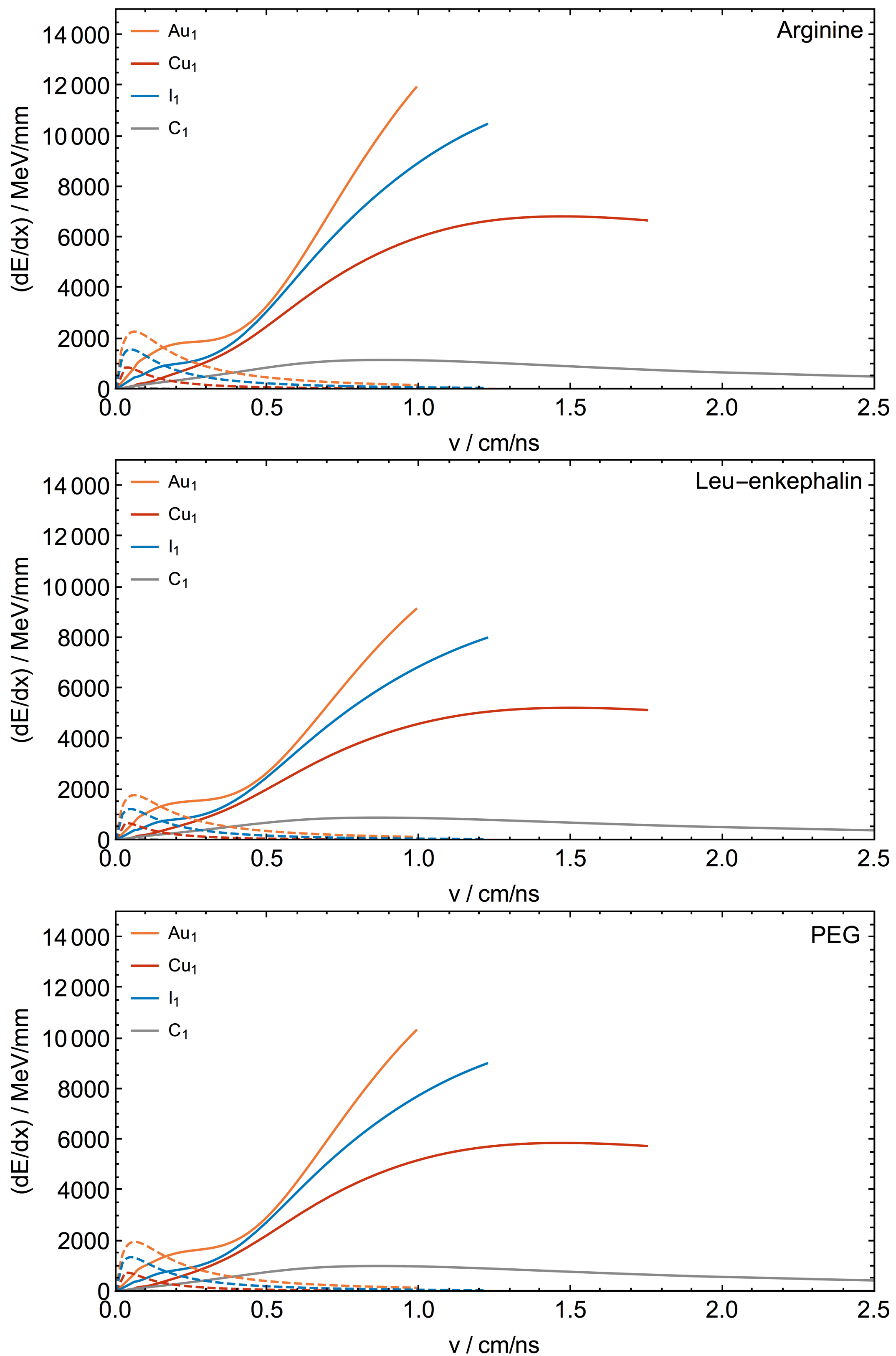

Figure 5.7.: Electronic (solid lines) and nuclear (dashed lines) stopping power in arginine (top), leu-enkephalin (center) and PEG (bottom) as a function of primary ion velocity for C, Cu, I and Au.

a significantly higher electronic stopping at those smaller velocities, so its actual ratio of electronic to nuclear stopping is higher and might be a better indicator for where to expect the crossing point from nuclear to electronic stopping yield branches. Additionally there could be cooperative sputtering effects at play in the velocity region where both the nuclear and electronic branches of the yield function overlap.

In this context it is also instructive to analyse the data with regard to the emission of multiple secondary ions from a single projectile impact to make conclusions on the origin of increased yield of secondary ions. Therefore in Figure 5.8 the fraction of multi-stop events (i.e. events for which more than a single secondary ion was detected per primary ion impact) is plotted as a function of primary ion velocity. The relative fraction of such multi-stop events in the secondary ion spectrum increases steeply from ca. 40 % to 80 % around the same threshold velocity as observed for the overall yields. This indicates that the increase in secondary ion yield for higher velocities is primarily due to the simultaneous emission of two or more ions from a single projectile impact. But for lower velocities below $0.25\,\mathrm{cm\,ns^{-1}}$ the fraction of multi-stop events from all three samples does not show such a significant increase, despite the observed yield attributed to the higher amount of nuclear stopping. It thus seems that the emission of multiple secondary ions from a single primary ion impact is significantly promoted by electronic stopping, while nuclear stopping favours the emission of single secondary ions.

Besides, the data from measurements performed with ^{12}C show a clear decrease in multi-stop frequency with increasing primary ion velocity. This hints at a close connection to the amount of electronic stopping power deposited in the sample material.

Finally, for the ^{197}Au data a maximum in total secondary ion yield is reached for velocities in the range of $0.6\,\mathrm{cm\,ns^{-1}}$ to $0.7\,\mathrm{cm\,ns^{-1}}$, with secondary ion yield starting to decrease again for even higher primary ion velocities. The same behaviour is indicated also for the ^{63}Cu data, although there the maximum in the yield curve seems to appear at higher velocities and could only be crossed on the arginine sample (at a velocity of approx. $1.0\,\mathrm{cm\,ns^{-1}}$). Again this is generally in line with what has been reported before by Albers et al. (1982),

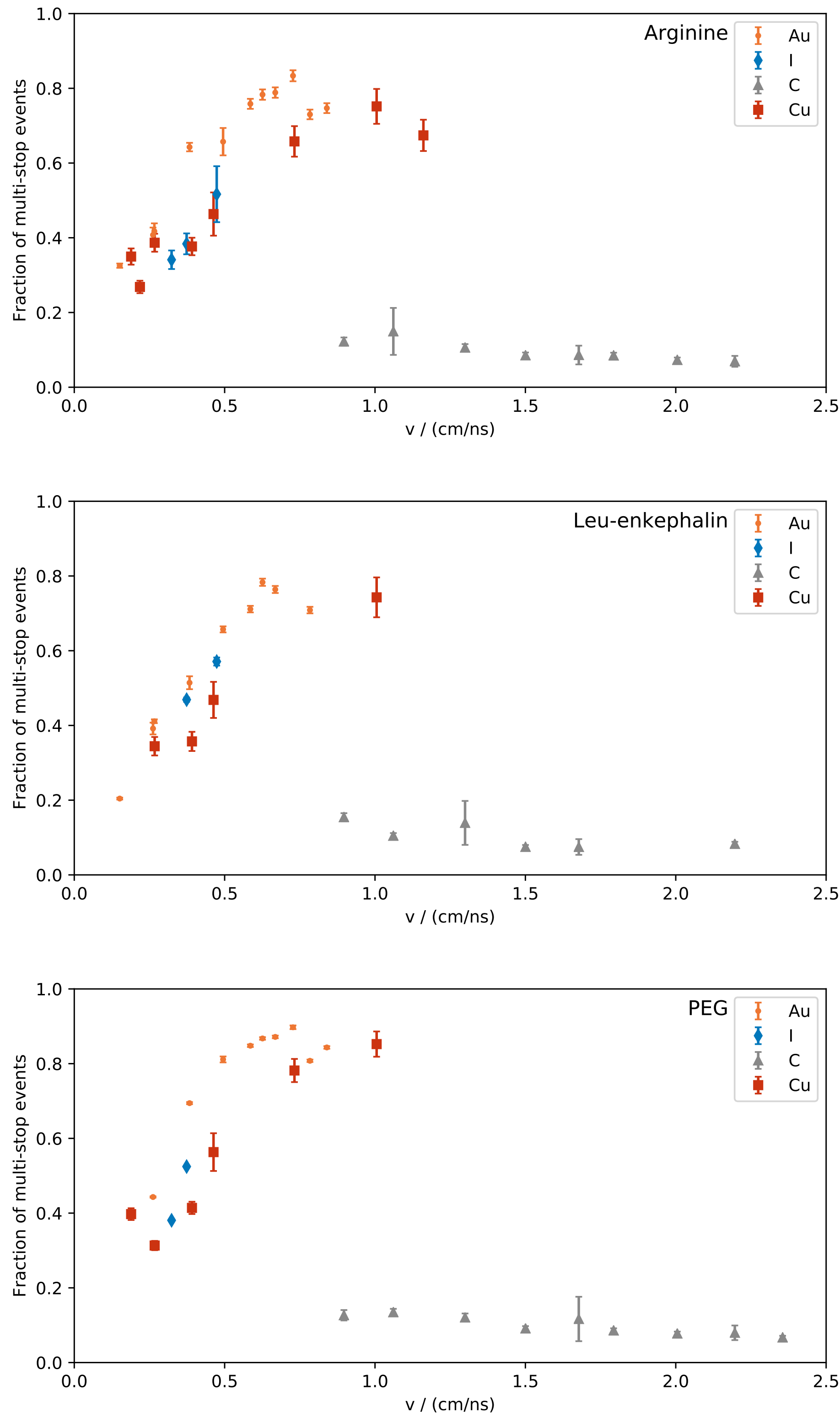

Figure 5.8.: Fraction of detected multi-stop events (more than a single secondary ion detected per primary ion impact) from arginine (top), leu-enkephalin (center) and PEG (bottom) as a function of primary ion velocity for measurements performed with C, Cu, I and Au.

however their measurements were made using ^{16}O and ^{32}S. They also observed yields from the heavier ^{32}S increasing and reaching their maximum at lower velocities than those from ^{16}O primary ions, however their yield curve for protonated valine ($C_5H_1NO_2$) ions from ^{16}O impacts peaks at a velocity of 0.7 cm ns^{-1}, comparable with the data reported here for a heavier ^{63}Cu beam. Given that no significant shift in total secondary ion yield behaviour between the three different sample materials was observed it is rather unlikely that this offset is caused by the change in sample material - however one has to consider that yields for large molecular ions could peak at higher velocities compared to the total secondary yield as measured here, which also includes significant contributions from monoatomic and fragment ions. This effect will be discussed and analysed in more detail when looking at individual peak yields in the Chapter 5.4.

Overall the data indicates a steep increase in secondary ion yields when a certain projectile velocity threshold is surpassed. Since this velocity directly determines the maximum velocity of the δ-electrons generated in the material, this could be interpreted as a threshold in the δ-electron velocity that is required to induce increased emission of secondary ions from the outer ultratrack region. At around the same threshold also the simultaneous emission of multiple ions (multi-stop events) shows a similar increase, indicating that the indirect sputtering involving δ-electrons favours multi-ion emission. Conversely the observed increase in secondary ion yield at lower velocities attributed to increased nuclear stopping and ion emission primarily from the infratrack does not coincide with a similar increase in the fraction of multi-stop events observed. This suggests that multi-ion emission is promoted by faster primary ions and a high number of δ-electrons, potentially indicating a close connection to the ionisation probability of secondary particles.

5.3.2. Scaling with electronic stopping power

The same data is plotted against electronic stopping power of the primary ion in the sample material in Figure 5.9. Positive ion yields increase monotonically with deposited electronic

stopping power in the stopping power region above the lower threshold where the nuclear sputtering yield branch becomes relevant (around $\left(\frac{dE}{dx}\right)_e = 1 \cdot 10^3\,\mathrm{MeV\,mm^{-1}}$) and below the point where the maximum of the secondary ion yield curve is reached (around $\left(\frac{dE}{dx}\right)_e = 5 \cdot 10^3\,\mathrm{MeV\,mm^{-1}}$). However, at a certain electronic stopping power the observed secondary ion yields saturate and level off respectively even show a slight decrease with further increasing electronic stopping power.

Only the data from ^{12}C does not completely fit into this picture, as yields for all three samples only show a much flatter or almost no scaling with electronic stopping power. It has to be noted though, that ^{12}C is the only primary ion beam for which the electronic stopping decreases with increasing energy of the primary beam (compare Figures 5.6 and 5.7).

This deviates from the earlier reported yield scaling behaviour with $\left(\frac{dE}{dx}\right)_e$ of positive molecular leucine ions by Hedin, Håkansson, Salehpour, et al. (1987). One difference between the datasets is that Hedin, Håkansson, Salehpour, et al. (1987) used different primary ions (7.4 MeV ^{12}C, 9.9 MeV ^{16}O, 19.7 MeV ^{32}S, 48.7 MeV ^{79}Br and 78.2 MeV ^{127}I) with energies selected such that all ions impact the sample with the same velocity of $1.1\,\mathrm{cm\,ns^{-1}}$ and in charge state equilibrium after passing a $100\,\mathrm{\mu g\,cm^{-2}}$ carbon foil. This was done to minimize the influence of the primary ion charge state on the secondary ion yields (although the equilibrium charge states of the primary ions deviate, stopping power values are usually tabulated for ions in charge state equilibrium). The constant velocity keeps the track radius of the primary ion in the sample constant, which is scaling with primary ion velocity (Hedin, Håkansson, Salehpour, et al. 1987). In contrast, the measurements presented here were performed with different velocity ions of varying charge states. It is therefore possible that the steep scaling with electronic stopping power observed here is partly due to a yield increase from higher charge states used for the higher energy primary ions. This would be in line with the slower scaling of ^{12}C yields, where the primary ion energy and therefore its used charge state actually decreases with increasing electronic stopping power (since the beam parameters are located on the high energy side of the Bragg peak).

Another potential factor is that for the higher energy primary ions used by Hedin, Håkans-

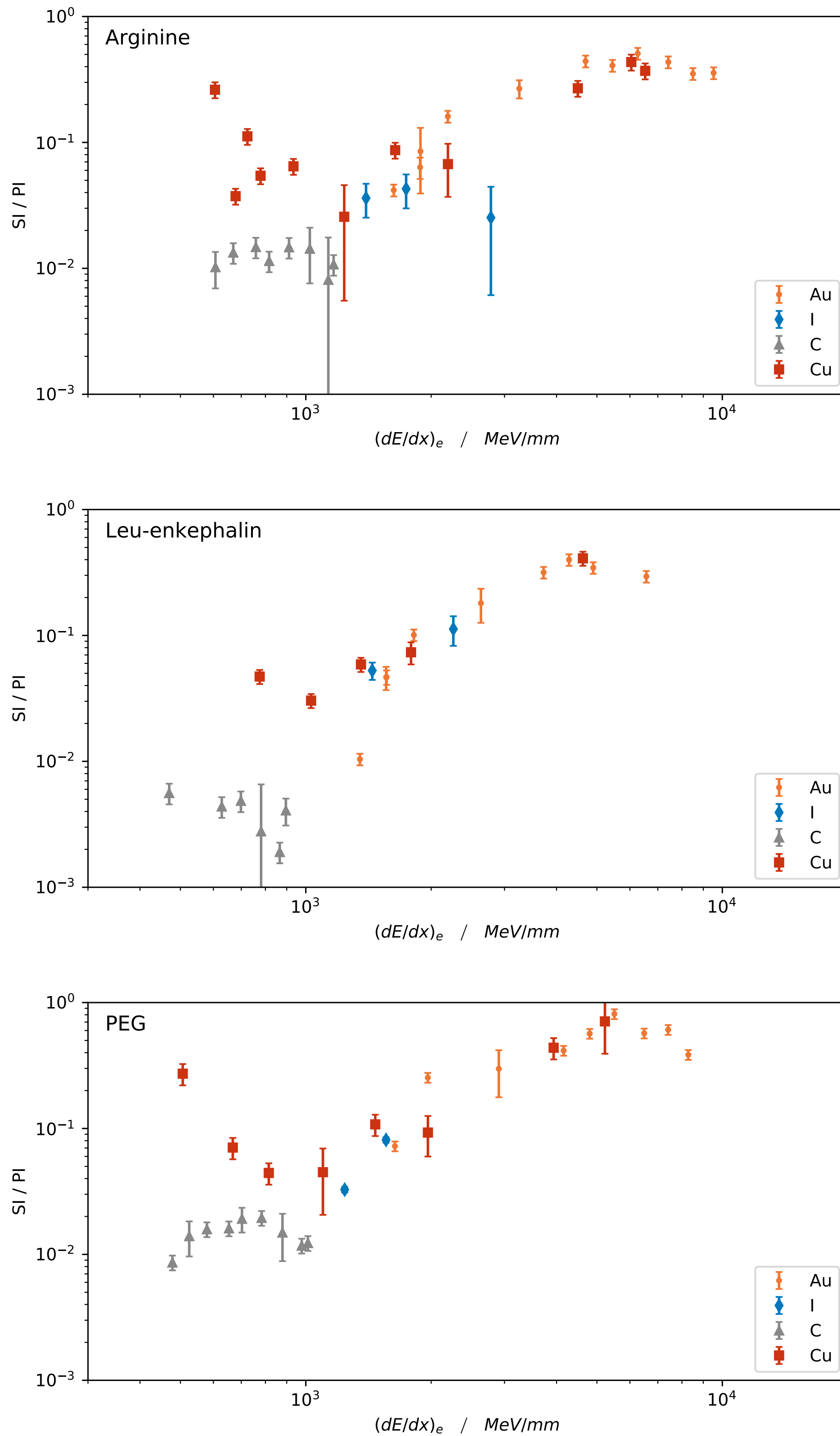

Figure 5.9.: Total secondary ion yield measured from arginine (top), leu-enkephalin (center) and PEG (bottom) samples using a range of primary ion beams as a function of their respective electronic stopping power.

son, Salehpour, et al. (1987), the electronic stopping power is significantly higher than at the point where secondary ion yields are maximized in our data, therefore leading to a slower overall scaling. However, this in turn means that for heavy primary ions total secondary ion yields reach their maximum at lower velocities (and therefore smaller track radii in the sample material) than for lighter primary ion projectiles. It will be specifically interesting whether this effect is also present for individual mass peak yields in the following chapters.

Nevertheless the observed secondary ion yield is clearly not scaling with a power of $\left(\frac{dE}{dx}\right)_e$ as suggested by many theoretical approaches: Apart from the influence of nuclear sputtering at lower projectile velocities, the observed saturation effect observed for high electronic stopping powers indicates a much more complex behaviour. In terms of the phenomenological view introduced in Chapter 2.3 it would be reasonable to assume that such an effect could be caused by an extremely high energy deposition within the inner infratrack region. A corresponding increase in size of the ultratrack region would not be sufficient to counterbalance the stagnant yields from the infratrack if the density of secondary δ-electrons (which is limited by their maximal projected range) is not anymore sufficient to induce desorption in the outer parts of the ultratrack.

5.4. Peak yields and fragmentation

It is especially interesting to compare the yield behaviour of different mass peaks in the secondary ion mass spectrum: This gives a significantly deeper insight into the desorption and ionization processes occurring and reveals differences between secondary ion fragments and full-mass molecules. Thus it can be used to study fragmentation induced in the sample material by the primary ion bombardment. In case of MeV-SIMS, previous studies have reported a significant relative enhancement of molecular secondary ion yields and respectively a reduction in fragmentation compared with conventional keV-SIMS (Jones, Matsuo, et al. 2011).

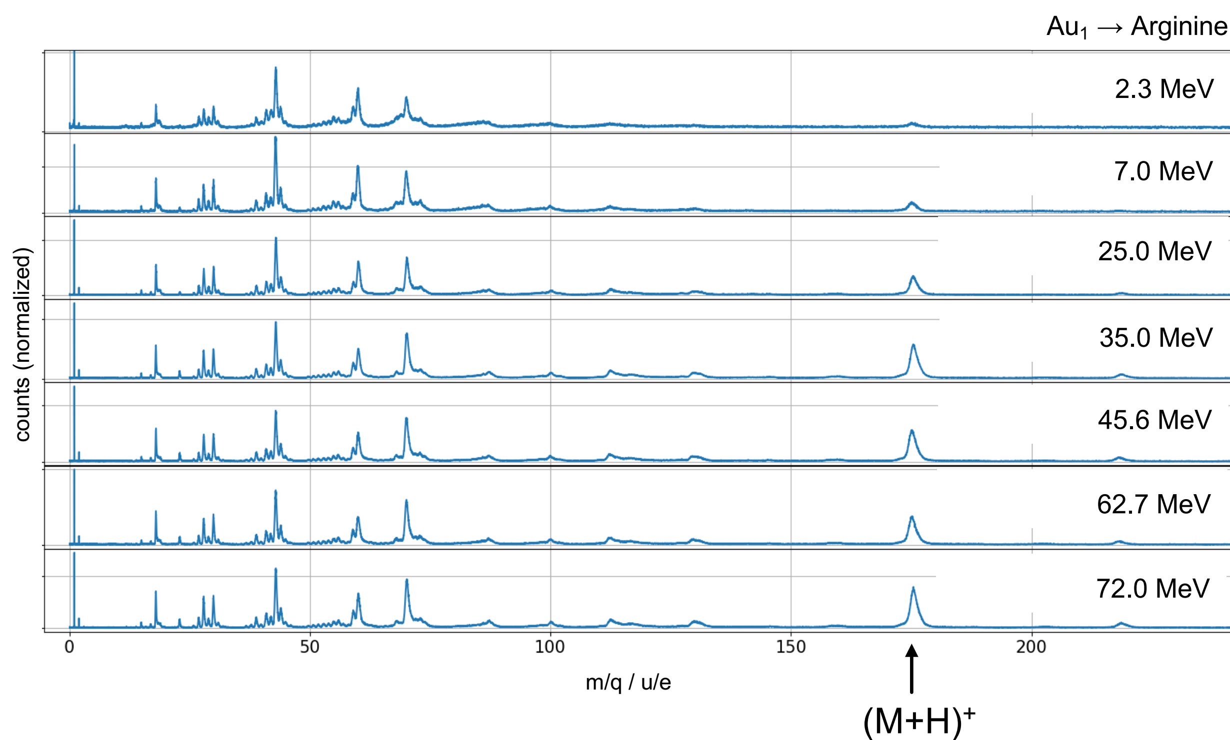

Figure 5.10.: Positive secondary ion mass spectra recorded from arginine sample with a Au monoatomic primary ion beam with increasing primary ion energy. With increasing energy, the $(M + H)^+$ full-mass arginine peak significantly increases in relative intensity compared to the rest of the spectrum. All spectra are normalized to the incident primary ion rate.

With the CHIMP setup this effect was confirmed and quantified by performing MeV-SIMS with primary ion beams of increasing energy: The secondary ion mass spectra measured from arginine using monoatomic ^{197}Au primary ion beams with seven different energies have been measured and results are plotted in Figure 5.10. While the low-mass portion of the spectra is comparable in intensity in all of the spectra, the full mass molecular $(M + H)^+$ arginine peak significantly increases in relative intensity with increasing primary ion beam energy.

To study fragmentation effects in more detail and quantify the changes across the stopping power regime covered, the next Chapter 5.4.1 will first take a closer look at the individual secondary ion peak yields of the most significant peaks for all three of the samples as identified in Chapter 5.1. Then these individual secondary ion peak yields will be put in relation to each other by normalizing e.g. the yield of a fragment ion to the one of the corresponding molecular ion, resulting in a suitable metric to quantify fragmentation. For selected pairs of mass peaks the fragmentation data of all measurements performed is compiled and their dependence on electronic and nuclear stopping power of the primary ion is discussed in Chapter 5.4.2. Additional fragmentation data for a wider range of mass peaks is presented in Appendix C.3.

5.4.1. Scaling of individual peak yields with electronic stopping power

In Figure 5.11 the secondary ion yields of the most significant individual peaks in the mass spectrum of arginine as well as the total secondary ion yield are plotted as a function of electronic stopping power of the primary ion beam. In case of the measurements with ^{197}Au primary ions all mass peaks as listed in Table 5.1 are included. Since many fragment mass peaks show a very similar behaviour, only data from the $m = 43\,$u, $m = 70\,$u and $m = 175\,$u mass peaks are shown for the ^{12}C and 63 Cu measurements, respectively. While yields of the fragment ions scale rather similarly, the same cannot be said of the protonated molecular arginine ion with mass $m = 175\,$u: Its yield increases significantly faster with electronic stopping power for all three different primary ion species. For both ^{63}Cu and ^{197}Au primary beams at the highest energies used it ends up being the most intensive peak in the secondary

mass spectrum. Again, this fast scaling reaches a saturation point which for the ^{197}Au primary ion beam is at an electronic stopping power on the order of $\left(\frac{dE}{dx}\right)_e = 5 \cdot 10^3\,\mathrm{MeV\,mm^{-1}}$. For even higher electronic stopping power values the yield seems to stay roughly constant or even decrease slightly.

The data for the most significant peaks in the mass spectrum of the leu-enkephalin sample as well as the total secondary ion yield is plotted in Figure 5.12. Again the data of all mass peaks as listed in Table 5.2 is shown for the ^{197}Au measurements, while for the ^{12}C and ^{63}Cu measurements only the data from the representative $m = 43\,\mathrm{u}$, $m = 120\,\mathrm{u}$ and $m = 279\,\mathrm{u}$ mass peaks is shown. For the rather high mass peaks of the larger fragment and molecular ions, the uncertainties of the determined yields are significantly larger due to the comparably limited mass resolution and therefore large uncertainties in the peak fitting and background reduction. Nevertheless, a similar picture as in the case of arginine emerges: While the yields from ^{12}C primary ions are very low and show practically no scaling with electronic stopping power, for both ^{63}Cu and ^{197}Au primary ion beams most of the peak yields increase significantly with electronic stopping power. The yields of heavier and larger fragment ions show a faster increase. For ^{197}Au primary ions the full molecular peak at mass $m = 556\,\mathrm{u}$ also seems to scale slightly faster although the effect is by far not as noticeable as in the case of arginine. Above an electronic stopping power of approximately $\left(\frac{dE}{dx}\right)_e = 3.5 \cdot 10^3\,\mathrm{MeV\,mm^{-1}}$ yields saturate and even a following slight decline in secondary ion yields is evident.

Finally the data for the secondary ion mass peaks from PEG is shown in Figure 5.13. For the ^{197}Au measurements, data for all mass peaks as listed in Table 5.3 are shown, but only the data from the $m = 45\,\mathrm{u}$, $m = 64\,\mathrm{u}$ and $m = 158\,\mathrm{u}$ mass peaks are plotted for the ^{12}C and ^{63}Cu measurements. Due to the polymer nature of this sample material with an average molecular mass of several thousands of u, no full-mass molecular peak yields could be determined. However it is still instructive to study differences between the scaling of different fragment mass peaks: For yields from ^{12}C primary ions we see a similar scaling of all the peak yields with roughly $\left(\frac{dE}{dx}\right)_e$. When ^{63}Cu primary ions are used, the yield curves show a clear

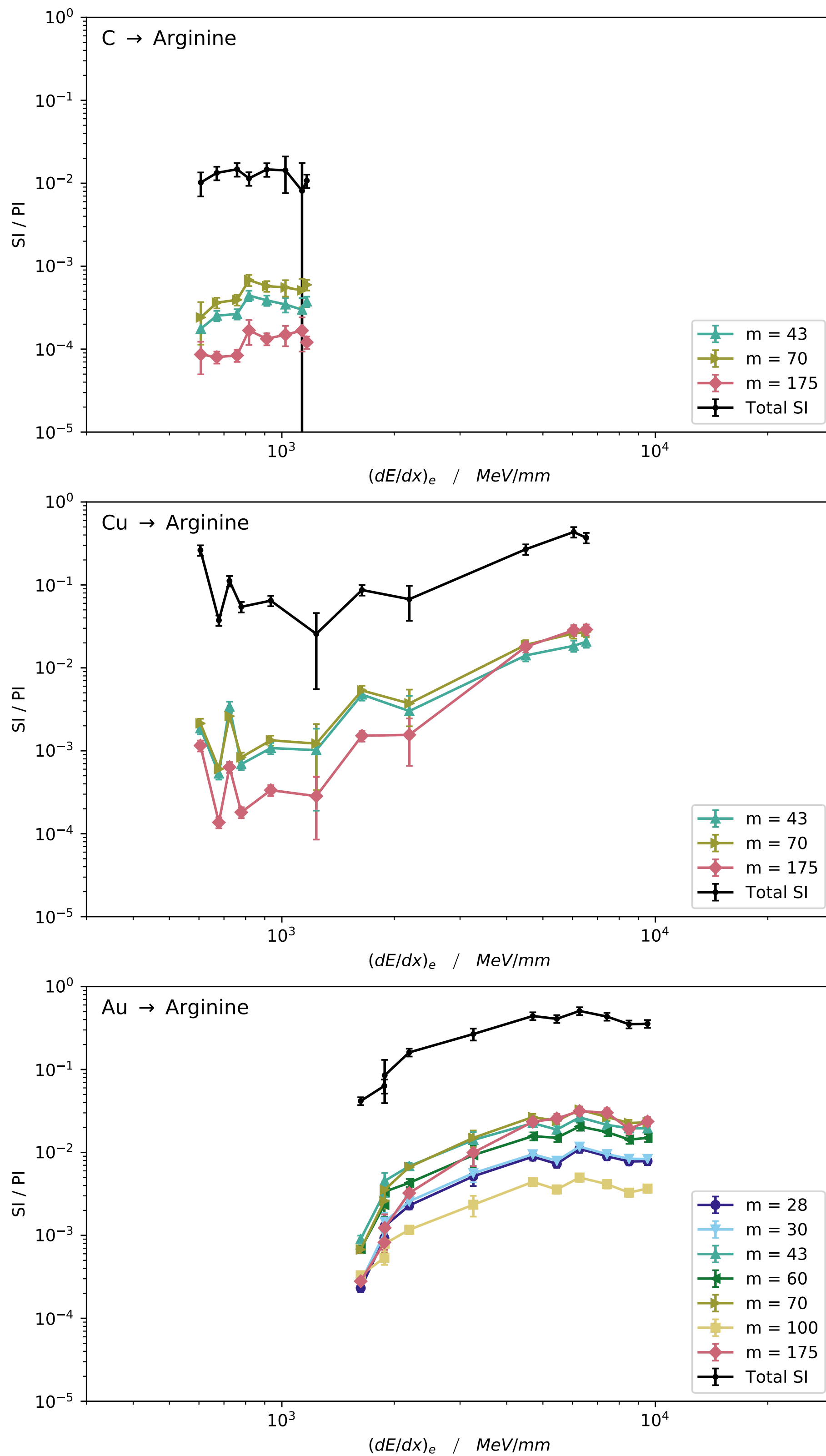

Figure 5.11.: Secondary ion peak yields measured from arginine sample using primary monoatomic ion beams of ^{12}C (top), ^{63}Cu (center) and ^{197}Au (bottom) as a function of their respective electronic stopping power.

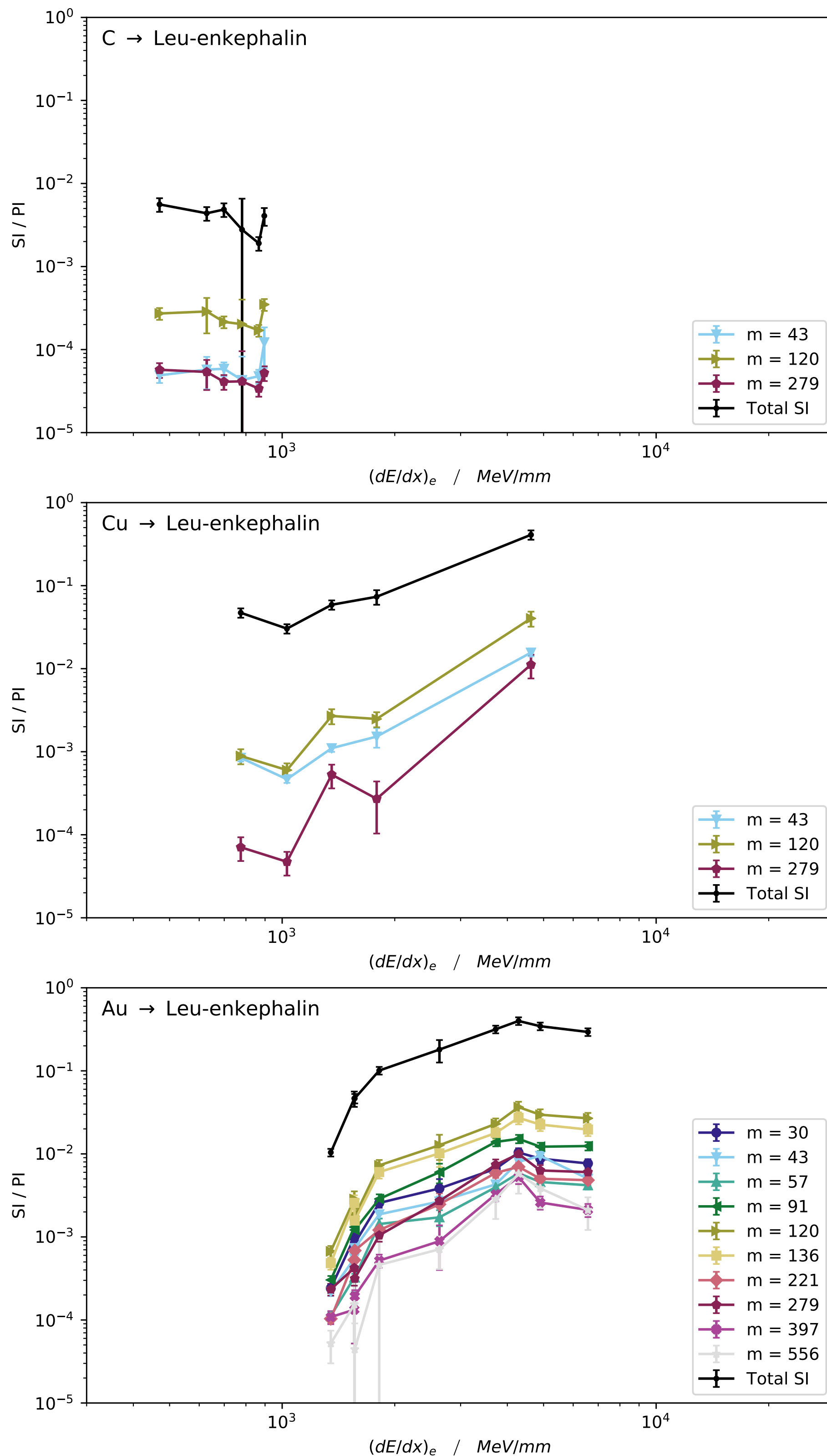

Figure 5.12.: Secondary ion peak yields measured from leu-enkephalin sample using primary monoatomic ion beams of ^{12}C (top), ^{63}Cu (center) and ^{197}Au (bottom) as a function of their respective electronic stopping power.

nuclear sputtering yield branch at low electronic stopping below $\left(\frac{dE}{dx}\right)_e = 1 \cdot 10^3\,\mathrm{MeV\,mm^{-1}}$, which seems to preferentially manifest for the $m = 158\,\mathrm{u}$ mass peak.

Noticeable is here the fragment peak with mass $m = 45\,\mathrm{u}$, which exhibits a faster scaling than the other fragments. Since this mass corresponds to the repeat unit of the polymer, it is possibly the best candidate to proxy the molecular yield scaling. This is in spite of the still significant fragmentation needed to separate out a single repeat unit from the long polymer chain. The yields from ^{197}Au primary ions also show a saturation and slight decline for electronic stopping powers above approximately $\left(\frac{dE}{dx}\right)_e = 4.5 \cdot 10^3\,\mathrm{MeV\,mm^{-1}}$.

When compared to the data published by Hedin, Håkansson, Salehpour, et al. (1987), the data presented here exhibits significantly faster scaling than they reported for positive secondary ions which are desorbed using a range of different primary ions with constant velocity. Instead the measurements rather match the scaling they found for neutral molecular secondary ion yields from leucine. However, the influence of the nuclear yield branch at low velocities and the observed saturation effects at high electronic stopping make a direct comparison difficult. In any case, the scaling of secondary ion yields cannot be described by a simple power of $\left(\frac{dE}{dx}\right)_e$. If one assumes that the underlying desorption process yield scales with $\left(\frac{dE}{dx}\right)_e^3$ as indicated by neutral molecule yield measurements (Hedin, Håkansson, Salehpour, et al. 1987), the difference in scaling observed here could be explained by an ionization yield varying with primary ion velocity (or crater size). This ionization yield behaviour would then modulate the underlying desorption yield and could reproduce the yield curves as measured for individual ions with changing primary ion velocity.

While at very low velocities nuclear stopping causes sputtering of many small fragment ions, additional electronic stopping in the infratrack region increases the secondary ion yields. As soon as the δ-electron velocity approaches the threshold value observed, electronic sputtering from the ultratrack region leads to a faster yield increase for larger and heavier secondary ions. With a further increase of stopping power both the infratrack and ultratrack radii increase, leading to a monotonous enhancement of both fragment and full mass molecular secondary ion yields. At one point however the combination of a very high energy density

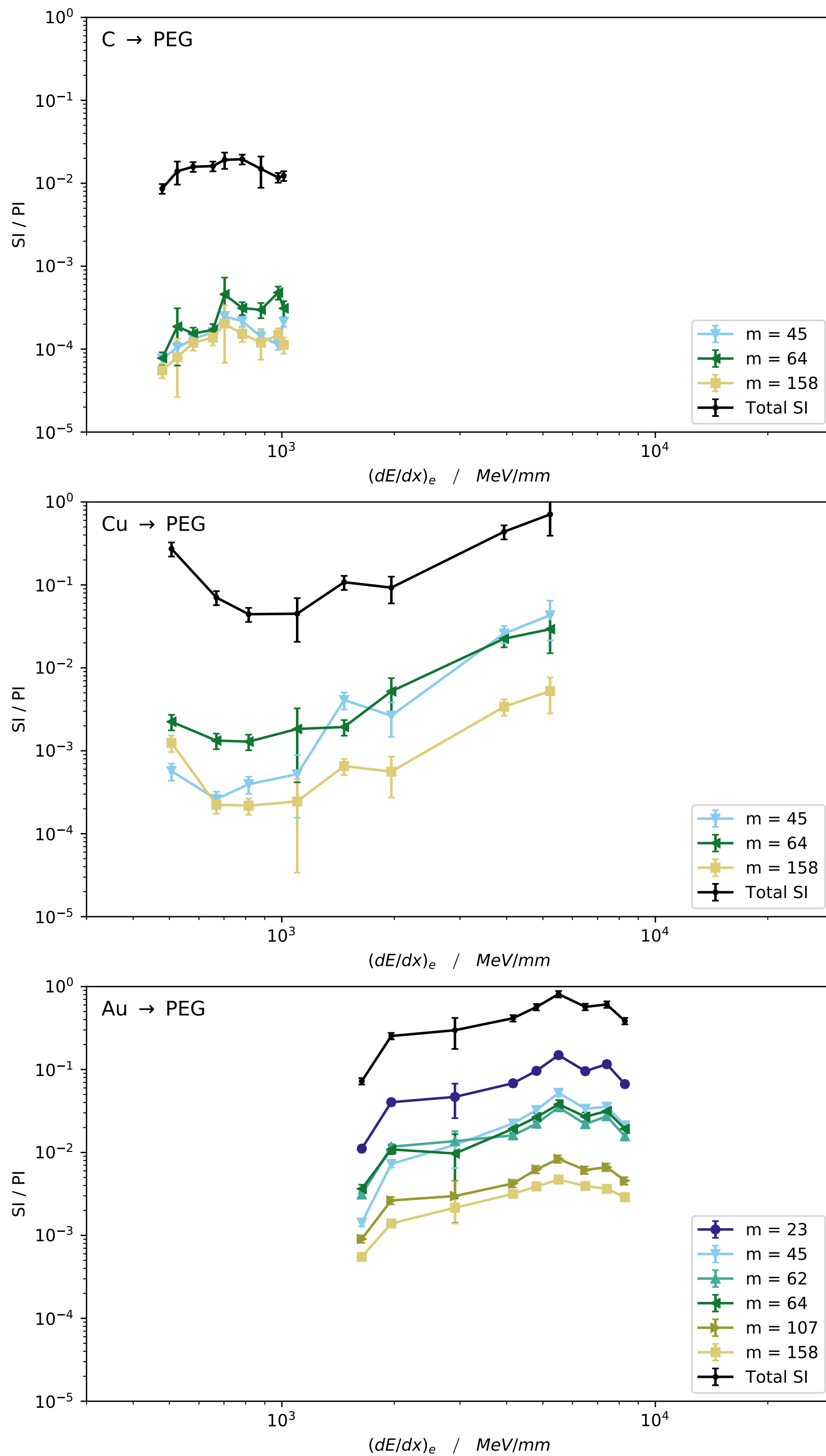

Figure 5.13.: Secondary ion peak yields measured from PEG sample using primary monoatomic ion beams of ^{12}C (top), ^{63}Cu (center) and ^{197}Au (bottom) as a function of their respective electronic stopping power.

in the infratrack region and an insufficient density of δ-electrons in the outer regions of the ultratrack inhibits further yield increases, resulting in the observed saturation effect.

5.4.2. Fragmentation behaviour with electronic and nuclear stopping

To further characterize the secondary desorption and ionization processes in MeV-SIMS it is instructive to look at the relative changes in secondary ion yields for different fragments and full mass molecular ions of the same spectrum by analysing and comparing their behaviour under different measurement parameters. This approach gives an insight in the fragmentation behaviour occurring during the impact and emission. As a measure of fragmentation, the ratio of a smaller fragment ion yield to a larger fragment or molecular ion yield is calculated for each single spectrum. Then the changes and scaling of this indicator can be tracked throughout the explored stopping power regime.

Especially notable is that for this fragmentation measure the obtained systematic uncertainties due to possible changes in the setup (detection efficiency, ion beam tuning, extraction efficiency) are largely cancelled out. The obtained values therefore show a much smaller scatter and a significantly better reproducibility compared to the total and peak yields studied in the previous chapters.

The obtained data is plotted for different select combinations of secondary ion peaks for each of the three samples measured in a 3D bar plot as a function of both electronic and nuclear stopping power. Plots of ratios of additional mass peaks are included in Appendix C.3. To be able to obtain a good impression of the data and its features, each plot is rendered in three different perspectives: projecting fragmentation vs. the electronic energy loss, projecting fragmentation vs. the nuclear energy loss, and an isometric projection in which most data points should be clearly identifiable. As an orientation an annotated top-down projection indicating the stopping power regime of the measurements is provided for the case of the arginine sample in Figure 5.14. The relative position of the data points in the stopping regime are similar for the other samples, while the absolute stopping power numbers

are of course different.

For these plots multiple repeated datapoints at the same electronic and nuclear stopping power were combined. However, no error bars are plotted for better readability and clarity. The data is coloured according to the primary ion used (^{12}C in gray, ^{63}Cu in red, ^{127}I in blue and ^{197}Au in red).

Arginine

For the arginine sample the fragment ion peaks with masses of $m = 43\,\mathrm{u}$ and $m = 100\,\mathrm{u}$ are of interest and the fragmentation data with respect to the molecular protonated arginine peak at mass $m = 175\,\mathrm{u}$ is plotted in Figures 5.15 and 5.16. Of these, the $m = 43\,\mathrm{u}$ fragments with their dual N-atoms almost certainly have to originate from the guanidino group of the arginine molecules. The $m = 100\,\mathrm{u}$ fragment consists of the aliphatic hydrocarbon straight chain of the arginine molecule and its guanidino group and therefore only requires a single chain break to form.

On first sight the data for both peaks shows the same underlying pattern: Fragmentation decreases by at least a factor of 3 when moving from primary ions with rather low energy deposition to ions with higher energy deposition at the sample surface. In the projection plots vs. electronic and nuclear stopping power this behaviour seems to be evident both when moving towards higher electronic and higher nuclear stopping. However, the scaling is markedly different: While for increased electronic stopping fragmentation decreases rapidly in an almost exponential fashion, the apparent decrease of fragmentation with increasing nuclear stopping is much slower and almost linear. Additionally, one has to keep in mind that nuclear and electronic stopping are still coupled in this view and from the 3D plots it is actually clearly visible that for a single monoatomic primary ion fragmentation increases with increasing nuclear stopping. The apparent decrease in the projected view originates from the data points of the larger cluster primary ions, which seem to reduce fragmentation with increasing primary ion cluster size n. This effect will be examined in more detail in Chapter 5.5.

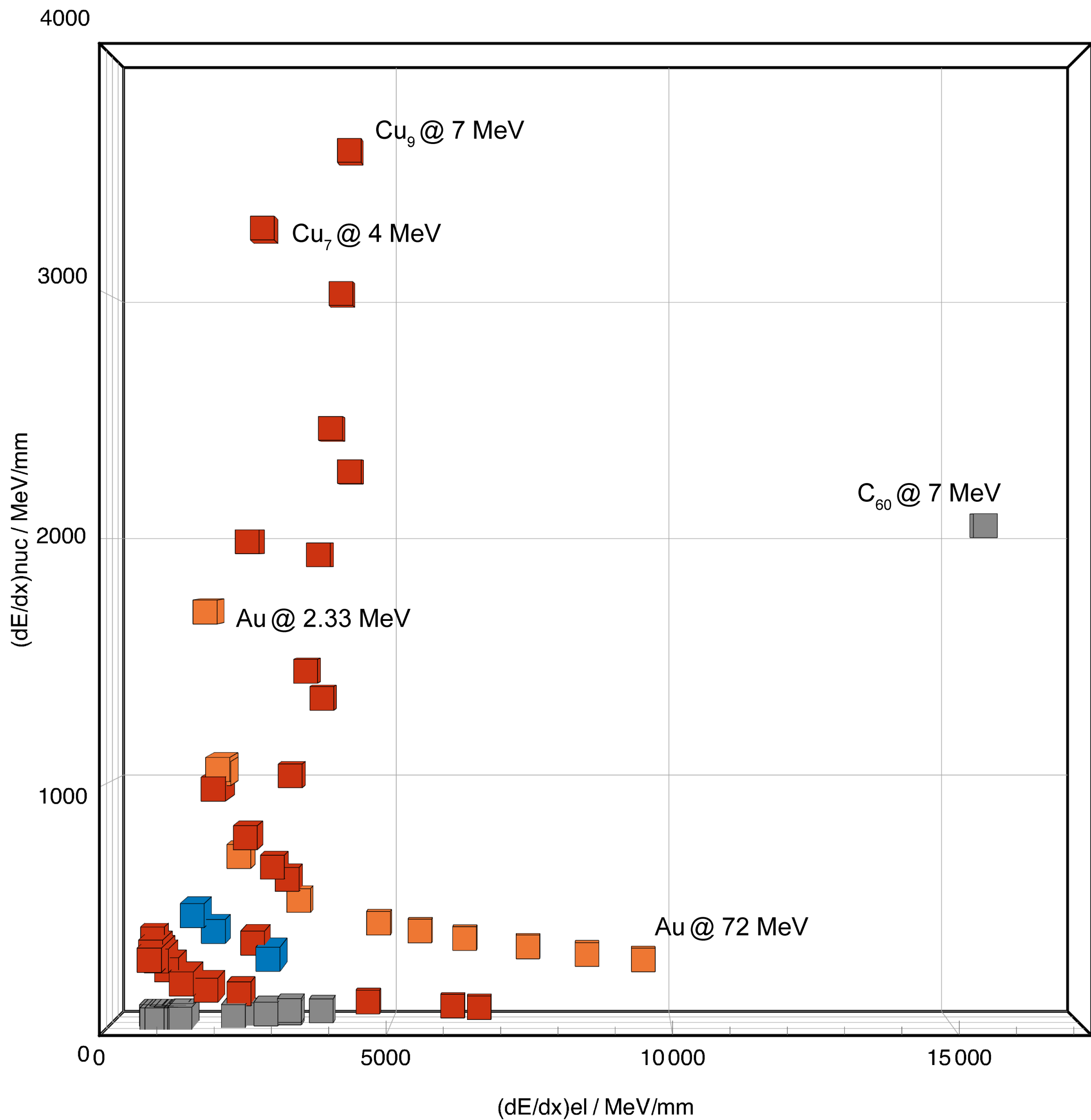

Figure 5.14.: Top-down projection of the fragmentation data ($m = 43\,\mathrm{u}$ normalized to $m = 175\,\mathrm{u}$) of positive secondary ion mass spectra recorded from arginine sample with different monoatomic and cluster ion beams (compare Figure 5.15). The plot is intended to serve as an orientation to identify the different measurements according to their respective stopping power regime as a function of $\left(\frac{dE}{dx}\right)_e$ and $\left(\frac{dE}{dx}\right)_n$.

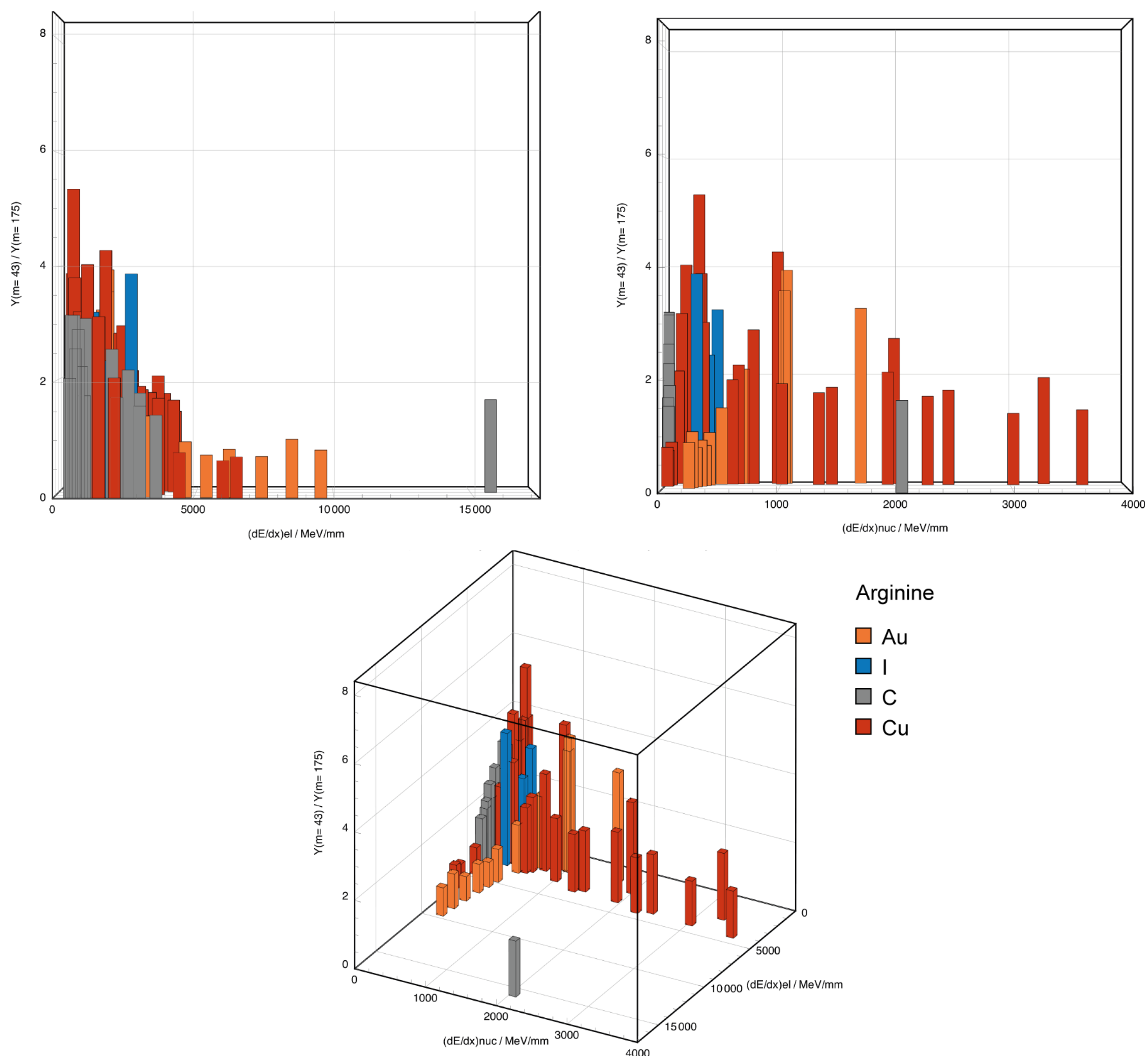

Figure 5.15.: Fragmentation (peak yield of fragment ion with mass $m = 43\,\mathrm{u}$ normalized to yield of molecular ion with mass $m = 175\,\mathrm{u}$) of positive secondary ion mass spectra recorded from arginine sample with different monoatomic and cluster ion beams as a function of $\left(\frac{dE}{dx}\right)_e$ and $\left(\frac{dE}{dx}\right)_n$.

Upon closer inspection, there are some differences between the datasets for different fragment ions: The formation of the small $m = 43\,\mathrm{u}$ fragment ion is significantly more likely than that for the $m = 100\,\mathrm{u}$ fragment ion. The large $m = 100\,\mathrm{u}$ consisting of more than half of the original arginine molecule (only the α-amino and the connected α-carboxylic acid group is detached) shows a very fast decrease in fragmentation already at very low electronic stopping power. In both cases, the data obtained with the large C_{60} primary cluster ions indicates a fragmentation similar to the data obtained with Cu_n primary cluster ions with comparable nuclear stopping power. However for the large $m = 100\,\mathrm{u}$ ion Cu_n cluster size does not seem to have a pronounced effect on fragmentation.

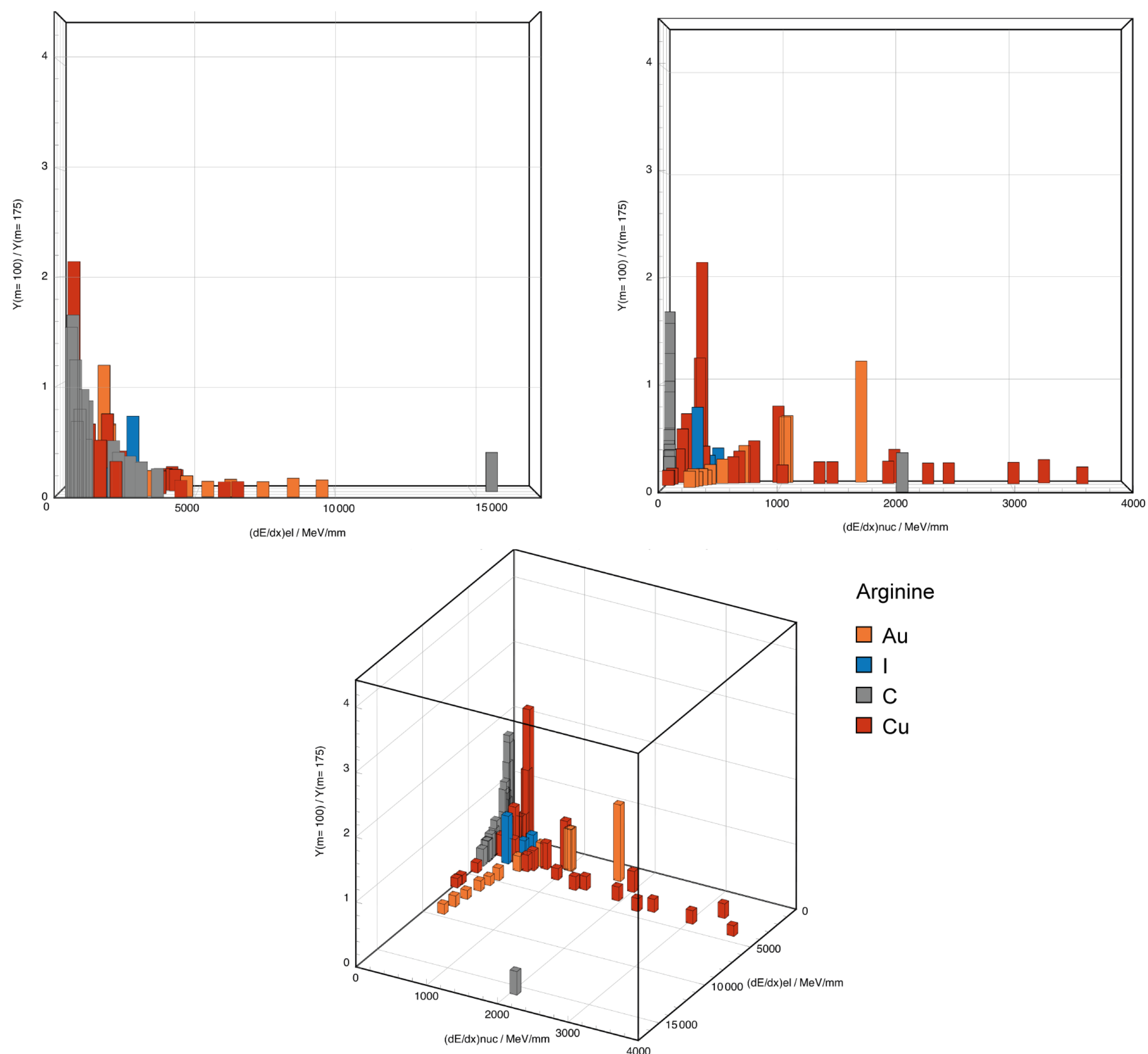

Figure 5.16.: Fragmentation (peak yield of fragment ion with mass $m = 100\,\mathrm{u}$ normalized to yield of molecular ion with mass $m = 175\,\mathrm{u}$) of positive secondary ion mass spectra recorded from arginine sample with different monoatomic and cluster ion beams as a function of $\left(\frac{dE}{dx}\right)_e$ and $\left(\frac{dE}{dx}\right)_n$.

Leu-enkephalin

For the leu-enkephalin sample the yields for the molecular ion with mass $m = 556\,\mathrm{u}$ have too high uncertainties to make any meaningful fragmentation ratio calculations. This is due to the rather low statistics and the limited mass resolution of the spectrometer, such that the background correction significantly impacts the uncertainty of the calculated yields. However, one can still get some insight into the fragmentation patterns as seen in the previous section by setting the relative peak yields of two different fragment ions in relation to each other and studying their changes within the covered stopping power region. Therefore, the ratios for the secondary fragment ion pair with $m = 57\,\mathrm{u}$ and $m = 86\,\mathrm{u}$ are plotted in Figure 5.17. This peak pair was selected according to the leu-enkephalin fragmentation pattern lined out in Figure 5.2: The fragment y ($m = 57\,\mathrm{u}$) is a sub-fragment of the super-fragment a_4 ($m = 86\,\mathrm{u}$).

Compared to its larger super-fragment, the $m = 57\,\mathrm{u}$ fragment ion forms less frequently. However, their yield ratio shows a classical fragmentation pattern with decreasing fragmentation towards higher electronic stopping and increasing fragmentation with higher nuclear stopping. It also decreases with cluster size for the Cu_n primary ions. For C_{60} primary cluster ions the fragmentation is once again significantly lower than for other ion species with comparable nuclear stopping, indicating that the large cluster ions favour the formation of the larger fragment or even intact molecular ions.

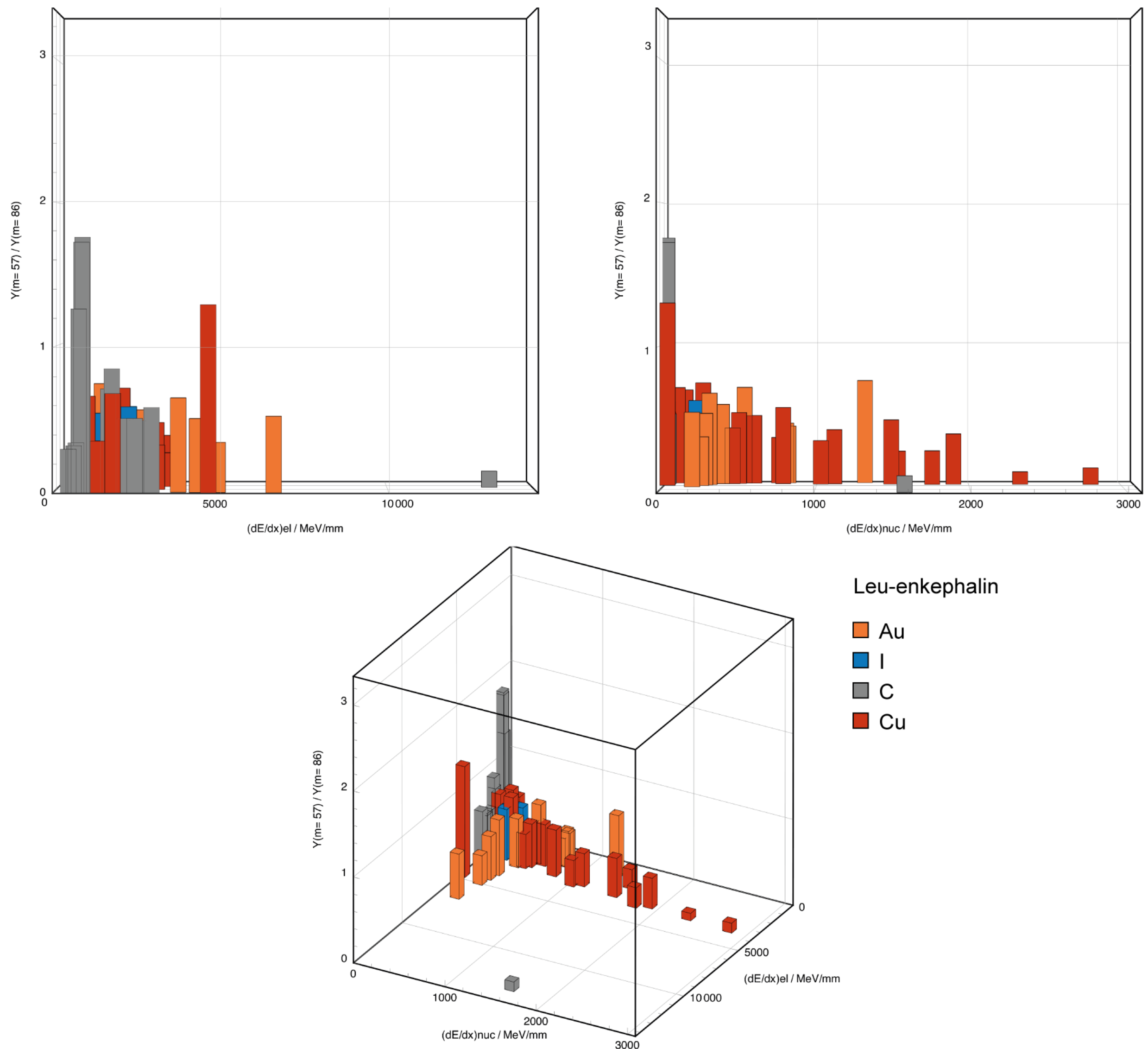

Figure 5.17.: Fragmentation (peak yield of fragment ion with mass $m = 57\,\text{u}$ normalized to yield of fragment ion with mass $m = 86\,\text{u}$) of positive secondary ion mass spectra recorded from leu-enkephalin sample with different monoatomic and cluster ion beams as a function of $\left(\frac{dE}{dx}\right)_e$ and $\left(\frac{dE}{dx}\right)_n$.

PEG

For the PEG sample there is also no full-mass molecular peak detectable in the secondary ion mass spectra, since the material mainly consists of polymer chains with molecular masses of 1000 u to 3000 u. Instead, one can put the fragment yields of the PEG repeat unit with mass $m = 45\,\mathrm{u}$ in relation to other larger fragment ions: The $m = 64\,\mathrm{u}$ mass peak, which can be most likely identified as 2-fluoro ethanol i.e. the PEG repeat unit with one attached fluorine and hydroxy group, was used for normalisation of the $m = 45\,\mathrm{u}$ peak yields. The respective ratios are plotted in Figure 5.18.

When looking at this yield ratio the observed pattern is again familiar: The relative yield of the repeat unit decreases with increasing electronic stopping and increases with increasing nuclear stopping. While the increased cluster size of Cu_n primary ions seems to only slightly favour the formation of the repeat unit ion, the bombardment with C_{60} primary cluster ions markedly increases the likelihood to form a repeat unit up to the highest level that has been observed with monoatomic C primary ions.

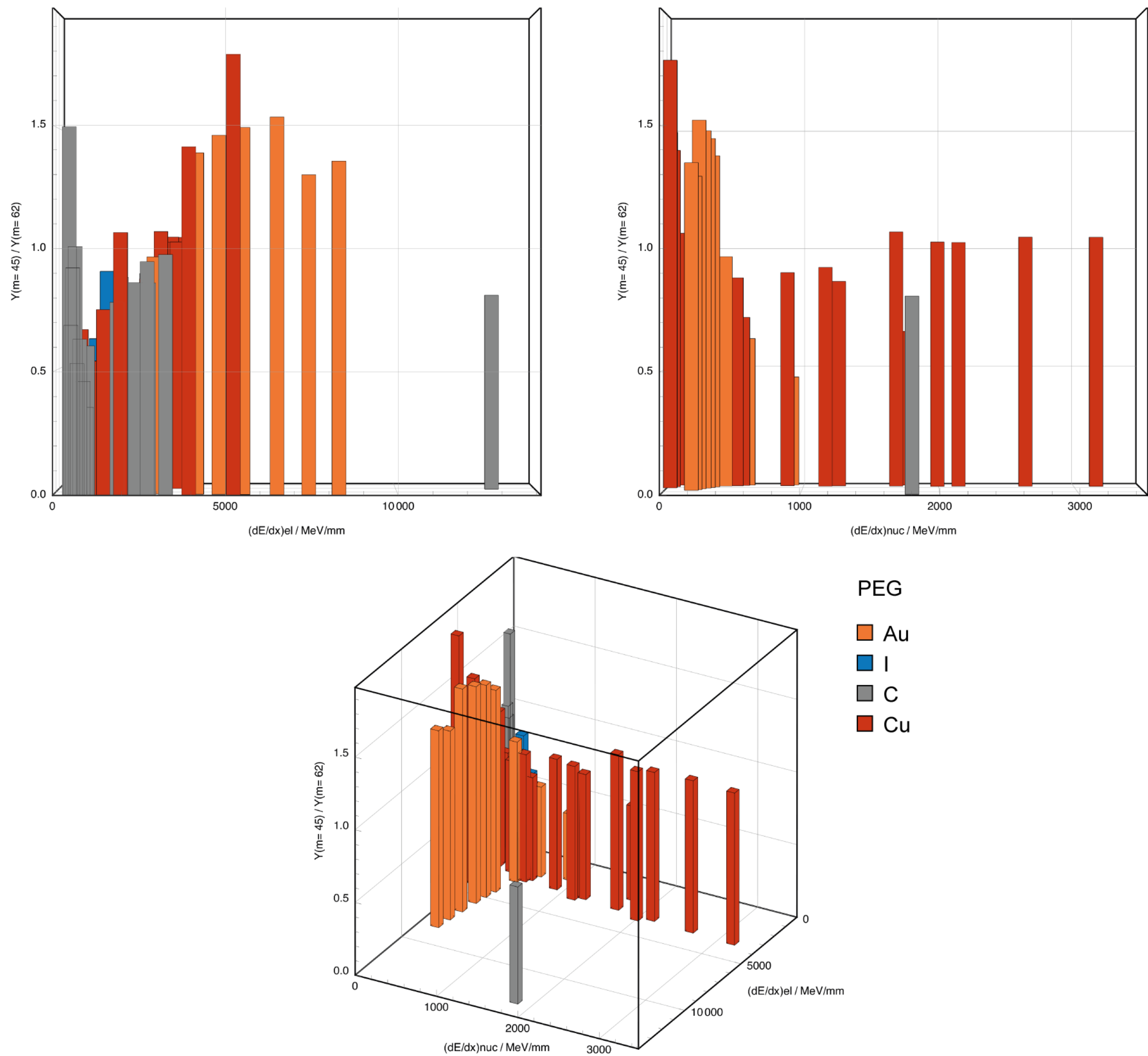

Figure 5.18.: Fragmentation (peak yield of fragment ion with mass $m = 45\,\mathrm{u}$ normalized to yield of fragment ion with mass $m = 64\,\mathrm{u}$) of positive secondary ion mass spectra recorded from PEG sample with different monoatomic and cluster ion beams as a function of $\left(\frac{dE}{dx}\right)_e$ and $\left(\frac{dE}{dx}\right)_n$.

5.5. Cluster ions

As pointed out in Chapter 5.4 the use of cluster primary ions in MeV-SIMS has effects on the fragmentation observed in the secondary ion mass spectra. From literature it is known that in keV-SIMS cluster ions enhance molecular secondary ion yields at least linearly with cluster size and for some secondary ions and cluster size ranges even nonlinearly with a scaling closer to n^3 (Guillermier et al. 2006).

To examine the effects of cluster ions on the secondary ion desorption and ionization more closely, the obtained data is broken out and discussed in more detail in the following chapters: At first Chapter 5.5.1 looks at secondary ion yield scaling with electronic stopping power, before Chapter 5.5.2 investigates the fragmentation induced by primary cluster ions.

5.5.1. Secondary ion yield scaling with electronic stopping per cluster constituent: cluster effects in MeV-SIMS

A first indication of the effect of cluster primary ions on secondary ion yields can be obtained by plotting secondary ion yields of select peaks from acquired mass spectra for a range of C_n and Cu_n cluster ions. The data is plotted in Figure 5.19 exemplarily for the full mass protonated molecular peak $m = 175\,u$ from arginine. For the measurements employing C_n (Figure 5.19, left) a significant increase of secondary ion yield with electronic stopping is observed as expected. Therefore, larger cluster sizes n at similar cluster primary ion energies lead to correspondingly increased yields. This means that the energy deposited in the sample by the simultaneous electronic stopping of several constituent atoms of a single cluster ion collectively leads to a higher emission and ionization yield. This is especially impressive in the case of the C_{60} cluster ion, which produces orders of magnitude increased secondary ion yields when compared to monoatomic primary ions at comparable primary ion energies.

The Cu_n data (Figure 5.19, right) shows a slightly different behaviour with an almost step-like increase of secondary ion yields at a certain electronic stopping power. This threshold shows a dependency on the primary ion cluster size n with a higher threshold for larger

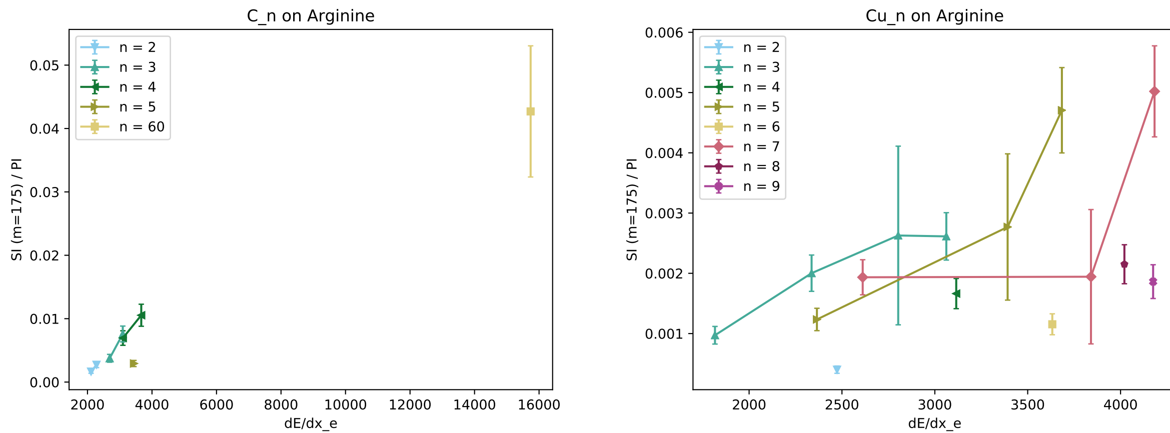

Figure 5.19.: Secondary ion yield of full mass protonated molecular ion with mass $m = 175\,\mathrm{u}$ measured from arginine sample with primary cluster ion beams C_n (left) and Cu_n (right) of varying size n as a function of $\left(\frac{dE}{dx}\right)_e$.

clusters.

If the simple assumption is made that a single impact by a cluster ion of size n with electronic stopping of $\left(\frac{dE}{dx}\right)_e$ is equivalent to the collective impact of n ions each with an electronic stopping power of $\left(\frac{dE}{dx}\right)_e / n$, one would expect a direct linear scaling of secondary ion yield with cluster size (when accounting for the differences in electronic stopping for the different primary ion energies). To investigate whether the yield scaling is actually linear with cluster size n or whether there are nonlinear effects enhancing secondary ion yields from cluster ion impacts - the so called ¨cluster effects¨, one can normalize the secondary ion yields to the cluster size n and thus calculate the secondary ion yield per cluster constituent. Such effects have been observed in keV-SIMS by Guillermier et al. (2006). In Figure 5.20, the normalized yields are plotted for the molecular ion with mass $m = 175\,\mathrm{u}$ from arginine (top) against the electronic stopping power per cluster constituent $\left(\frac{dE}{dx}\right)_e / n$.

For all three sample materials the same general trend can be observed: With increasing cluster size n, the secondary ion yield of both the fragment and molecular secondary ions increases already at significantly lower electronic stopping power per constituent.

For the C_n cluster primary ions (Figure 5.20, left), the secondary ion yields per cluster constituent are significantly higher than for monoatomic primary ions ($n = 1$) at a comparable

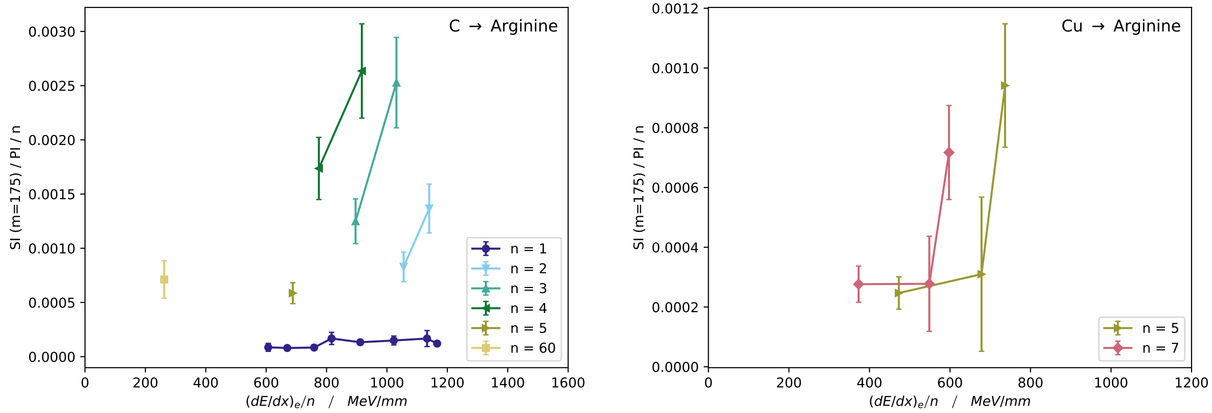

Figure 5.20.: Secondary ion yield of full mass protonated molecular ion ($m = 175$ u) measured from arginine sample normalized to cluster size n with primary cluster ion beams Cu_n and C_n (bottom) as a function of $\left(\frac{dE}{dx}\right)_e / n$.

electronic stopping per constituent $\left(\frac{dE}{dx}\right)_e / n$. This indicates the presence of a non-linear ¨cluster effect¨ in MeV-SIMS and is demonstrated in Figure 5.21, where the secondary ion yield per constituent from C_n primary ions is normalized to the secondary ion yield from monoatomic C primary ions at comparable electronic stopping power. The data are plotted as a function of cluster size n and for the normalization the mean secondary ion yield of measurements with monoatomic C primary ions with electronic stopping powers in the range $600\,\mathrm{MeV\,mm^{-1}} < \left(\frac{dE}{dx}\right)_e < 1200\,\mathrm{MeV\,mm^{-1}}$ was used. In this electronic stopping power range the secondary ion yield from monoatomic C primary ions changes only slightly, therefore this is a reasonable quantity for comparison. Additionally, the individual measurement points are annotated with their respective electronic stopping power per constituent $\left(\frac{dE}{dx}\right)_e / n$ / MeV mm^{-1}. It is immediately noticeable that higher electronic stopping power results also in higher secondary ion yields for a constant cluster size n. The magnitude of this cluster enhancement effect is dependent on cluster size n itself, with the biggest secondary ion yield enhancement of up to a factor 25× seen for cluster sizes $n < 5$, while the large C_{60} primary ions induce a smaller but still significant yield enhancement by roughly one order of magnitude over the monoatomic primary C ions. However, it has to be noted that the C_{60} cluster constituents have an electronic stopping power per constituent of only $\left(\frac{dE}{dx}\right)_e / n = 262\,\mathrm{MeV\,mm^{-1}}$, such that they fall outside the used normalization range. This could lead to

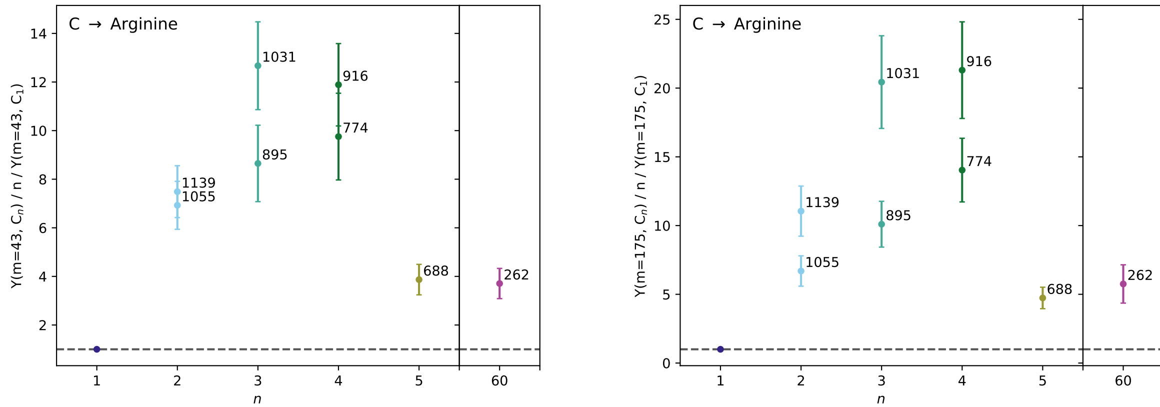

Figure 5.21.: Secondary ion yield per constituent $Y(m = 43\,\text{u}, C_n)$ normalized to the secondary ion yield induced by a monoatomic ion $Y(m = 43\,\text{u}, C_1)$ at comparable electronic stopping power (averaged over the range $600\,\text{MeV}\,\text{mm}^{-1} < \left(\frac{dE}{dx}\right)_e < 1200\,\text{MeV}\,\text{mm}^{-1}$) as a function of cluster size n for the fragment ion $m = 43\,\text{u}$ and full mass protonated molecular ion $m = 175\,\text{u}$ measured from arginine sample. The individual measurement points are annotated with their respective electronic stopping per constituent $\left(\frac{dE}{dx}\right)_e$ / n / MeV mm^{-1}.

a slight underestimation of the cluster effect enhancement factor determined for C_{60} primary ions.

Data acquired with the much heavier Cu_n primary ions (Figure 5.20, right) shows a slightly different behaviour with the step-like increase in secondary ion yield at a specific electronic stopping threshold as observed before. However when normalizing both the yield and stopping power per constituent, this threshold is now actually lower for larger Cu_n cluster primary ions. This indicates that a corresponding cluster effect is also present for the heavier Cu_n clusters.

5.5.2. Fragmentation induced by primary cluster ions

The fragmentation induced by primary cluster ions can be studied by looking once again at the yield ratios of select specific fragment ions and corresponding larger fragments or even the molecular secondary ion. This data is plotted for the three different sample materials analysed in Figures 5.22 (arginine), 5.24 (leu-enkephalin) and 5.25 (PEG) against the electronic stopping power per cluster constituent. Each measurement point is labelled with the primary ion cluster size to make the distinction clearer.

It has been observed that the fragmentation of arginine increases with the ratio of nuclear stopping to electronic stopping (Jones 2012): This behaviour is also observed in the Cu_n data presented here for both the $m = 43\,\mathrm{u}$ and $m = 70\,\mathrm{u}$ fragment ions if their yield is normalized to the molecular protonated arginine ion with $m = 175\,\mathrm{u}$. In general, larger cluster ions induce significantly less fragmentation at comparable electronic energy loss per cluster constituent than monoatomic primary ions. Additionally, the steepness of the fragmentation increases with decreasing electronic stopping power decreases with primary ion cluster size n. The same effects are also observed for the C_n data on arginine, although here the fragmentation varies much less with electronic stopping per cluster constituent. This can be explained by the almost constant ratio of nuclear to electronic stopping power over the stopping power range investigated for ^{12}C. However the fragmentation observed again decreases clearly with increasing cluster size. This is demonstrated in Figure 5.23, where the fragmentation ratios for measurements with an electronic stopping power per constituent in the range $600\,\mathrm{MeV\,mm^{-1}} < \left(\frac{dE}{dx}\right)_e < 1200\,\mathrm{MeV\,mm^{-1}}$ (with the exception of C_{60}) are plotted as a function of cluster size n. In particular the fragmentation from C_{60} primary cluster ions is reduced by up to a factor of $5\times$. Since the electronic stopping per constituent of C_{60} is much lower than the selected range, this rather underestimates the magnitude of the observed cluster effect. Similar to the cluster effect for secondary ion yield enhancement, the fragmentation reduction effect exhibits saturation for larger cluster ions.

When looking at the data from the leu-enkephalin sample a slightly different behaviour

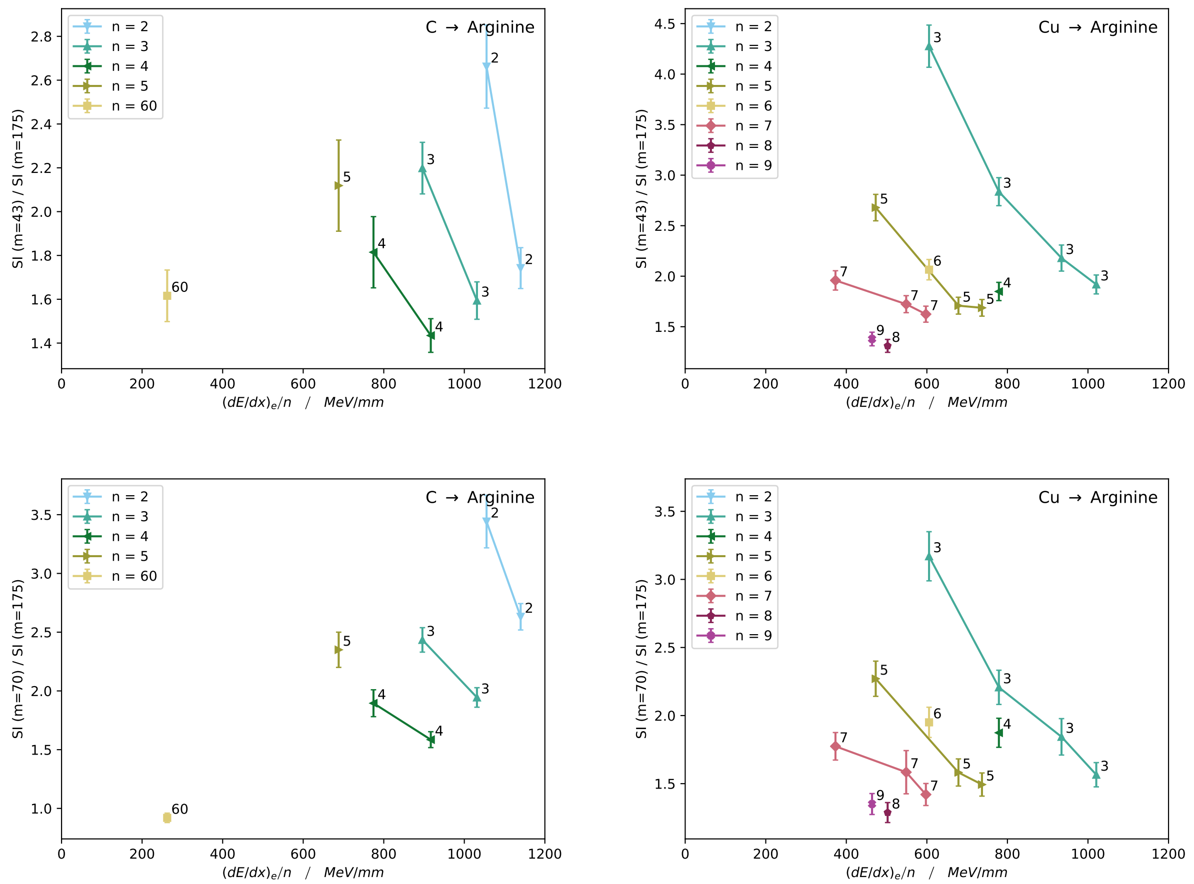

Figure 5.22.: Fragmentation of secondary ions from arginine for fragment ion mass peaks $m = 43\,\text{u}$ (top) and $m = 70\,\text{u}$ (bottom) normalized to the full molecular mass peak of $m = 175\,\text{u}$ for primary cluster ion beams C_n (left) and Cu_n (right) and plotted as a function of $\left(\frac{dE}{dx}\right)_e / n$.

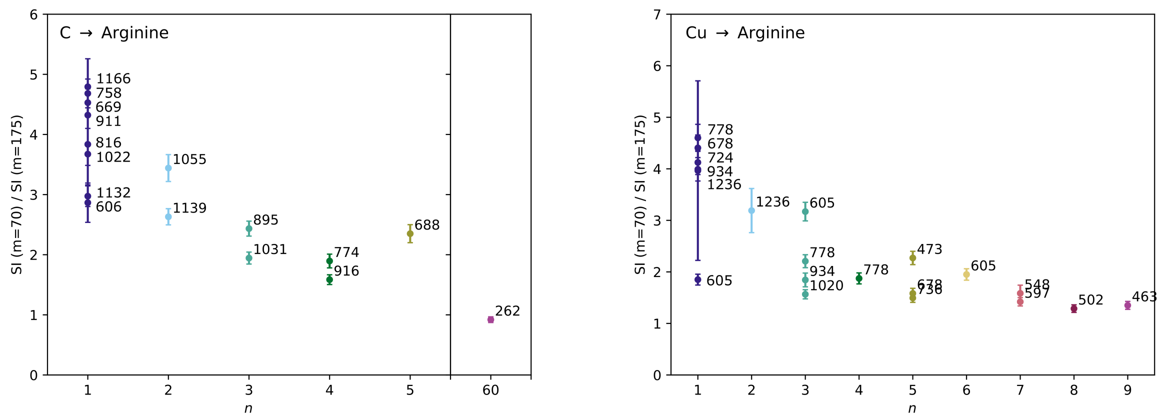

Figure 5.23.: Fragmentation of secondary ions from arginine for fragment ion mass peak $m = 70\,\mathrm{u}$ normalized to the full molecular mass peak of $m = 175\,\mathrm{u}$ for primary cluster ion beams C_n (left) and Cu_n (right) and plotted as a function of cluster size n. Shown are measurements with electronic stopping power per constituent in the range $600\,\mathrm{MeV\,mm^{-1}} < \left(\frac{dE}{dx}\right)_e < 1200\,\mathrm{MeV\,mm^{-1}}$ (with the exception of C_{60}). The individual measurement points are annotated with their respective electronic stopping per constituent $\left(\frac{dE}{dx}\right)_e$ / n / $\mathrm{MeV\,mm^{-1}}$.

emerges: Fragmentation as measured by the yield of the $m = 57\,\mathrm{u}$ fragment ion normalized to the $m = 86\,\mathrm{u}$ fragment ion seems to slightly increase with electronic stopping per cluster constituent though the observed effect is small and barely significant. Larger clusters still seem to induce a lower amount of fragmentation than the monoatomic primary ion, although the effect is relatively weak especially for the smaller C_n and Cu_n primary cluster ions. However, the fragmentation induced by the C_{60} cluster ions is significantly reduced in comparison to the smaller C_n cluster ions. This change in fragmentation behaviour is most likely due to a different mechanism for formation of the specific secondary ion fragments.

Finally, for the PEG data we observe another behaviour: The relative intensity of the $m = 45\,\mathrm{u}$ repeat unit fragment normalized to the $m = 64\,\mathrm{u}$ fragment increases monotonically with electronic stopping power per cluster constituent. It also clearly increases with increasing primary ion cluster size at the same electronic stopping power per cluster constituent. This is demonstrated by plotting the fragmentation ratios for measurements with an electronic stopping power per constituent in the range $600\,\mathrm{MeV\,mm^{-1}} < \left(\frac{dE}{dx}\right)_e < 1200\,\mathrm{MeV\,mm^{-1}}$ (with the exception of C_{60}) as a function of cluster size n in Figure 5.26. The same behaviour

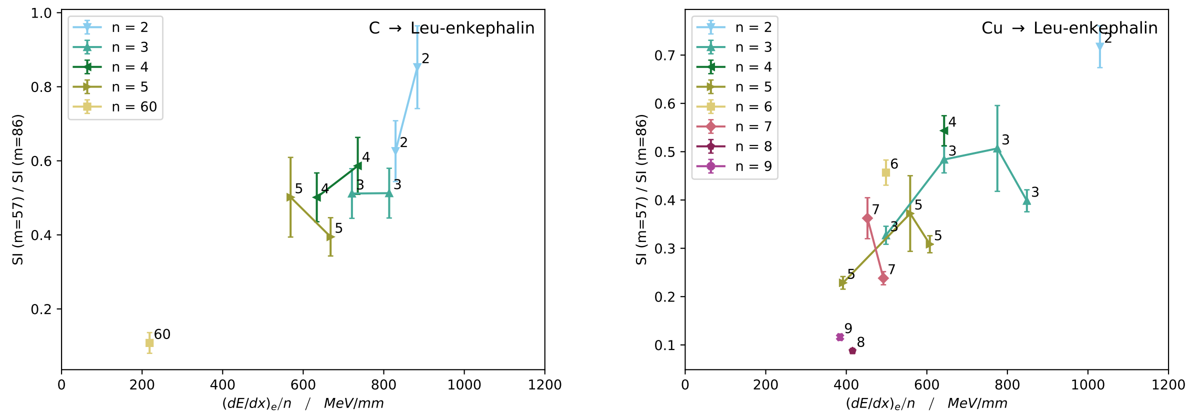

Figure 5.24.: Fragmentation of secondary ions from leu-enkephalin for fragment ion mass peak $m = 57\,\mathrm{u}$ normalized to $m = 86\,\mathrm{u}$ for primary cluster ion beams C_n (left) and Cu_n (right) and plotted as a function of $\left(\frac{dE}{dx}\right)_e / n$.

is observed in the C_n cluster data, although here the effect is weaker and similar relative intensities are measured from all C_n primary cluster ions up to C_{60} primary cluster ions (with a large uncertainty).

This behaviour indicates distinctly different desorption and ionization mechanisms for secondary ions in the case of primary cluster ions impacts: Fragmentation of molecular ions like arginine is significantly reduced. It could be the result of a larger ultratrack region form which larger secondary ions are sputtered relative to the infratrack region to which smaller fragment ions can be attributed. The collective simultaneous impact of all cluster constituents and their collective energy deposition within a very small volume at the sample surface likely lead to a higher δ-electron density when compared to the impact of a single projectile ion. A saturation effect as observed for very large clusters is likely due to an excess in stopping power density within the infratrack as well as in the inner regions of the ultratrack limiting any further molecular yield enhancement.

Meanwhile the behaviour of different fragment and sub-fragment ion yields (as observed from leu-enkephalin and PEG) seems to depend on the specific formation mechanism. In these cases, fragmentation is reduced for larger primary cluster ions. However, due to the comparison of different fragment ions (and not the full-mass molecular ion), this effect is

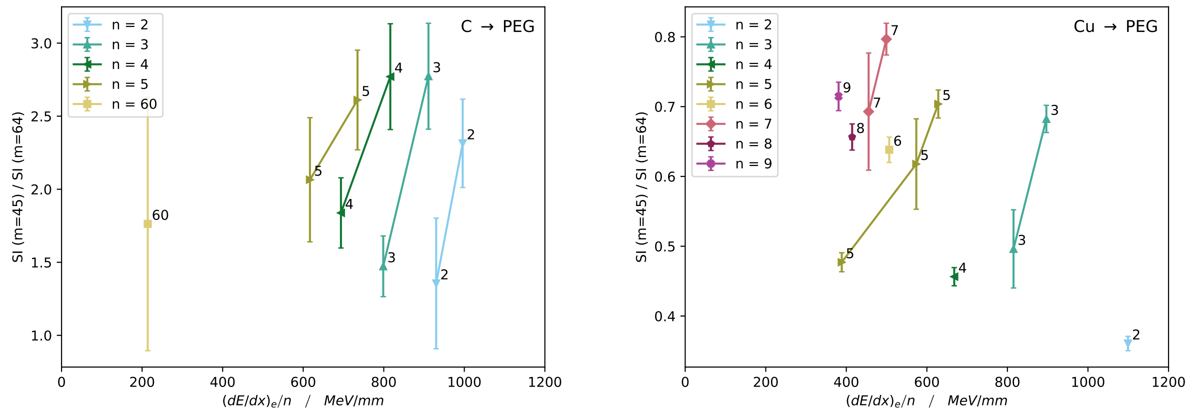

Figure 5.25.: Fragmentation of secondary ion mass spectra from PEG for fragment ion mass peaks $m = 45\,\mathrm{u}$ normalized to $m = 64\,\mathrm{u}$ for primary cluster ion beams C_n (left) and Cu_n (right) and plotted as a function of $\left(\frac{dE}{dx}\right)_e / \, n$.

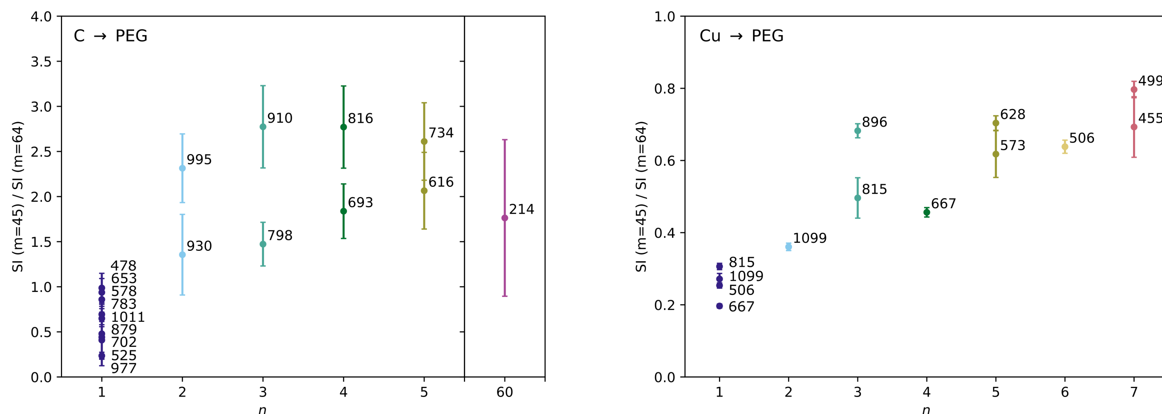

Figure 5.26.: Fragmentation of secondary ions from PEG for fragment ion mass peak $m = 45\,\mathrm{u}$ normalized to $m = 64\,\mathrm{u}$ for primary cluster ion beams C_n (left) and Cu_n (right) and plotted as a function of cluster size n. Shown are measurements with electronic stopping power per constituent in the range $600\,\mathrm{MeV\,mm^{-1}} < \left(\frac{dE}{dx}\right)_e < 1200\,\mathrm{MeV\,mm^{-1}}$ (with the exception of C_{60}). The individual measurement points are annotated with their respective electronic stopping per constituent $\left(\frac{dE}{dx}\right)_e \; / \; n \; / \; \mathrm{MeV\,mm^{-1}}$.

much weaker and the fragmentation reduction manifests only for larger cluster sizes n. For PEG the significant increase of the relative yield of the PEG polymer repeat unit fragment from larger primary cluster impacts could indicate a less selective desorption and ionization: Within a sample made from long polymer chains, larger primary cluster impacts seem to favour the emission of the unaltered representative repeat unit rather than emission of the repeat unit with additionally attached fluorine and hydroxy groups. This effect could also be the result of an excess in stopping power density within the infratrack and the inner ultratrack leading to a highly excited material state which breaks up the polymer in its repeat units while at the same time inhibiting the binding of attachment groups.

6. Dual polarity secondary ion mass spectrometry

The new dual polarity ToF mass spectrometer setup CHIMP described in Section 3.4 uniquely enables the simultaneous study and comparison of negative and positive secondary ion yields and secondary electrons emitted from samples under bombardment with primary ions in MeV-SIMS. The simultaneous acquisition of all three detector channels ensures direct comparability of the data since all secondary particles are emitted under the same sputtering conditions, allowing for conclusions about the underlying desorption and especially ionization processes.

These features will be described in the following subchapters, with Section 6.1 introducing the two different sample materials investigated and their spectra. In Section 6.2 the offline event correlation analysis provides some insights into the characteristics of simultaneous emission of multiple secondary ions from a single primary ion impact. In Section 6.3, specific peak yields for corresponding positive and negative ion pairs occurring in the spectra will be compared, an analysis that is only accessible by a bipolar spectrometer.

6.1. Accessing all the ions from two different samples

Although the modified setup was only fully commissioned and put into operation at the beginning of 2020, a set of measurements with small C_n cluster primary ions on two different samples were performed: One is once again an arginine spin-coated Si-wafer, while for the second sample NaCl was deposited on a clean Si-wafer by evaporative coating. The positive and negative secondary mass spectra acquired from both samples using a primary C_6 cluster ion beam with an energy of 7 MeV are shown in Figures 6.1 (Arginine) and 6.2 (NaCl).

For the positive arginine spectrum the same fragmentation peaks as listed in Table 5.1

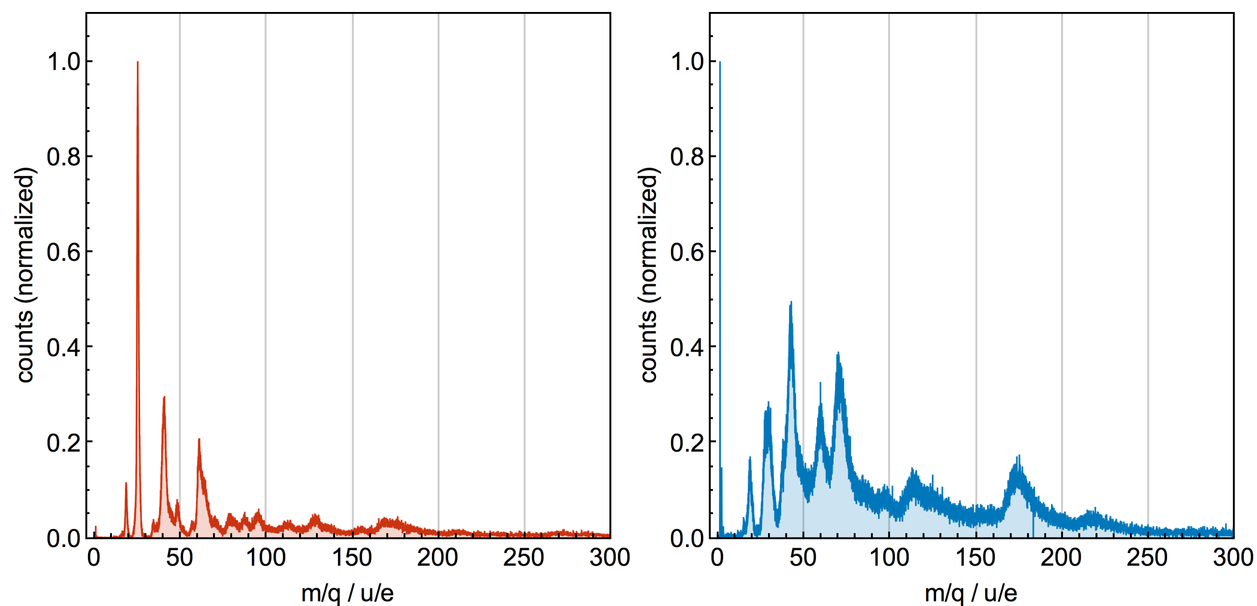

Figure 6.1.: Negative (left) and positive (right) spectra of Arginine sample using 7 MeV C_6 primary cluster ions.

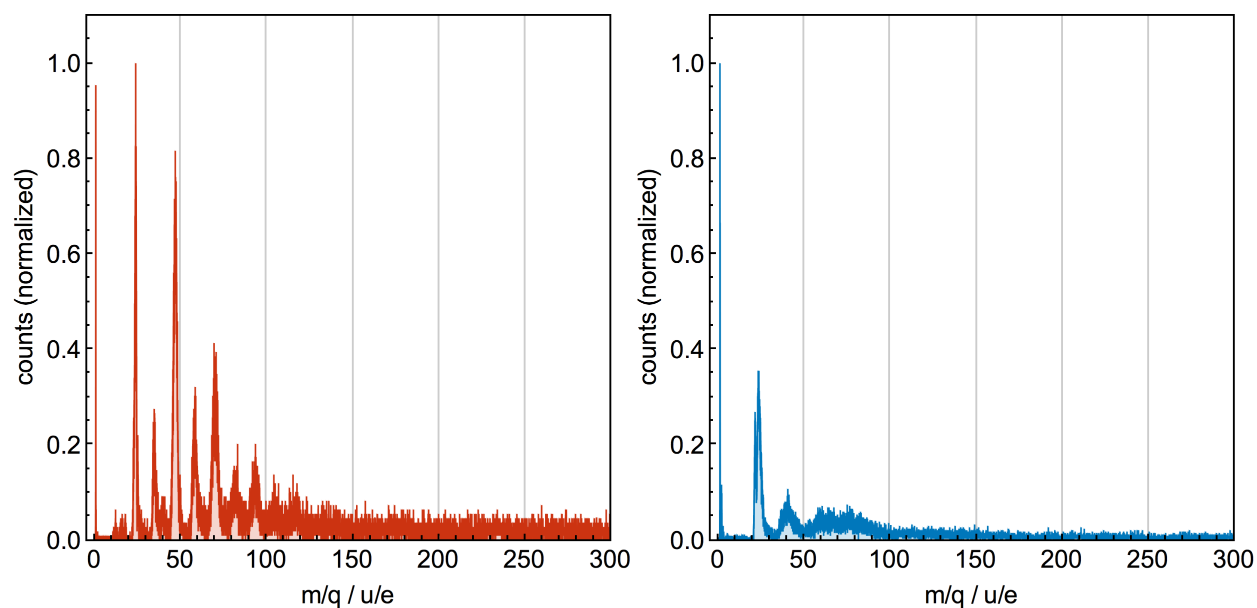

Figure 6.2.: Negative (left) and positive (right) spectra of NaCl using 7 MeV C_6 primary cluster ions.

are observed, while in the negative spectrum the most significant peaks occur at masses $m = 26\,\text{u}, 41\,\text{u}, 60\,\text{u}$. The peaks corresponding to full molecular Arginine secondary ions can be observed in the positive and negative polarity mass spectra at masses $m = 175\,\text{u}$ (pToF) and $m = 173\,\text{u}$ (nToF) respectively.

In case of the NaCl sample it is actually the negative spectrum that is more feature-rich: Here a series of peaks at masses $m = 23\,\text{u}, 34\,\text{u}, 46\,\text{u}, 58\,\text{u}, 70\,\text{u}, 81\,\text{u}, 94\,\text{u}$ is observed, of which only the first one can be attributed clearly to the Na^- ion. In the positive spectrum apart from the intense Na^+ peak at mass $m = 23\,\text{u}$, only one second peak at mass $m = 40\,\text{u}$ can be resolved, which could potentially be attributed to the $HNaO^+$ ion.

6.2. Event correlation analysis: simultaneous emission of multiple ions

The list-file recording of all detected events allows for offline analysis of event correlations within and across the single detector channels. This provides a unique tool to study collective emission of not only ions of the same polarity but also of ions with opposite polarity from a single primary ion impact. To investigate the influence of cluster size on the simultaneous emission of several secondary ions from a single primary ion impact and potential differences between negative and positive secondary ion emission, the distribution of multi-stop events (i.e. start signals that are correlated with more than one single stop event in the corresponding ToF stop detector) in the measured spectra was analysed.

In Figure 6.3, the relative frequency of multi-stop events is plotted as a function of multiplicity $M = \frac{\#Stops}{Start}$ of the correlated stops for both positive and negative spectra acquired from Arginine with primary monomer and cluster ions beams of C_1, C_2, C_4 and C_6. Independent of cluster size we can observe that the relative frequency of detection of multi-stop events decreases much faster with increasing multiplicity for negative secondary ions than for positive secondary ions. For both polarities the use of larger primary clusters significantly

shifts the emission characteristics towards multiple secondary ions per primary ion impact. The relative frequency at which such multi-stop events are detected is increasing by several orders of magnitude. At the same time the fraction of start events for which only a single stop is detected decreases from $>90\,\%$ to $\approx 40\,\%$ when moving from C_1 to C_6 primary ions.

Furthermore, the distribution of multi-stop frequency with multiplicity M shifts from a roughly exponentially decreasing dependency ($\propto \exp(-M)$, appearing as a straight line in the linear-logarithmic plots) towards a more poisson-like dependency on increasing cluster size.

The behaviour observed from the inorganic NaCl sample is different in this regard, as the plots of the corresponding multi-stop frequencies for positive and negative secondary ions in Figure 6.4 show: The distribution of multi-stop frequency with multiplicity M remains exponentially decreasing ($\propto \exp(-M)$, straight line) even for the largest primary cluster ions used. Still, the other two observed effects are also apparent: Larger primary ions lead to a significantly enhanced emission of multiple secondary ions from a single primary ion impact (although for negative ions desorbed form NaCl, the effect of cluster size seems to be strongly reduced when compared to the behaviour observed on the Arginine sample). In general the emission of several negative secondary ions occurs much more rarely than this is the case for positive secondary ions. This can be expected, since with high enough energies positive secondary ions can be formed from basically all particles, while this is not necessarily the case for the formation of negative secondary ions.

Finally, we can compare the relative frequency of multi-stop events for negative and positive secondary ions detected from both samples. The data for a primary ion beam of C_6 clusters at 7 MeV is shown in Figure 6.5. The different dependency of relative frequency on multiplicity becomes apparent when comparing the two figures. Additionally, one now notices that multi-stop events for negative ions are much rarer than for positive ions. This difference is much more pronounced in case of the inorganic NaCl sample than for the Arginine sample. Potentially the larger and intramolecularly weaker bound arginine molecules enables the ejection of several secondary ions from a single primary ion impact for both polarities, while

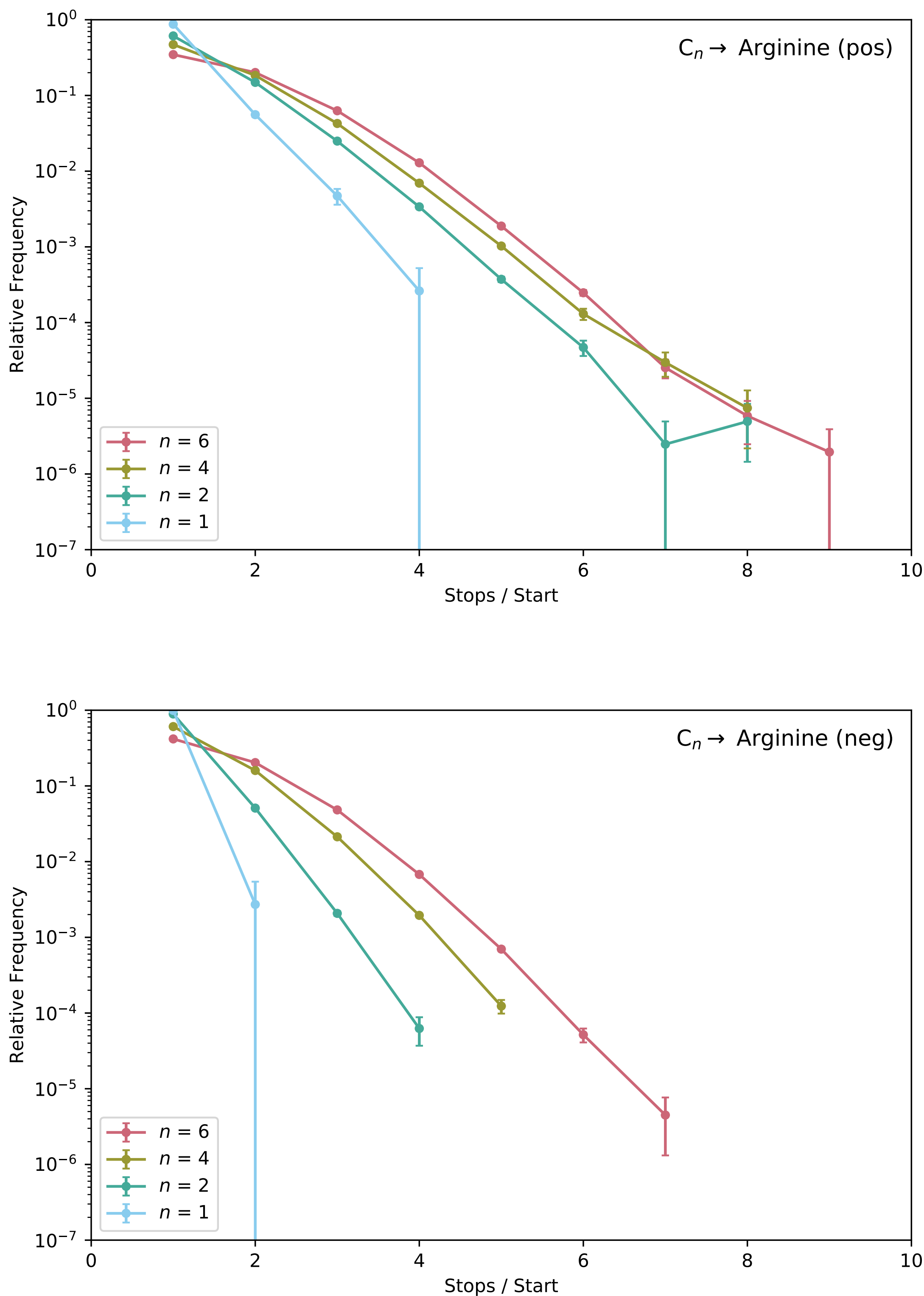

Figure 6.3.: Relative frequency of positive (top) and negative (bottom) multistopevents recorded from arginine sample with 7 MeV C_n primary ion beams with varying C_n ion cluster size.

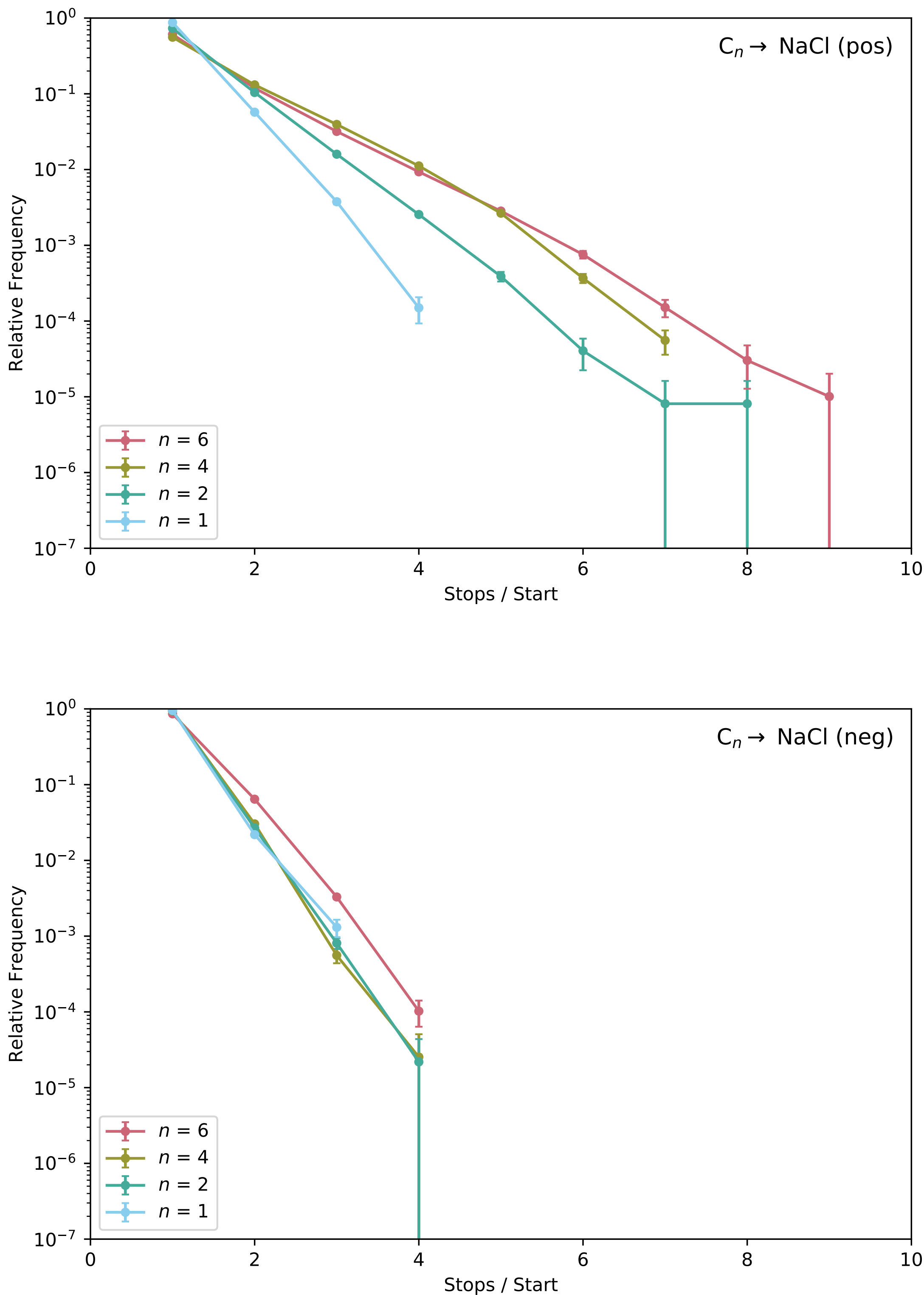

Figure 6.4.: Relative frequency of positive (top) and negative (bottom) multistopevents recorded from NaCl sample with 7 MeV C_n primary ion beams with varying C_n ion cluster size.

the crystalline structure of NaCl leads to a higher relative frequency of coincident emission of more than 4 positive ions but at the same time inhibits the coincident emission of negative ions severely.

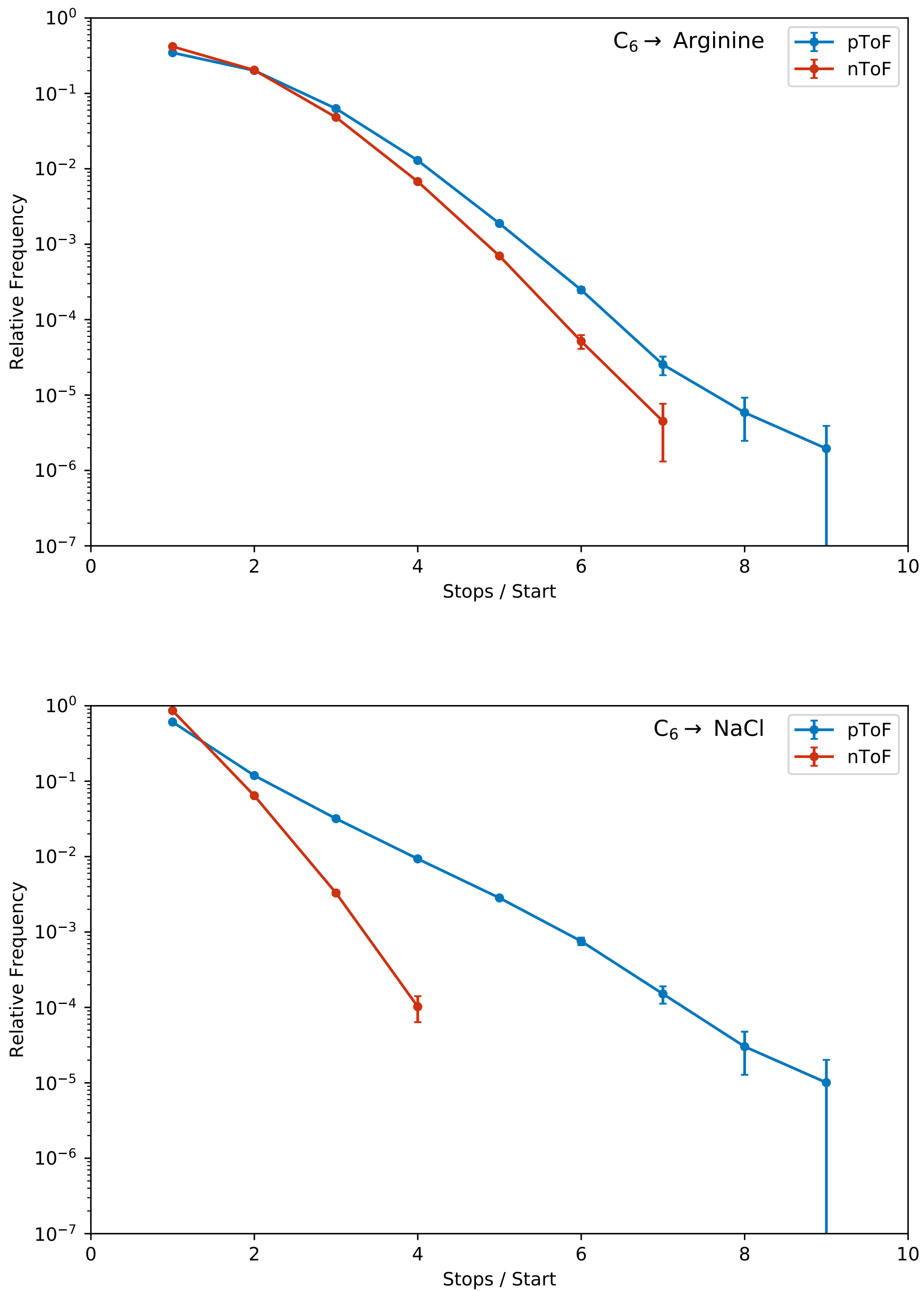

Figure 6.5.: Relative frequency of multistopevents recorded from arginine (top) and NaCl (bottom) samples with a 7 MeV C_6 primary ion beam for negative (red) and positive (blue) secondary ions.

6.3. Positive and negative secondary ion yields

To study the influence of primary ion cluster size on the ratio of negative and positive secondary ions desorbed from the sample surface, a few corresponding pairs of negative and positive ions have been selected: For the Arginine sample spectra, the first peak pair are the mass peaks at masses $m = 43\,\mathrm{u}$ (positive) and $m = 41\,\mathrm{u}$ (negative), corresponding to the negative and positive ions of the arginine fragments C_2H_3N respectively CH_3N_2 (due to the limited mass resolution both of these peaks and those of the neighbouring fragments CH_2N_2 and CH_4N_2 cannot be resolved and are all integrated together). As a second peak pair the mass peaks corresponding to the full molecular arginine molecule at masses $m = 175\,\mathrm{u}$ (positive, $(M + H)^+$) and $m = 173\,\mathrm{u}$ (negative, $(M - H)^-$) were selected. For the NaCl sample spectra, only the corresponding mass peaks at the common mass of $m = 23\,\mathrm{u}$ (Na^+ resp. Na^- ions) were considered, since no unambiguous identification and correspondence of additional mass peaks could be done.

The peak yields of these fragment ions were determined as described in appendix C and are plotted as a function of primary C_n ion cluster size n in Figures 6.6 (Arginine) and 6.7 (NaCl). Additionally in the lower panel of each plot the ratio of the corresponding positive and negative ion peak yield is plotted.

All three corresponding ion pairs show the same overall behaviour: For monomer C primary ions positive secondary ion yields are significantly higher compared to their corresponding negative secondary ions. However, the ratio of positive and negative secondary ion yields approaches values close to parity with increasing size n of the primary C_n ion clusters.

This indicates a considerable change in the ionization process of secondary ion desorption when employing primary cluster ions. This effect occurs for both fragment and full mass molecular ions. Therefore it is not directly influenced by or connected to the effect of reduced fragmentation observed with using primary cluster ions.

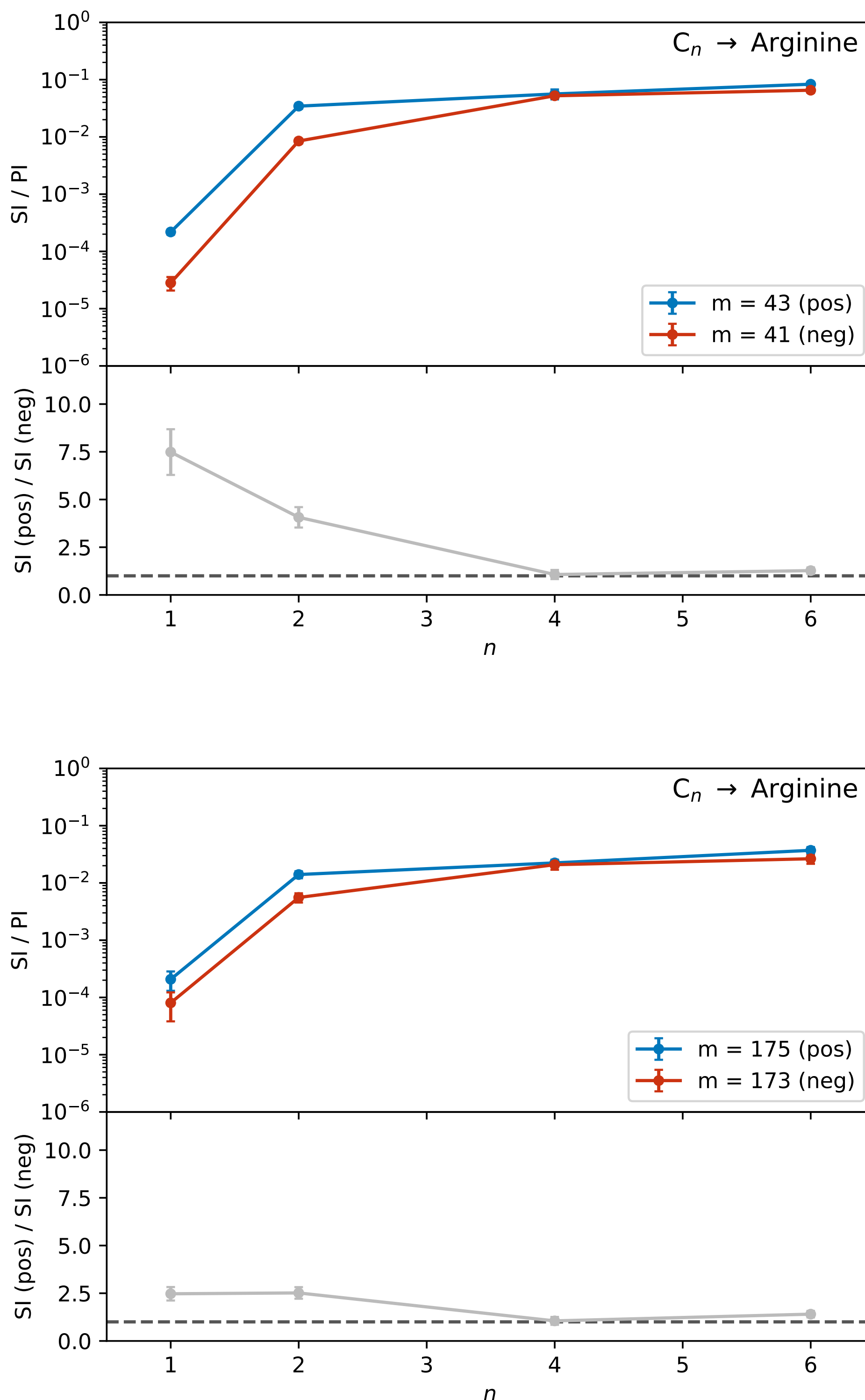

Figure 6.6.: Positive and negative peak yields for secondary ions of masses $m = 43\,\mathrm{u}$ / $m = 41\,\mathrm{u}$ (top) respectively $m = 175\,\mathrm{u}$ / $m = 173\,\mathrm{u}$ (bottom) sputtered from arginine and their yield ratio as a function of primary C_n ion cluster size.

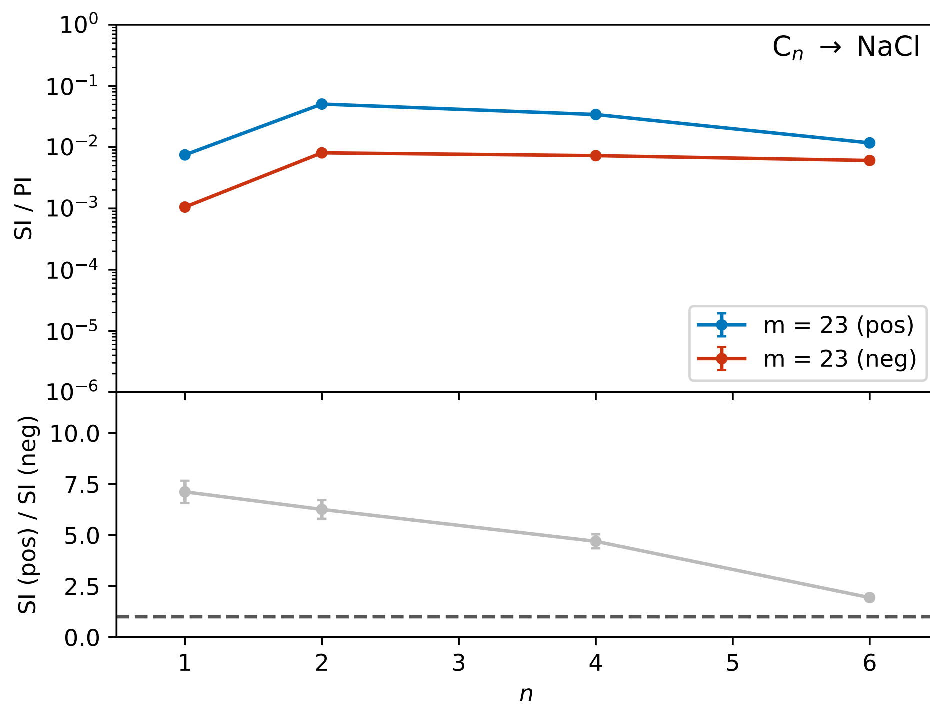

Figure 6.7.: Positive and negative peak yields for secondary ions of masses $m = 23\,\mathrm{u}$ / $m = 23\,\mathrm{u}$ sputtered from NaCl and their yield ratio as a function of primary C_n ion cluster size.

7. Summary and conclusion

Within the present work both new technical approaches to study secondary ion emission in MeV-SIMS have been developed and a comprehensive set of secondary ion yield measurements has been performed to provide the basis for an improved understanding of the underlying desorption and ionization processes.

Besides continuous technical improvements to the existing CHIMP setup at ETH Zurich, the potential of capillary collimation for MeV-SIMS molecular imaging could be demonstrated. Independent of primary ion mass and energy a collimation down to beam sizes on the order of a single µm is possible, resulting in primary ion particle currents in the p fA range. Due to the extremely high efficiency of the technique this consequently enables micrometer-resolution molecular imaging in the static SIMS regime.

The unique setup at the TANDEM accelerator facility was used to collect secondary ion yield data over a wide range of energetic primary ions including cluster ions for the three organic sample materials arginine, leu-enkephalin and PEG. Additionally the samples were also used in a round-robin comparison study coordinated by the IAEA in which secondary ion yields were determined and the conditions for static SIMS could be confirmed. The resulting dataset explores a wide parameter space of electronic and nuclear stopping power of the primary projectile ion as well as a range of primary ion cluster sizes consisting of light and heavier consitutents. Analysis of the data indicates a significant yield increase above a certain threshold velocity of the projectile ion which is accompanied by a promotion of simultaneous emission of several secondary ions per impact. As both nuclear and electronic branches could be identified in the yield data it could be demonstrated that this effect is likely connected to increased electronic sputtering activated by generated δ-electrons exceeding a certain velocity threshold. At higher velocities the secondary ion yields level off. This indicates a possible saturation of the highly excited matter state in the infratrack that is no longer compensated

by an increase in ultratrack size due to an insufficient δ-electron density. In any case, the secondary ion yield data shows a complex scaling behaviour and cannot be described by a simple power-law scaling with electronic stopping power over a large range as proposed by many theoretical models.

The yields of large molecular ions increase much faster with electronic stopping than the ones of their corresponding fragment ions, resulting in a significant reduction of fragmentation in the secondary ion mass spectra. Both, decreased nuclear stopping and increased electronic stopping, contribute to this reduction in fragmentation. However, the dependencies of both cannot be completely decoupled. This supports the model of increased fragmentation originating from the infratrack region, while larger molecular ions are predominantly sputtered from an outer ultratrack region, which is activated through electronic sputtering by secondary δ-electrons. While bonds in the ultratrack region are softened by ionization and electronic excitation, the actual emission of large particles from this zone could still be fostered by atomic motion originating from the inner or deeper parts of the ion track.

The use of cluster primary ions significantly reduces the occurring fragmentation compared to monoatomic projectile species at comparable stopping power characteristics. For sample materials consisting of long polymer chains, cluster primary ions promote the desorption of polymer repeat groups. Both of these effects could be explained by an enhanced δ-electron density in the sample due to the collective energy deposition of the cluster constituents. The ratio of nuclear to electronic stopping is also larger for a cluster ion than for its corresponding monoatomic ion at the same electronic energy loss due to its lower velocity, which leads to an increase in overall atomic motion. Additionally, the cluster effects known from keV-SIMS could also be observed in MeV-SIMS, resulting in a non-linear yield increase with primary ion cluster size. The magnitude of these cluster effects levels off with increasing projectile cluster size, indicating a saturation effect in the excitation state of the sample material within the infra- and ultratrack zones.

In a second step, the CHIMP setup was upgraded to a simultaneous dual polarity MeV-SIMS instrument featuring electron start with the unique capability to detect secondary electrons,

secondary negative as well as positive ions emitted from the sample. The instrument was not designed to achieve high mass resolution but rather as a tool to enable the study of the underlying desorption and ionization processes by comparison and correlation of secondary ions of both polarities.

The new setup was successfully put into operation and a first study with small primary C_n cluster ions was performed on organic and inorganic samples. Offline event correlation analysis shows that negative ions are emitted with significantly smaller multiplicity from a single projectile impact than positive ions. Larger primary cluster ions, however, increase the emission multiplicity for both positive and negative secondary ions. They also shift the observed distribution of emission multiplicity on the organic sample used from an exponential decrease towards a poisson distribution.

A direct comparison of simultaneously acquired positive and negative mass spectra reveals that for increasing cluster size the ratio of corresponding emitted positive / negative ion pairs approaches parity. Monomer primary ions strongly favour the emission of the respective positive secondary ion. This yield ratio effect is observed for both fragment and full mass molecular secondary ions, indicating that it is not directly connected to the reduced fragmentation induced by primary cluster ions. The formation of a plasma-like state at the primary ion impact point could be a possible explanation of this dramatic effect.

To conclude, the collected data shines new light on the phenomenological processes involved in the emission of secondary ions in MeV-SIMS by identifying and characterizing some already known effects but also some which have not been observed with energetic heavy monomer and cluster ions before. The upgraded dual polarity setup holds considerable promise to study these effects in more detail and thereby contribute to a more granular picture of secondary ion emission.

8. Outlook

Following the successful installation of the new dual-polarity ToF system the next step is to employ it for in-depth studies of secondary ion desorption and ionization in MeV-SIMS. As already demonstrated, the setup with its separate simultaneous detection capability for secondary electrons, positive as well as negative secondary ions and the ability to perform offline event correlation analysis provides a unique platform to explore secondary ion emission.

In the near future, potential studies could investigate the influence of primary ion charge state on secondary ion yields of both polarities: In past experiments significant charge state dependencies have been reported. By modifying the installed micrometer apertures through application of a thin carbon stripper foil, the equilibrium charge state distribution of the primary ions can be reached before they impact the sample. Similarly direct comparison measurements between a cluster impact and the simultaneous impact of the single monoatomic cluster constituents can be performed by dissociation of the cluster in such a foil before the sample. Additional insights into the ionization processes involved in the generation of corresponding negative and positive ions can be obtained by detailed studies of correlated emission of multiple positive and negative ions form a single projectile impact.

The ability to simultaneously measure positive and negative ion yields should also be used to explore secondary ion yields from a wide range of different sample materials including simple inorganic and even conducting ones. While generally only very low yields have been achieved from these, the use of energetic cluster projectiles and the very high efficiency of MeV-SIMS might be sufficient to overcome this issue. The highly excited material state responsible for ion emission holds the potential to mitigate matrix effects which usually limit the quantitativeness of conventional keV-SIMS analysis.

Although MeV-SIMS with its very high efficiency requires only very low primary ion beam currents for analysis, dynamic MeV-SIMS with cluster ions at higher beam intensities holds

potential for sputter depth profiling. Here it could be again of interest to study the time-evolution of positive and negative secondary ion yields as well as the destruction cross-sections for different sample materials.

Finally, as research and the progress of the technical development within the last years has proven, MeV-SIMS holds a significant potential for applications in a wide range of research fields. The integration with additional simultaneously performed ion beam analytical techniques is easily possible and provides a powerful multi-analysis tool. Although the current setup at ETH Zurich was not developed with the primary goal of pursuing applications, the conversion to a state-of-the art instrument suitable for applied research by installation of a commercially available orthogonal-extraction or bunched mass spectrometer is straightforward. Furthermore, the microcapillary beam collimation approach offers the ability to extract the primary ion beam into air and could be used to install an ambient pressure MeV-SIMS setup.

A. Technical improvements and modifications to the CHIMP setup

The CHIMP setup used for most of the yield and fragmentation measurements and described in Chapter 3.3 features some improvements with respect to the initial setup as existing in 2016 and described in Schulte-Borchers et al. (2016):

- To suppress electrons originating from the beam collimation slits and capillary entrance from reaching the eCT secondary electron detector, additional shielding was installed, including a high voltage biased shielding at the collimator mount.
- The pToF mass spectrometer was optimized by lowering the potential applied to Cone 2 and the ToF liner tube, resulting in particle flight times that are increased by $\sim$15 %. Additionally, the pMCP front voltage was increased such that the arriving secondary ions are accelerated a second time just before they are detected on the pMCP detector. A comparison of the electric potential and field configuration with the initial (left) and modified (right) operating parameters applied is shown in Figure A.1. As demonstrated in Figure 3.6, these modifications increased mass resolution of the pToF spectrometer from $m/\Delta m \approx 45$ to about $m/\Delta m \approx 100$.

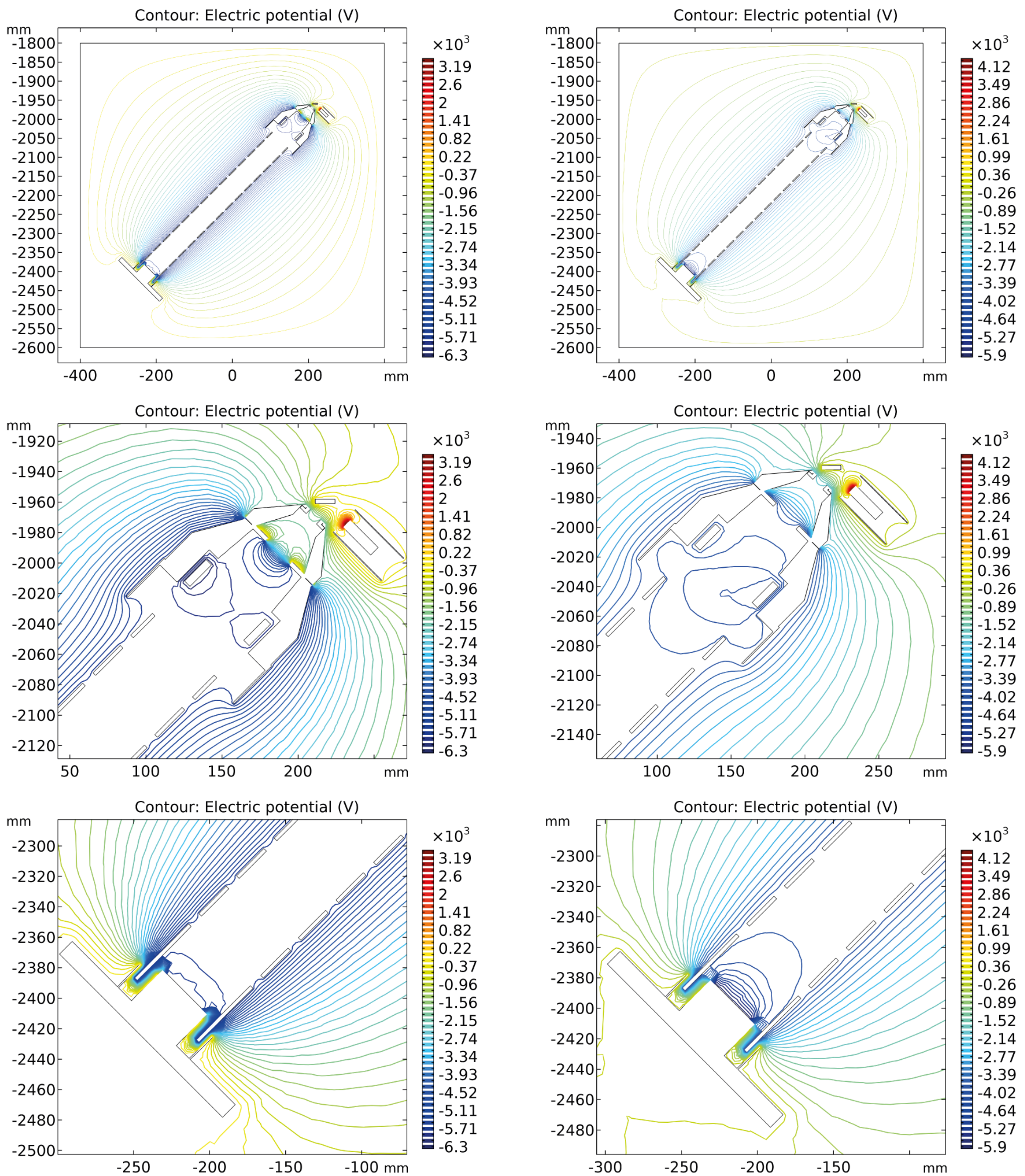

Figure A.1.: Initial (left) and modified (right) electric potential and field configuration of the pToF mass spectrometer.

B. Production and characterization of glass capillaries

To collimate the primary ion beam straight glass capillaries with a preferentially conically shaped tip were used. Since the tip of commercially available capillaries is often bent due to the production process, Simon, Döbeli, et al. (2012) developed a specific procedure to produce straight capillaries with varying geometries. The process consists of two steps: First the tubular straight capillary is pulled to a tapered shape and subsequently the tip is cut to achieve a well-defined capillary outlet of the desired diameter.

Most capillaries were produced from straight capillaries made from borosilicate glass (Science Products GB150-8P). The straight glass tube is then clamped vertically with both ends into a capillary puller machine and heated preferentially in its middle over a limited length by a heating filament. Once the glass softens, the capillary is stretched out due to an electromagnet pulling the two mounted capillary ends apart, resulting in a tapered glass capillary. The capillary geometry can be controlled by careful fine-tuning of the current in the heating filament and the pulling electromagnet, with a lower pulling force and higher heating current leading to shorter capillaries with smaller tapering angle. Too fast heating as well as slight asymmetries in the alignment of the capillary clamps lead to deformed, non-straight capillaries or even prevent that both parts of the capillary separate during the pulling process.

The pulled tapered capillaries are then selected based on their straightness and shape and examined under an optical microscope. Its inner diameter is optically determined as a function of the position along the capillary axis from the tip, yielding the tapering angle profile of the capillary (see Figure B.1).

After the pulling process, most capillaries feature a not well-defined or even closed tip, such that they need to be cut to obtain a capillary outlet with the desired diameter. This

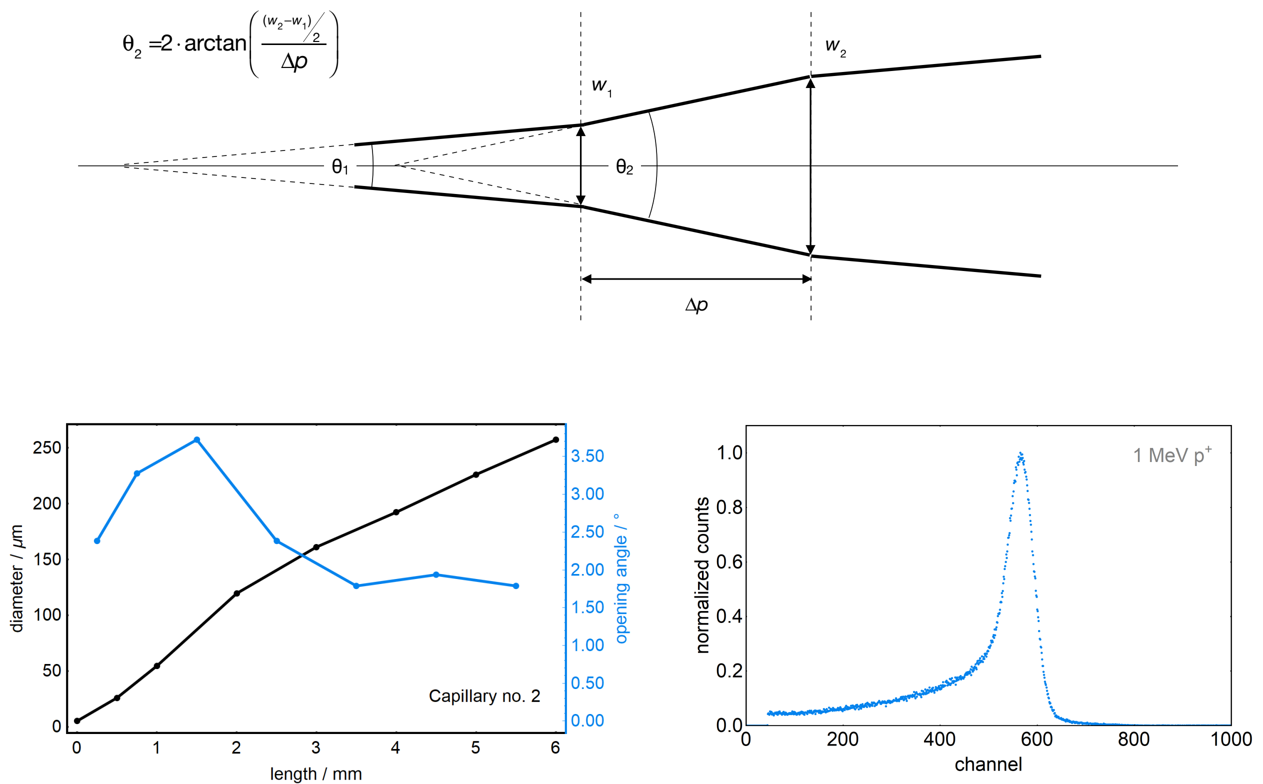

Figure B.1.: Sketch of simplified capillary geometry (top), and measured inner diameter and tapering angle of a self-manufactured straight glass capillary with an outlet diameter of 5.2 µm (bottom left). Additionally the test spectrum of an 1 MeV ion beam transmitted through the capillary into air and measured using a silicon PIN diode detector is shown (bottom right).

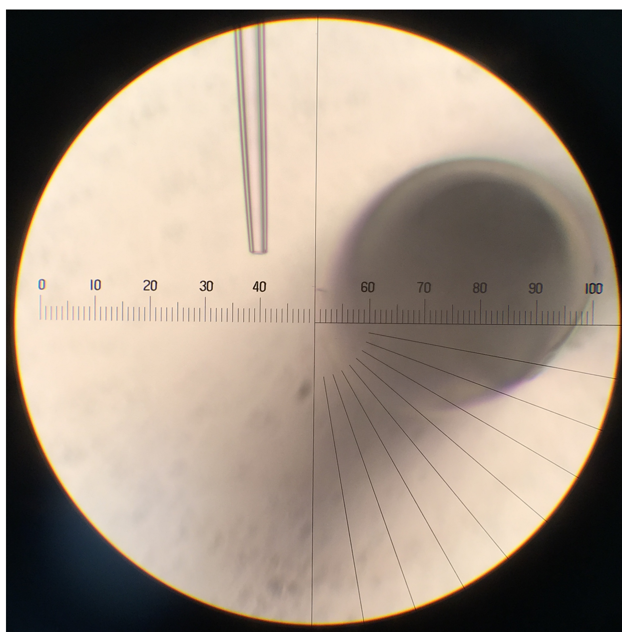

Figure B.2.: Picture taken after the capillary cutting process in the microforge, showing the cut capillary tip (left) as well as the molten fusing glass bead attached to the heating wire (right, out of focus).

cutting is performed using a microforge instrument (Narishige MF-900), which consists of a microscope observing a micromanipulator as well as a heating wire element. The capillary is inserted into the micromanipulator and aligned such that the heating wire with a pre-applied amount of fusing glass powder is close to the cutting point. Subsequently the heating element is switched on, melting the fusing glass powder and creating a molten glass bead that extends during the heating process. The capillary is then moved towards the molten glass bead. Once the fusing glass bead attaches to the outside of the glass capillary at the cutting point, the heating element is switched off again and the contracting fusing glass bead breaks of the capillary tip at the contact point (see Figure B.2). By adjusting the heating temperature and duration, the melting or softening of the capillary tip itself and possible deformations can be avoided.

Finally, before installation of the capillaries into the MeV-SIMS measurement chamber, their transmission and collimation capabilities are tested at a dedicated beam end station. This is done by transmitting an ion beam (usually 1 MeV p^+) from vacuum into air through the capillary and measuring the energy spectrum of the transmitted ion beam using a silicon PIN diode detector. Using the beam end station the capillary position as well as its angle can be adjusted, such the optimal geometrical transmission parameters can be determined. Under optimal conditions the measured energy spectrum should feature a distinct monoenergetic peak featuring only a weak scattering tail extending to lower ion energies. An example spectrum of a good quality capillary with an outlet diameter of 5.2 µm is shown in Figure B.1 (bottom right).

C. Compilation of experimental yield and fragmentation data

C.1. GID interpolation and error estimate

As described in chapter 5.2 the primary ion count rate was measured twice using the transmission GID detector for each MeV-SIMS measurement performed: Once immediately before and once immediately after the spectra acquisition. The measurement was only used for further analysis if the count rates measured were somewhat comparable - and discarded in cases where the beam stabilisation of the accelerator had failed and the count rate was completely lost or similar occurrences. To then determine the total number of primary ions incident during the spectra acquisition, the two measurements of the GID detector count rate were averaged and multiplied with the acquisition time of the secondary ion mass spectrum:

$$N_{PI,mean} = \frac{(R_{GID,start} + R_{GID,stop})}{2} \cdot T_{DAQ} \qquad \text{(C.1)}$$

This straightforward linear interpolation provides quite reliable estimates for the total number of primary ions that hit the target. Over long measurement times any small beam instabilities or current variations cancel out. This was also checked by monitoring the electron Channeltron detector count rate during the measurements: Since secondary electron emission closely correlates with the number of primary ions hitting the target for a given spot and sample material, it can be used to track changes in primary ion count rate. Therefore the changes observed in the secondary electron rate were scaled up to the GID count rates measured before and after the mass spectrum acquisition. The total number of primary ions incident

during spectra acquisition is then estimated as:

$$N_{PI,int} = \int_{t_{start}}^{t_{stop}} R_{GID,int} \mathrm{d}t \tag{C.2}$$

For most measurements analysed, the relative deviation is well below the relative error of 5 % that was assumed for the GID rate measurement. Therefore the use of the simplified linear interpolation given in C.1 is reasonable.

C.2. Mass spectra calibration and peak fitting

Calibration of ToF mass spectra

For mass calibration of the ToF spectra, a number of characteristic mass peaks that are well separated and good candidates for automatic fitting were identified. These peaks in the ToF spectrum were then automatically fitted with a gaussian peak function using the Mathematica NonLinearModelFit function to determine their ToF peak positions. From the resulting calibration points a quadratic mass calibration function specific to the individual ToF spectrum was determined using again the NonLinearModelFit function of Mathematica and applied to obtain a calibrated mass spectrum of the respective measurement. An example of one of these calibration functions for a spectrum acquired from an arginine sample is shown in Figure C.1. For each spectrum the calibration was checked visually for sufficient peak fit quality and a good calibration function fit with reasonable coefficient of determination R^2.

Fitting of individual mass peaks

For the determination of the counts of a specific mass peak within a mass spectrum, for each sample material a number of potentially interesting mass peaks were identified (compare Tables 5.1, 5.2 and 5.3). For each spectrum analysed the corresponding mass peaks were automatically fitted on top of a constant background with an exponentially modified gaussian peak function in one of the following equivalent representations:

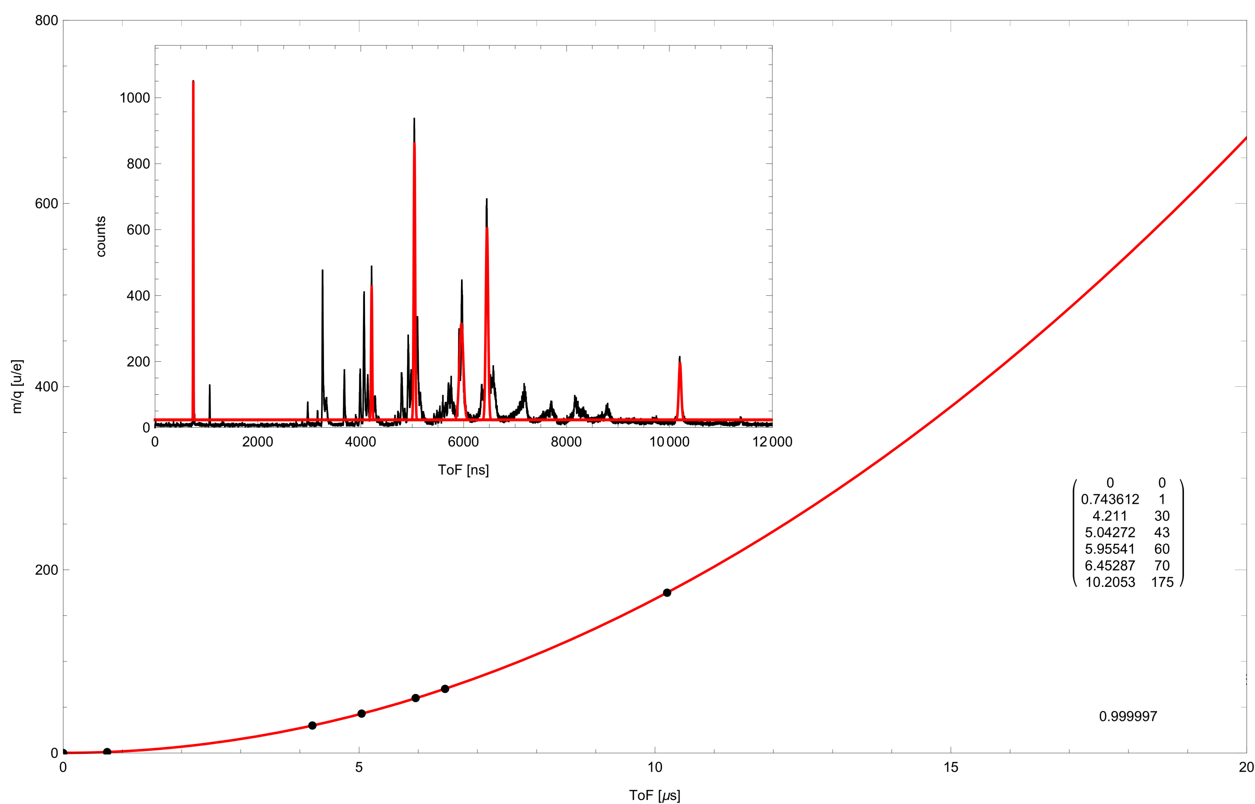

Figure C.1.: Calibration plot of example spectra acquired from an arginine sample. Inset is the ToF spectrum with fitted gaussian peaks for the position determination (top left) as well as the ToF positions of the fitted mass peaks (right) and the coefficient of determination R^2 of the quadratic calibration function fit.

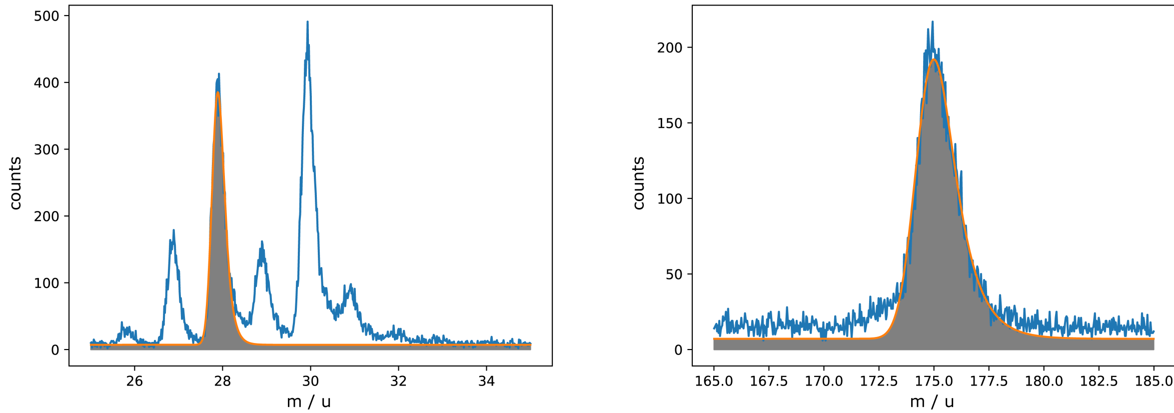

Figure C.2.: Mass peaks $m = 28\,\text{u}$ (left) and $m = 175\,\text{u}$ (right) in an example spectrum acquired from an arginine sample. The peaks are fitted using an exponentially modified gaussian peak function with an added background offset.

$$f(x, a, m, s, t) = \frac{a \cdot s}{t} \cdot \sqrt{\frac{\pi}{2}} \cdot \exp\left(\frac{1}{2}\left(\frac{s}{t}\right)^2 - \frac{x-m}{t}\right) \cdot \operatorname{erfc}\left(\frac{1}{\sqrt{2}} \cdot \left(\frac{s}{t} - \frac{x-m}{s}\right)\right) \quad (C.3)$$

$$f(x, a, m, s, t) = a \cdot \exp\left(-\frac{1}{2}\left(\frac{x-m}{s}\right)^2\right) \cdot \frac{s}{t} \cdot \sqrt{\frac{\pi}{2}} \cdot \operatorname{erfcx}\left(\frac{1}{\sqrt{2}} \cdot \left(\frac{s}{t} - \frac{x-m}{s}\right)\right) \quad (C.4)$$

The peak fitting was performed with Python scripts utilizing the scipy.curve_fit function with initial parameter estimates and fit-windows derived from a pre-defined peak parameter list (defining a peak position estimate and fit range window) and the individual mass spectrum. Two exemplary peak fits of mass peaks $m = 28\,\text{u}$ (left) and $m = 175\,\text{u}$ (right) in a spectrum acquired from an arginine sample are shown in Figure C.2. A number of fit parameters as well as the coefficient of determination R^2 were programmatically monitored for each individual peak fit performed and the resulting peak fits were inspected visually for noticeable problems. Subsequently, the number of counts for the individual mass peak was then determined by integration over the fit function as given in Formulas C.3 and C.4 (without the constant background). The integration boundaries for each individual mass peak were identically pre-defined for all analysed spectra.

C.3. Additional peak yields and fragmentation data

Arginine

The formation of the small $m = 30\,\mathrm{u}$ fragment ion (C.3) is significantly less likely than that for the $m = 43\,\mathrm{u}$ fragment ion (see 5.15, which likely reflects the additionally required bond break and protonation). For the $m = 30\,\mathrm{u}$ fragment ion the observed decrease in fragmentation with electronic stopping and cluster size in case of the cluster primary ions is also less significant and slower than for the bigger $m = 43\,\mathrm{u}$ fragment ion. The data obtained with the large C_{60} primary cluster ions indicates a fragmentation roughly comparable to the data obtained with Cu_n primary cluster ions with comparable nuclear stopping power in the sample material.

When viewing the data for the heavier $m = 70\,\mathrm{u}$ fragment ion (C.4), the fragmentation observed from a C_{60} primary cluster ion beam is significantly lower than that of Cu_n primary cluster ions with comparable nuclear stopping power. Apart from this difference the general behaviour and scaling of $m = 70\,\mathrm{u}$ fragmentation, which requires the breakage of 2 bonds in the intact arginine molecule, mirrors the one seen for the $m = 43\,\mathrm{u}$ fragment.

To highlight the differences in fragmentation between the $m = 70\,\mathrm{u}$ and $m = 100\,\mathrm{u}$ fragment ions, Figure C.5 plots the fragmentation ratio of the $m = 70\,\mathrm{u}$ fragment relative to that of the $m = 100\,\mathrm{u}$ fragment: One observes only a very slight change of this ratio with electronic stopping power in the form of a small decrease with increasing stopping power, indicating that both fragment ion yields scale similarly with $m = 70\,\mathrm{u}$ formation more likely for lower electronic stopping. The projection vs. nuclear stopping power (Figure C.5, top right) shows almost no dependence of the ratio on the amount of nuclear stopping. However the ratio observed for C_{60} primary cluster ions is significantly lower than for most other primary ion species used, indicating that the energy deposition through a large cluster ion seems to markedly favour the formation of $m = 100\,\mathrm{u}$ ions with the guanidino group still attached over the formation of the smaller $m = 70\,\mathrm{u}$ fragment ions.

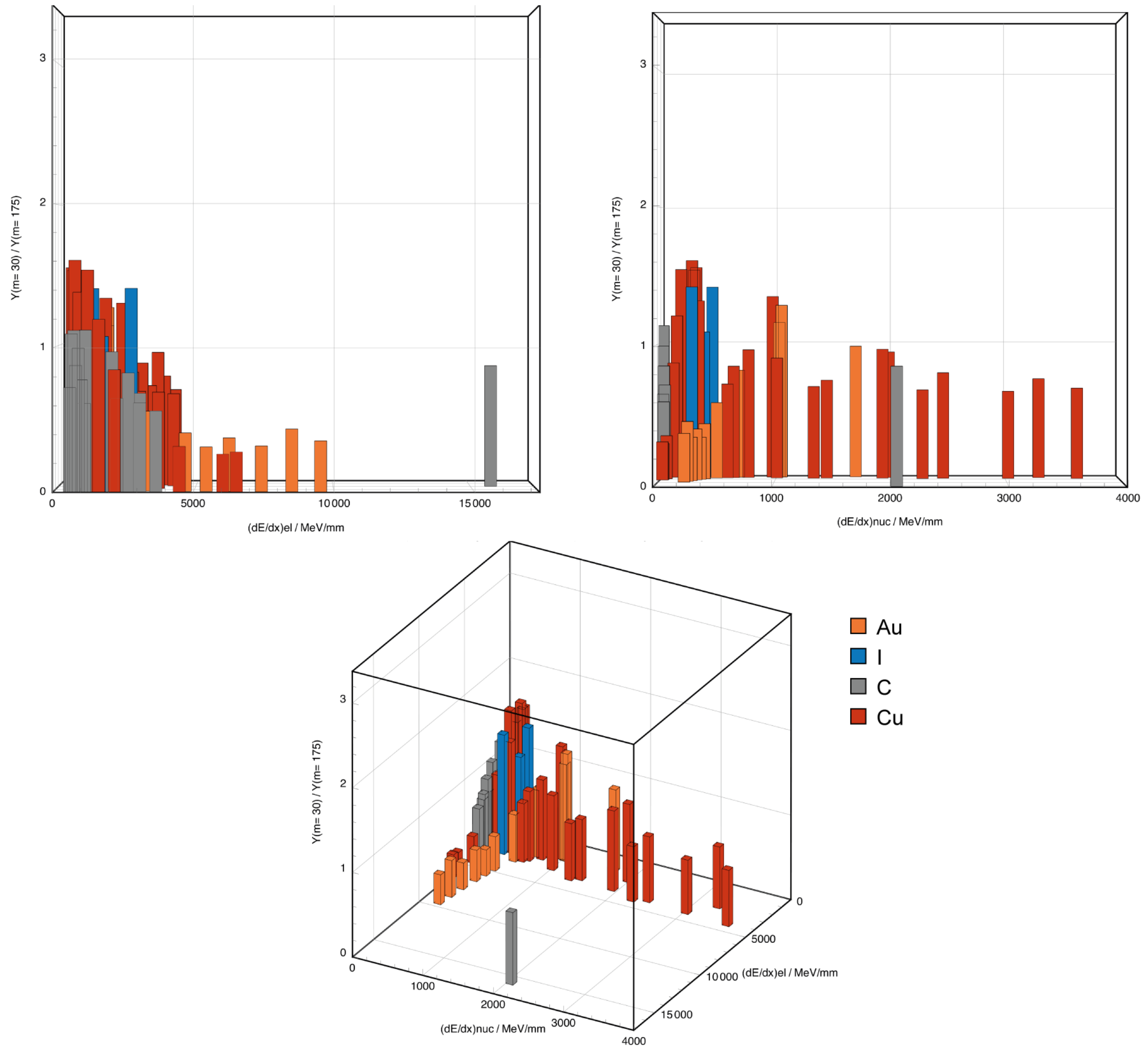

Figure C.3.: Fragmentation (peak yield of fragment ion with mass $m = 30\,\mathrm{u}$ normalized to yield of molecular ion with mass $m = 175\,\mathrm{u}$) of positive secondary ion mass spectra recorded from arginine sample with different monoatomic and cluster ion beams as a function of $\left(\frac{dE}{dx}\right)_e$ and $\left(\frac{dE}{dx}\right)_n$.

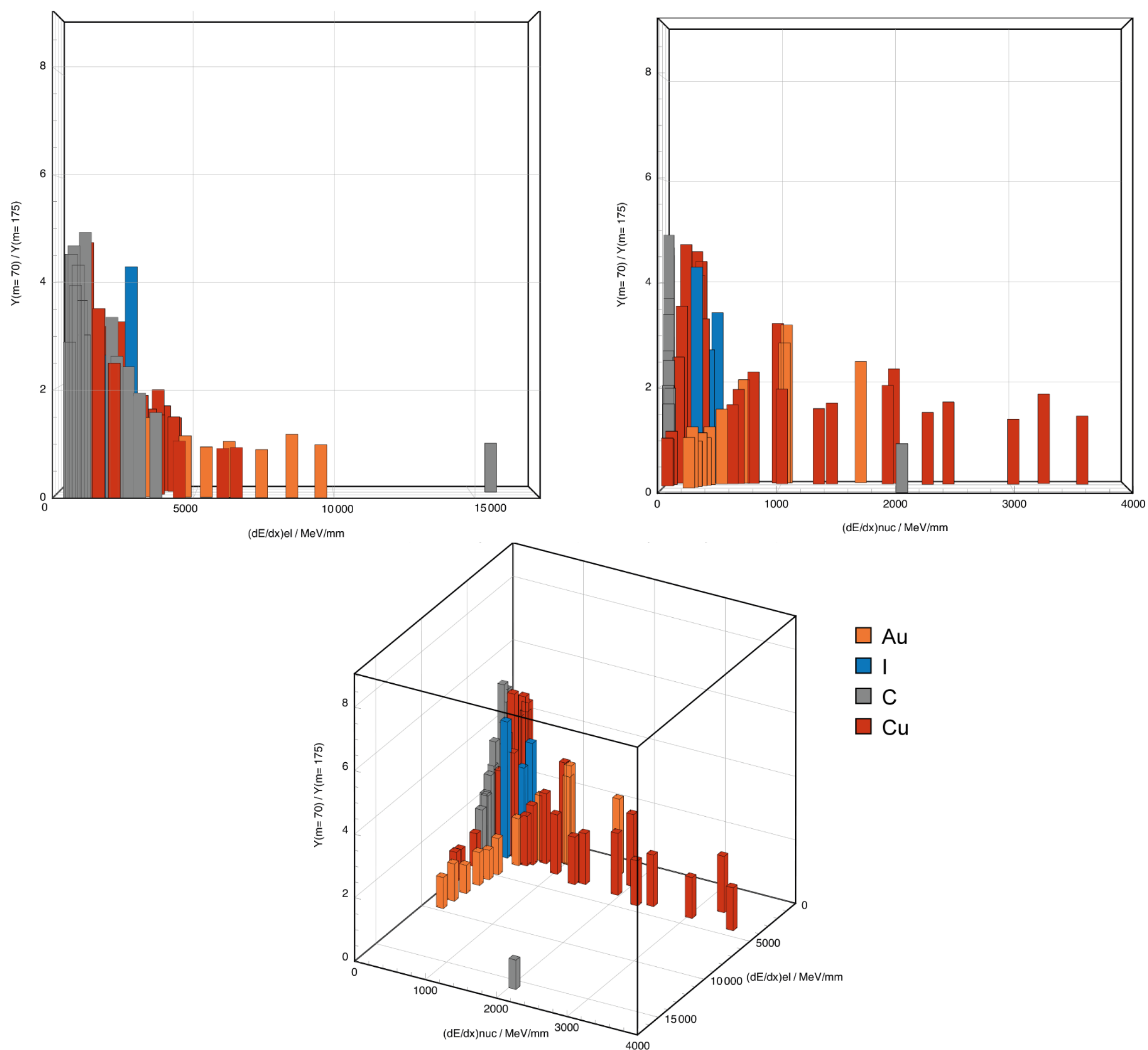

Figure C.4.: Fragmentation (peak yield of fragment ion with mass $m = 70\,\mathrm{u}$ normalized to yield of molecular ion with mass $m = 175\,\mathrm{u}$) of positive secondary ion mass spectra recorded from arginine sample with different monoatomic and cluster ion beams as a function of $\left(\frac{dE}{dx}\right)_e$ and $\left(\frac{dE}{dx}\right)_n$.

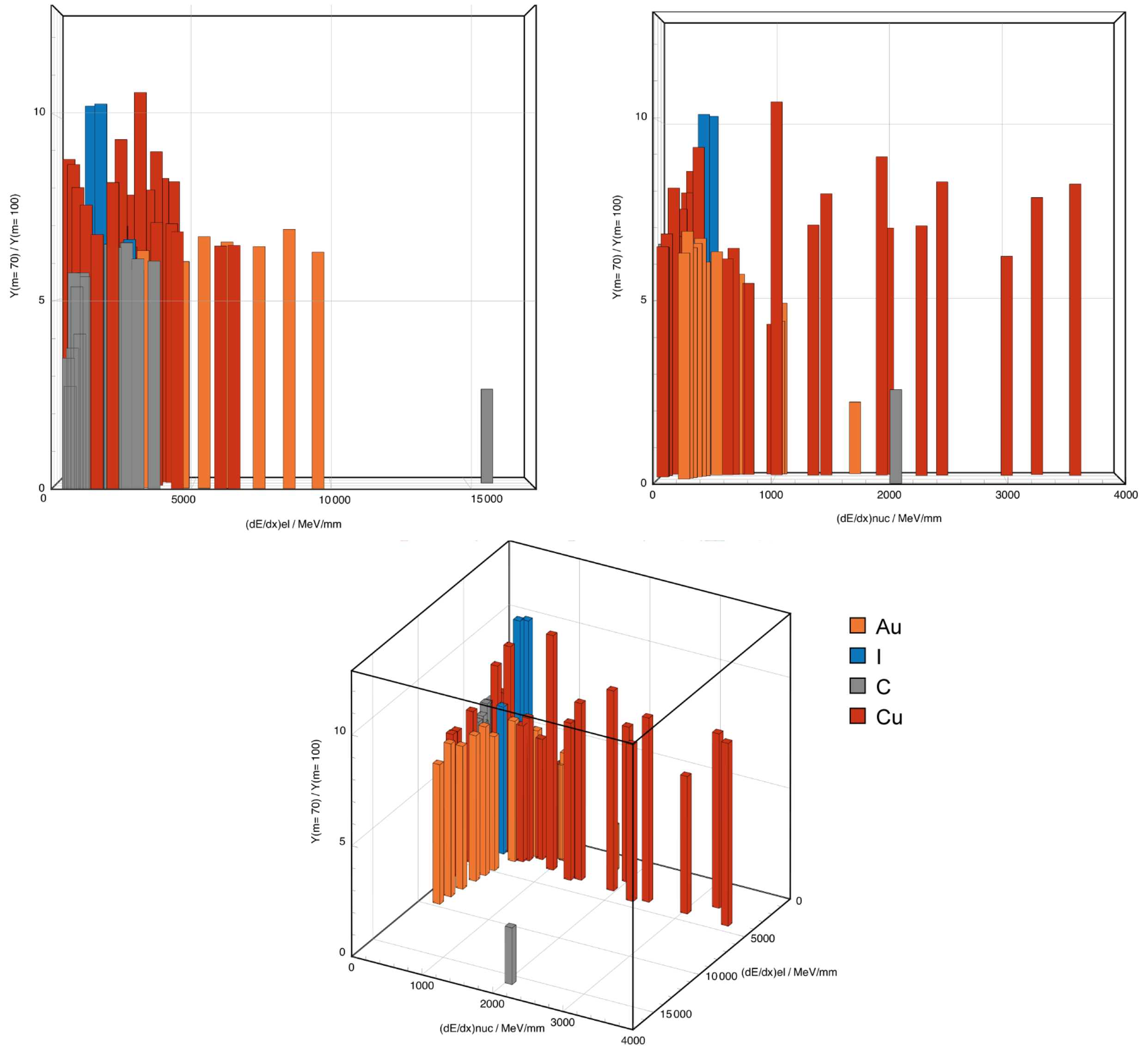

Figure C.5.: Fragmentation (peak yield of fragment ion with mass $m = 70\,\mathrm{u}$ normalized to yield of fragment ion with mass $m = 100\,\mathrm{u}$) of positive secondary ion mass spectra recorded from arginine sample with different monoatomic and cluster ion beams as a function of $\left(\frac{dE}{dx}\right)_e$ and $\left(\frac{dE}{dx}\right)_n$.

Leu-enkephalin

For the fragment ratio of masses $m = 43\,\mathrm{u}$ and $m = 57\,\mathrm{u}$ (Figure C.6) only a very slight decrease is apparent with electronic stopping respectively a slight increase with nuclear stopping. This indicates that the additional bond breaking necessary to separate the methylene group does not seem to depend significantly on stopping conditions and both fragment ions have a very similar formation process. If at all, larger Cu_n primary ion clusters slightly favour the formation of the lighter $m = 43\,\mathrm{u}$ fragment, while C_{60} clusters result in fragmentation comparable to the one of Cu_n with comparable nuclear stopping.

The fragment ion with mass $m = 91\,\mathrm{u}$ and its aromatic hydrocarbon ring shows the lowest yield ratios yet when compared to its larger super-fragment with mass $m = 120\,\mathrm{u}$ originating from the main chain of the leu-enkephalin molecule (Figure C.7). The ratio of both fragment yields shows the familiar pattern of increased electronic stopping and decreased nuclear stopping slightly favouring the formation of the larger fragment. For a C_{60} primary ion cluster beam the fragmentation behaviour of both ions is similar to the one induced by Cu_n cluster ions with comparable nuclear stopping.

PEG

The yield ratio of the $m = 45\,\mathrm{u}$ and $m = 62\,\mathrm{u}$ fragment ions (Figure C.8) shows that formation of the $m = 45\,\mathrm{u}$ fragment (missing the two hydroxy groups) increases with both electronic and nuclear stopping of the primary ion in the material. An increase of Cu_n cluster size also seems to increase the ratio, suggesting that with higher energy deposition the attachment of a hydroxy group becomes less likely. The fragmentation induced by C_{60} primary ions however is roughly in line with that of Cu_n clusters with similar nuclear stopping power.

When setting the $m = 45\,\mathrm{u}$ yields in relation to the $m = 158\,\mathrm{u}$ fragment yields (Figure C.9), the relative yield of the PEG repeat unit increases with both increasing electronic and nuclear stopping. For larger Cu_n primary cluster ions this preference in secondary ion formation seems to be slightly reduced, but the large C_{60} primary ions produce significantly higher yields of the repeat unit at mass $m = 45\,\mathrm{u}$.

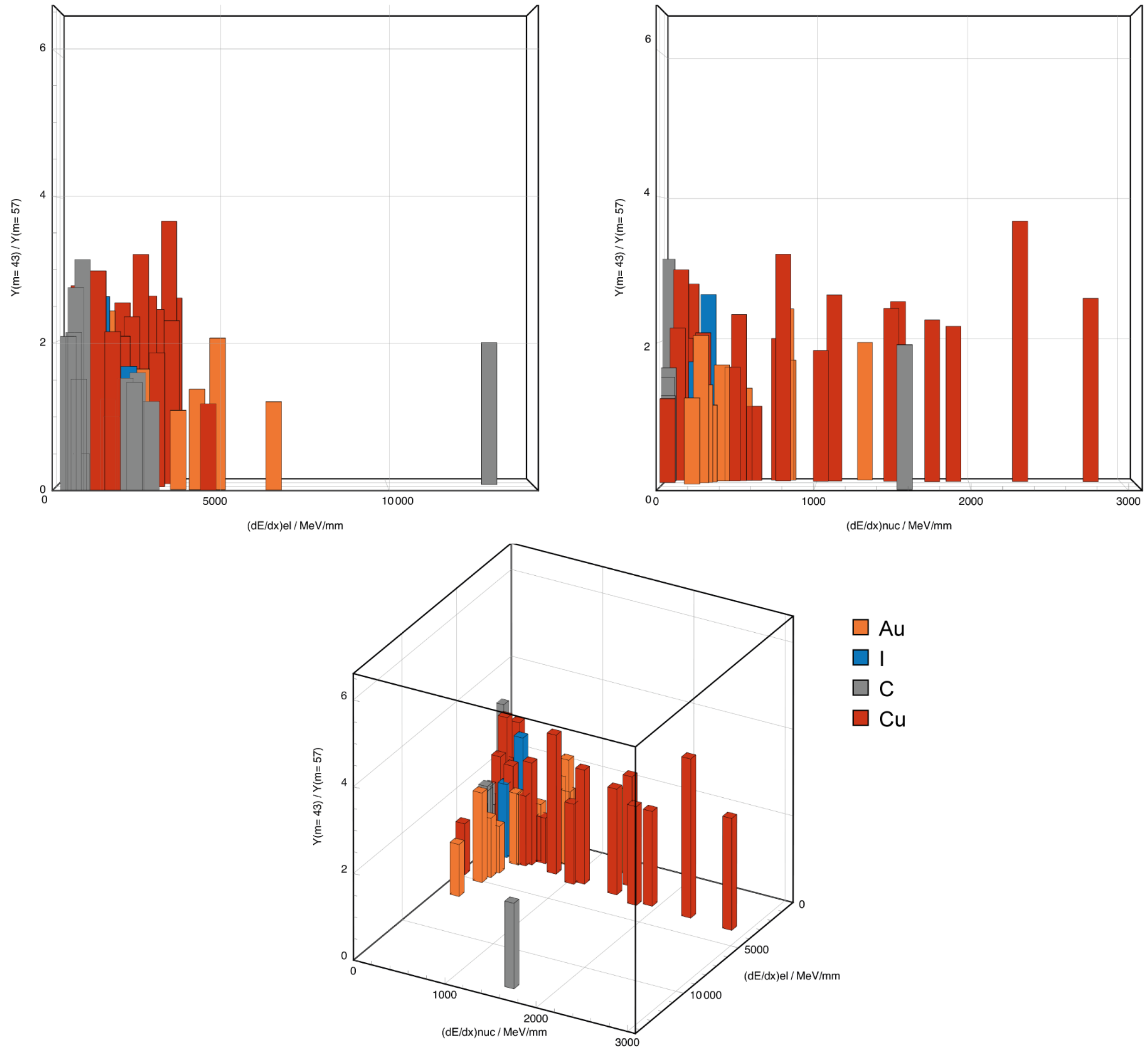

Figure C.6.: Fragmentation (peak yield of fragment ion with mass $m = 43\,\mathrm{u}$ normalized to yield of fragment ion with mass $m = 57\,\mathrm{u}$) of positive secondary ion mass spectra recorded from leu-enkephalin sample with different monoatomic and cluster ion beams as a function of $\left(\frac{dE}{dx}\right)_e$ and $\left(\frac{dE}{dx}\right)_n$.

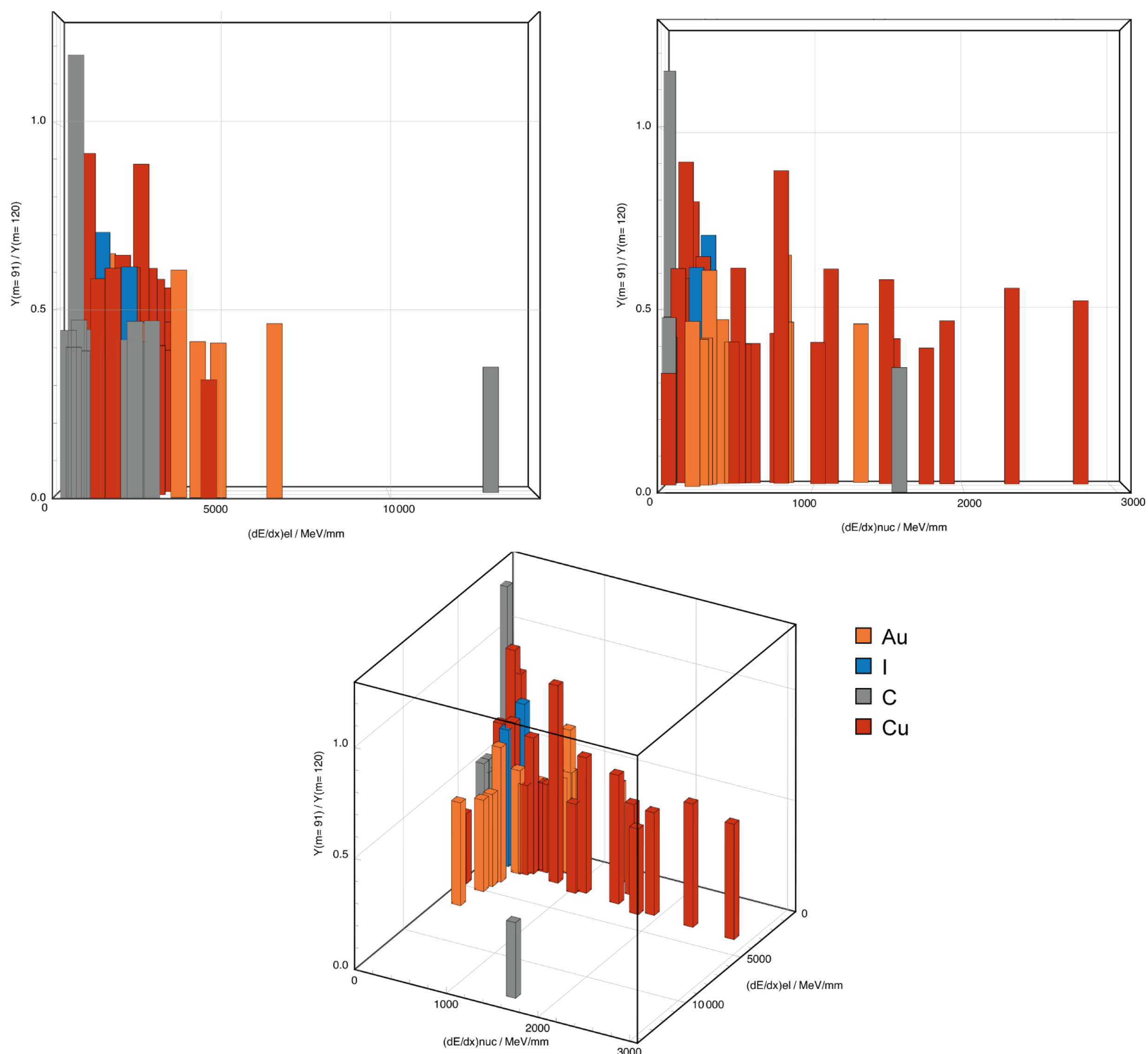

Figure C.7.: Fragmentation (peak yield of fragment ion with mass $m = 91\,\mathrm{u}$ normalized to yield of fragment ion with mass $m = 120\,\mathrm{u}$) of positive secondary ion mass spectra recorded from leu-enkephalin sample with different monoatomic and cluster ion beams as a function of $\left(\frac{dE}{dx}\right)_e$ and $\left(\frac{dE}{dx}\right)_n$.

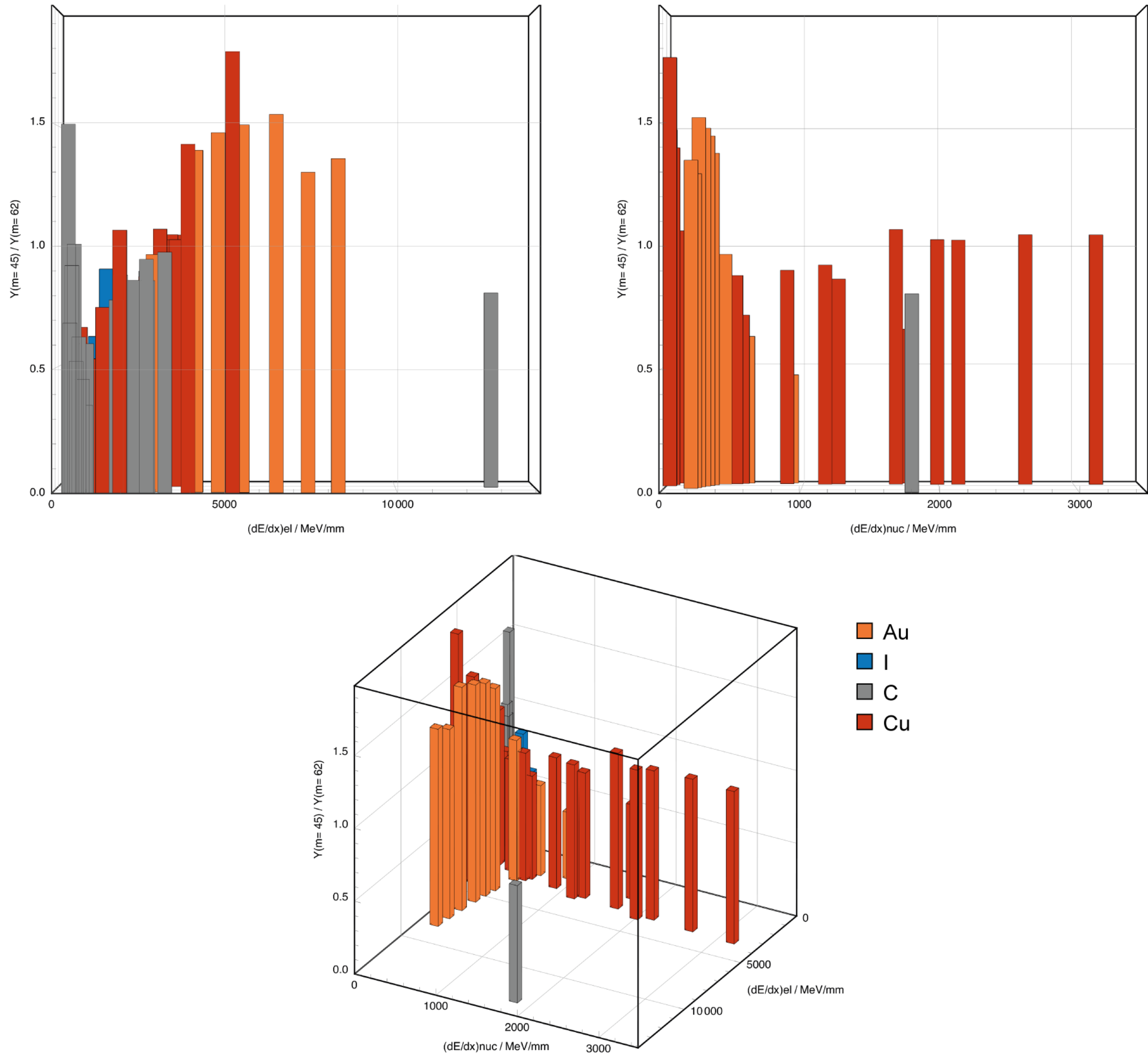

Figure C.8.: Fragmentation (peak yield of fragment ion with mass $m = 45\,\mathrm{u}$ normalized to yield of fragment ion with mass $m = 62\,\mathrm{u}$) of positive secondary ion mass spectra recorded from PEG sample with different monoatomic and cluster ion beams as a function of $\left(\frac{dE}{dx}\right)_e$ and $\left(\frac{dE}{dx}\right)_n$.

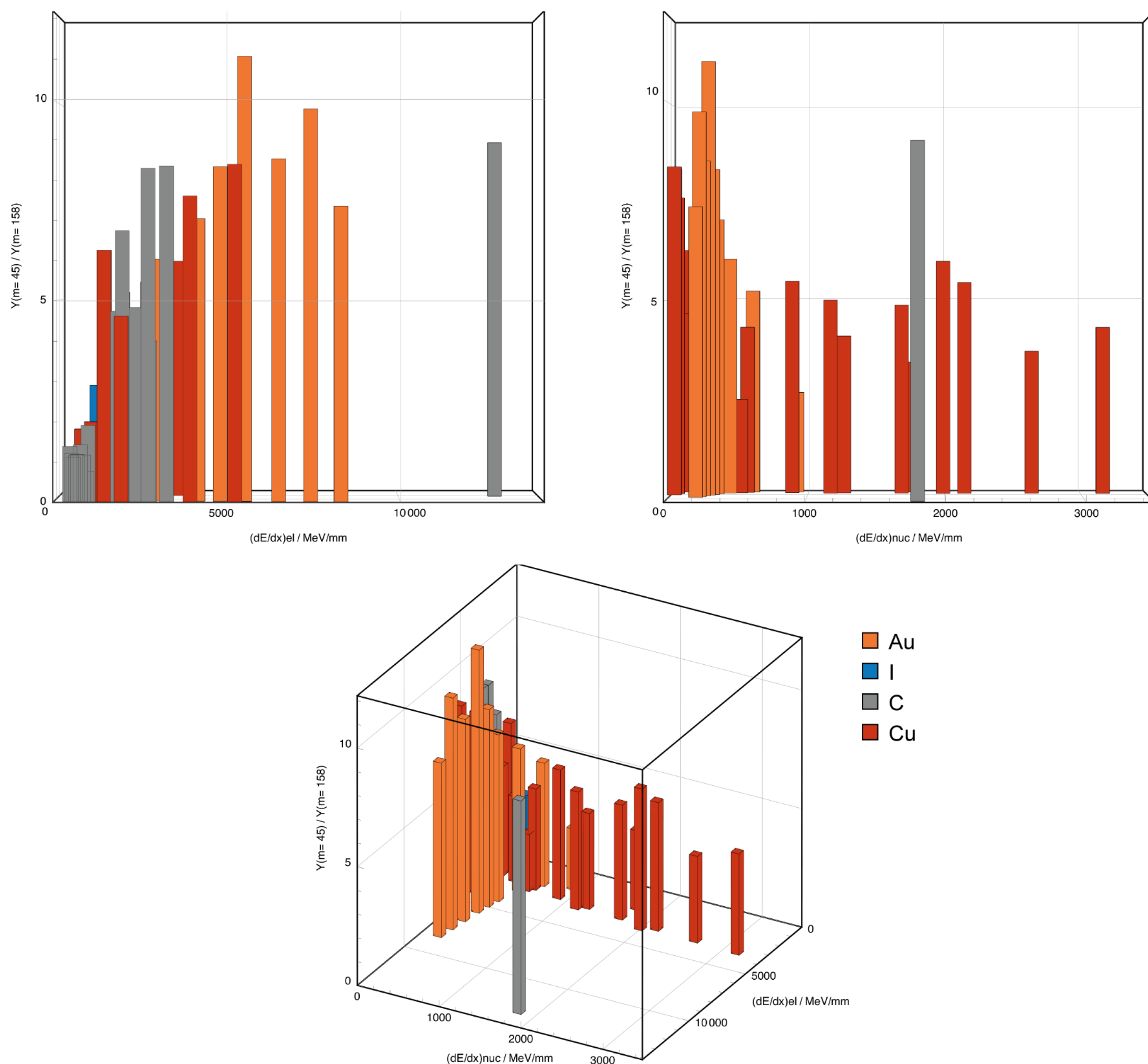

Figure C.9.: Fragmentation (peak yield of fragment ion with mass $m = 45\,\mathrm{u}$ normalized to yield of fragment ion with mass $m = 158\,\mathrm{u}$) of positive secondary ion mass spectra recorded from PEG sample with different monoatomic and cluster ion beams as a function of $\left(\frac{dE}{dx}\right)_e$ and $\left(\frac{dE}{dx}\right)_n$.

Bibliography

Albers, A., Wien, K., Dück, P., Treu, W., and Voit, H. (1982): "Secondary Ion Emission from Dielectric Films as a Function of Primary Ion Velocity". In: *Nuclear Instruments and Methods in Physics Research* 198.1, pp. 69–74. DOI: `10.1016/0167-5087(82)90054-0`.

Assmann, W., Toulemonde, M., and Trautmann, C. (2007): "Electronic Sputtering with Swift Heavy Ions". In: *Sputtering by Particle Bombardment: Experiments and Computer Calculations from Threshold to MeV Energies*. Topics in Applied Physics. Berlin, Heidelberg: Springer, pp. 401–450. DOI: `10.1007/978-3-540-44502-9_7`.

Bailey, M. J., Jones, B. N., Hinder, S., Watts, J., Bleay, S., and Webb, R. P. (2010): "Depth Profiling of Fingerprint and Ink Signals by SIMS and MeV SIMS". In: *Nuclear Instruments and Methods in Physics Research Section B: Beam Interactions with Materials and Atoms*. 19th International Conference on Ion Beam Analysis 268.11–12, pp. 1929–1932. DOI: `10.1016/j.nimb.2010.02.104`.

Becker, O., Della-Negra, S., Le Beyec, Y., and Wien, K. (1986): "MeV Heavy Ion Induced Desorption from Insulating Films as Function of Projectile Velocity". In: *Nuclear Instruments and Methods in Physics Research Section B: Beam Interactions with Materials and Atoms* 16.4, pp. 321–333. DOI: `10.1016/0168-583X(86)90091-1`.

Benninghoven, A. (1971): "Beobachtung von Oberflächenreaktionen Mit Der Statischen Methode Der Sekundärionen-Massenspektroskopie. I Die Methode". In: *Surface Science* 28.2, pp. 541–562. DOI: `10.1016/0039-6028(71)90061-6`.

Benninghoven, A. and Sichtermann, W. K. (1978): "Detection, Identification, and Structural Investigation of Biologically Important Compounds by Secondary Ion Mass Spectrometry". In: *Analytical Chemistry* 50.8, pp. 1180–1184. DOI: `10.1021/ac50030a043`.

Bitensky, I. S. and Parilis, E. S. (1987): "Shock Wave Mechanism for Cluster Emission and Organic Molecule Desorption under Heavy Ion Bombardment". In: *Nuclear Instruments and Methods in Physics Research Section B: Beam Interactions with Materials and Atoms* 21.1, pp. 26–36. DOI: `10.1016/0168-583X(87)90135-2`.

Bodzon-Kulakowska, A. and Suder, P. (2016): "Imaging Mass Spectrometry: Instrumentation, Applications, and Combination with Other Visualization Techniques". In: *Mass Spectrometry Reviews* 35.1, pp. 147–169. DOI: `10.1002/mas.21468`.

Bogdanović Radović, I., Siketić, Z., Jembrih-Simbürger, D., Marković, N., Anghelone, M., Stoytschew, V., and Jakšić, M. (2017): "Identification and Imaging of Modern Paints Using Secondary Ion Mass Spectrometry with MeV Ions". In: *Nuclear Instruments and*

Methods in Physics Research Section B: Beam Interactions with Materials and Atoms. Proceedings of the 12th European Conference on Accelerators in Applied Research and Technology (ECAART12) 406, pp. 296–301. DOI: 10.1016/j.nimb.2017.01.007.

Bringa, E. M. and Johnson, R. E. (2000): "Electronic Sputtering of Solid O2". In: *Surface Science* 451.1, pp. 108–115. DOI: 10.1016/S0039-6028(00)00015-7.

Brunelle, A., Della-Negra, S., Deprun, C., Depauw, J., Håkansson, P., Jacquet, D., le Beyec, Y., and Pautrat, M. (1997): "High Desorption—Ionization Yields of Large Biomolecules Induced by Fast C60 Projectiles". In: *International Journal of Mass Spectrometry and Ion Processes* 164.3, pp. 193–200. DOI: 10.1016/S0168-1176(97)00057-8.

Castaing, R. and Slodzian, G. (1962): "Optique Corpusculaire-Premiers Essais de Microanalyse Par Emission Ionique Secondaire". In: *Comptes Rendus Hebdomadaires Des Seances De L Academie Des Sciences* 255.16, p. 1893.

Chait, B. T., Agosta, W. C., and Field, F. H. (1981): "Fission Fragment Ionization (252Cf) Mass Spectrometry. Positive and Negative Spectra and Decomposition Mechanisms for Seven Compounds". In: *International Journal of Mass Spectrometry and Ion Physics* 39.3, pp. 339–366. DOI: 10.1016/0020-7381(81)87007-6.

Chater, R. J., Shollock, B. A., McPhail, D. S., Smith, A. J., and Cooke, G. (2014): "Differentially Pumped Quadrupole SIMS Probe on FIB-Based and Two-Beam Microscopes". In: *Surface and Interface Analysis* 46.S1, pp. 372–374. DOI: 10.1002/sia.5665.

Cheng, J. and Winograd, N. (2006): "Molecular Depth Profiling of Multi-Layer Systems with Cluster Ion Sources". In: *Applied Surface Science*. Proceedings of the 15th International Conference on Secondary Ion Mass Spectrometry, 252.19, pp. 6498–6501. DOI: 10.1016/j.apsusc.2006.02.207.

Cloete, K. J., Jenčič, B., Šmit, Ž., Kelemen, M., Mkentane, K., and Pelicon, P. (2017): "Detection of Lithium in Scalp Hair by Time-of-Flight Secondary Ion Mass Spectrometry with High Energy (MeV) Primary Ions". In: *Analytical Methods* 9.36, pp. 5249–5253. DOI: 10.1039/C7AY01616F.

Cobice, D. F., Goodwin, R. J. A., Andren, P. E., Nilsson, A., Mackay, C. L., and Andrew, R. (2015): "Future Technology Insight: Mass Spectrometry Imaging as a Tool in Drug Research and Development". In: *British Journal of Pharmacology* 172.13, pp. 3266–3283. DOI: 10.1111/bph.13135. pmid: 25766375.

Daya, D. D. N. B., Demirev, P., Eriksson, J., Hallén, A., Håkansson, P., Johnson, R. E., Kopniczky, J., Papaléo, R. M., Reimann, C. T., Rottler, J., and Sundqvist, B. U. R. (1997): "Interaction of MeV Atomic Ions with Molecular Solids: Ion Track Structure and Sputtering Phenomena". In: *Radiation Measurements*. International Conference on Nuclear Tracks in Solids 28.1, pp. 101–110. DOI: 10.1016/S1350-4487(97)00048-6.

Delcorte, A. and Bertrand, P. (2004): "Interest of Silver and Gold Metallization for Molecular SIMS and SIMS Imaging". In: *Applied Surface Science*. Proceedings of the 14th International Conference on Secondary Ion Mass Spectrometry and Related Topics 231-232, pp. 250–255. DOI: `10.1016/j.apsusc.2004.03.029`.

Delcorte, A., Garrison, B. J., and Hamraoui, K. (2009): "Dynamics of Molecular Impacts on Soft Materials: From Fullerenes to Organic Nanodrops". In: *Analytical Chemistry* 81.16, pp. 6676–6686. DOI: `10.1021/ac900746x`.

Delcorte, A. (2006): "Matrix-Enhanced Secondary Ion Mass Spectrometry: The Alchemist's Solution?" In: *Applied Surface Science*. Proceedings of the 15th International Conference on Secondary Ion Mass Spectrometry 252.19, pp. 6582–6587. DOI: `10.1016/j.apsusc.2006.02.076`.

Dück, P., Fröhlich, H., Bischof, N., and Voit, H. (1982): "Yield Measurements of Organic Molecules Desorbed by Energetic Heavy Ions as a Function of the Ionic Charge State". In: *Nuclear Instruments and Methods in Physics Research* 198.1, pp. 39–41. DOI: `10.1016/0167-5087(82)90049-7`.

Eller, M. J., Cottereau, E., Rasser, B., Verzeroli, E., Agnus, B., Gaubert, G., Donzel, X., Delobbe, A., and Della-Negra, S. (2015): "Andromede Project: Surface Analysis and Modification with Probes from Hydrogen to Nano-Particles in the MeV Energy Range". In: *Nuclear Instruments and Methods in Physics Research Section B: Beam Interactions with Materials and Atoms*. Proceedings of the 19th International Conference on Ion Beam Modification of Materials (IBMM 2014) 365, pp. 367–370. DOI: `10.1016/j.nimb.2015.07.090`.

Eller, M. J., Verkhoturov, S. V., and Schweikert, E. A. (2016): "Testing Molecular Homogeneity at the Nanoscale with Massive Cluster Secondary Ion Mass Spectrometry". In: *Analytical Chemistry* 88.15, pp. 7639–7646. DOI: `10.1021/acs.analchem.6b01466`.

Fenyö, D. and Johnson, R. E. (1992): "Computer Experiments on Molecular Ejection from an Amorphous Solid: Comparison to an Analytic Continuum Mechanical Model". In: *Physical Review B* 46.9, pp. 5090–5099. DOI: `10.1103/PhysRevB.46.5090`.

Fernandez-Lima, F. A., Post, J., DeBord, J. D., Eller, M. J., Verkhoturov, S. V., Della-Negra, S., Woods, A. S., and Schweikert, E. A. (2011): "Analysis of Native Biological Surfaces Using a 100 kV Massive Gold Cluster Source". In: *Analytical Chemistry* 83.22, pp. 8448–8453. DOI: `10.1021/ac201481r`.

Folkard, M., Prise, K. M., Vojnovic, B., Newman, H. C., Roper, M. J., Hollis, K. J., and Michael, B. D. (1995): "Conventional and Microbeam Studies Using Low Energy Charged Particles Relevant to Risk Assessment and the Mechanisms of Radiation Action". In: *Radiation Protection Dosimetry* 61.1-3, pp. 215–218. DOI: `10.1093/oxfordjournals.rpd.a082786`.

Fujita, N., Ishii, K., and Ogawa, H. (2009): “Development of In-Air-RBS Method with Tapered Glass Capillary”. In: *Journal of Physics: Conference Series* 194.14, p. 142004. DOI: 10.1088/1742-6596/194/14/142004.

Fujita, N., Ishii, K., and Ogawa, H. (2011): “Development of Two-Dimensional Mapping Technique by in-Air-PIXE with Metal Capillary”. In: *Nuclear Instruments and Methods in Physics Research Section B: Beam Interactions with Materials and Atoms*. Proceedings of the 24th International Conference on Atomic Collisions in Solids (ICACS-24) 269.9, pp. 1023–1025. DOI: 10.1016/j.nimb.2010.11.065.

Geng, S., Verkhoturov, S. V., Eller, M. J., Della-Negra, S., and Schweikert, E. A. (2017): “The Collision of a Hypervelocity Massive Projectile with Free-Standing Graphene: Investigation of Secondary Ion Emission and Projectile Fragmentation”. In: *The Journal of Chemical Physics* 146.5, p. 054305. DOI: 10.1063/1.4975171.

Griffith, J. E., Weller, R. A., Seiberling, L. E., and Tombrello, T. A. (1980): “Sputtering of Uranium Tetrafluoride in the Electronic Stopping Region”. In: *Radiation Effects* 51.3-4, pp. 223–231. DOI: 10.1080/00337578008210004.

Guillermier, C., Negra, S. D., Rickman, R. D., Pinnick, V., and Schweikert, E. A. (2006): “Influence of Massive Projectile Size and Energy on Secondary Ion Yields from Organic Surfaces”. In: *Applied Surface Science*. Proceedings of the 15th International Conference on Secondary Ion Mass Spectrometry 252.19, pp. 6529–6532. DOI: 10.1016/j.apsusc.2006.02.077.

Gurdak, E., Green, F. M., Rakowska, P. D., Seah, M. P., Salter, T. L., and Gilmore, I. S. (2014): “VAMAS Interlaboratory Study for Desorption Electrospray Ionization Mass Spectrometry (DESI MS) Intensity Repeatability and Constancy”. In: *Analytical Chemistry* 86.19, pp. 9603–9611. DOI: 10.1021/ac502075t.

Gutierres, L. I., Lima, N. W., Thomaz, R. S., Papaléo, R. M., and Bringa, E. M. (2017): “Simulations of Cratering and Sputtering from an Ion Track in Crystalline and Amorphous Lennard Jones Thin Films”. In: *Computational Materials Science* 129, pp. 98–106. DOI: 10.1016/j.commatsci.2016.12.001.

Haff, P. K. (1976): “Possible New Sputtering Mechanism in Track Registering Materials”. In: *Applied Physics Letters* 29.8, pp. 473–475. DOI: 10.1063/1.89126.

Haff, P. and Seiberling, L. (1981): “Anomalous Sputtering at High Energy”. In: *Nature* 290.5807, pp. 544–545. DOI: 10.1038/290544a0.

Håkansson, P., Jayasinghe, E., Johansson, A., Kamensky, I., and Sundqvist, B. (1981): “Charge-State Dependence of Desorption of Biomolecules Induced by Fast Heavy Ions”. In: *Physical Review Letters* 47.17, pp. 1227–1229. DOI: 10.1103/PhysRevLett.47.1227.

Håkansson, P., Johansson, A., Kamensky, I., Sundqvist, B., Fohlman, J., and Peterson, P. (1981): "Fast Heavy-Ion Induced Desorption of Biomolecules". In: *IEEE Transactions on Nuclear Science* 28.2, pp. 1776–1778. DOI: 10.1109/TNS.1981.4331519.

Hasegawa, J., Jaiyen, S., Polee, C., and Oguri, Y. (2011): "Development of a Micro-PIXE System Using Tapered Glass Capillary Optics". In: *Nuclear Instruments and Methods in Physics Research Section B: Beam Interactions with Materials and Atoms*. Proceedings of the 10th European Conference on Accelerators in Applied Research and Technology (ECAART10) 269.24, pp. 3087–3090. DOI: 10.1016/j.nimb.2011.04.073.

Hasegawa, J., Shiba, S., Fukuda, H., and Oguri, Y. (2008): "A Compact Micro-Beam System Using a Tapered Glass Capillary for Proton-Induced X-Ray Radiography". In: *Nuclear Instruments and Methods in Physics Research Section B: Beam Interactions with Materials and Atoms*. Proceedings of the 9th European Conference on Accelerators in Applied Research and Technology (ECAART9) 266.10, pp. 2125–2129. DOI: 10.1016/j.nimb.2008.02.051.

Hedin, A., Håkansson, P., Salehpour, M., and Sundqvist, B. U. R. (1987): "Fast-Ion-Induced Erosion of Leucine as a Function of the Electronic Stopping Power". In: *Physical Review B* 35.14, pp. 7377–7381. DOI: 10.1103/PhysRevB.35.7377.

Hedin, A., Håkansson, P., Sundqvist, B., and Johnson, R. E. (1985): "Ion-Track Model for Fast-Ion-Induced Desorption of Molecules". In: *Physical Review B* 31.4, pp. 1780–1787. DOI: 10.1103/PhysRevB.31.1780.

Heeren, R. M. A., McDonnell, L. A., Amstalden, E., Luxembourg, S. L., Altelaar, A. F. M., and Piersma, S. R. (2006): "Why Don't Biologists Use SIMS?: A Critical Evaluation of Imaging MS". In: *Applied Surface Science*. Proceedings of the 15th International Conference on Secondary Ion Mass Spectrometry 252.19, pp. 6827–6835. DOI: 10.1016/j.apsusc.2006.02.134.

Hellborg, R. and Hellborg, R. (2005): *Electrostatic Accelerators: Fundamentals and Applications*. Springer. URL: http://ebookcentral.proquest.com/lib/eth/detail.action?docID=304145 (visited on 06/23/2020).

Hittle, L. R., Altland, D. E., Proctor, A., and Hercules, D. M. (1994): "Investigation of Molecular Weight and Terminal Group Effects on the Time-of-Flight Secondary Ion Mass Spectra of Polyglycols". In: *Analytical Chemistry* 66.14, pp. 2302–2312. DOI: 10.1021/ac00086a016.

Holle, A., Haase, A., Kayser, M., and Höhndorf, J. (2006): "Optimizing UV Laser Focus Profiles for Improved MALDI Performance". In: *Journal of Mass Spectrometry* 41.6, pp. 705–716. DOI: 10.1002/jms.1041.

Hunt, J. E. (1987): "Large Molecule Electronic Sputtering by Plasma Desorption and Heavy-Ion Bombardment". In: *Nuclear Instruments and Methods in Physics Research Section B:*

Beam Interactions with Materials and Atoms 27.1, pp. 181–187. DOI: 10.1016/0168-583X(87)90019-X.

Ikeda, T., Kanai, Y., Kojima, T. M., Iwai, Y., Kanazawa, Y., Hoshino, M., Kobayashi, T., Pokhil, G. P., and Yamazaki, Y. (2007): "Focusing of Charged Particle Beams with Various Glass-Made Optics". In: *Journal of Physics: Conference Series* 88.1, p. 012031. DOI: 10.1088/1742-6596/88/1/012031.

Ikeda, T., Kanai, Y., Iwai, Y., Kojima, T. M., Maeshima, K., Meissl, W., Kobayashi, T., Nebiki, T., Miyamoto, S., Pokhil, G. P., Narusawa, T., Imamoto, N., and Yamazaki, Y. (2011): "Glass Capillary Optics for Producing Nanometer Sized Beams and Its Applications". In: *Surface and Coatings Technology*. Surface Modification of Materials by Ion Beams 2009 206.5, pp. 859–863. DOI: 10.1016/j.surfcoat.2011.03.098.

Imanishi, N., Shimizu, A., Ohta, H., and Itoh, A. (1999): "Electronic Sputtering from an SiO2 Target Bombarded by Heavy Ions". In: *AIP Conference Proceedings* 475.1, pp. 396–400. DOI: 10.1063/1.59161.

Jakas, M. M., Bringa, E. M., and Johnson, R. E. (2002): "Fluid Dynamics Calculation of Sputtering from a Cylindrical Thermal Spike". In: *Physical Review B* 65.16, p. 165425. DOI: 10.1103/PhysRevB.65.165425.

Jenčič, B. (2018): "Imaging Mass Spectroscopy MeV-SIMS with Continuous Primary Beam". Doctoral Thesis. University of Ljubljana. URL: https://repozitorij.uni-lj.si/IzpisGradiva.php?id=103225 (visited on 02/21/2020).

Jenčič, B., Jeromel, L., Ogrinc Potočnik, N., Vogel-Mikuš, K., Kovačec, E., Regvar, M., Siketić, Z., Vavpetič, P., Rupnik, Z., Bučar, K., Kelemen, M., Kovač, J., and Pelicon, P. (2016): "Molecular Imaging of Cannabis Leaf Tissue with MeV-SIMS Method". In: *Nuclear Instruments and Methods in Physics Research Section B: Beam Interactions with Materials and Atoms*. Proceedings of the 22nd International Conference on Ion Beam Analysis (IBA 2015) 371, pp. 205–210. DOI: 10.1016/j.nimb.2015.10.047.

Jenčič, B., Vavpetič, P., Kelemen, M., Vencelj, M., Vogel-Mikuš, K., Kavčič, A., and Pelicon, P. (2019): "MeV-SIMS ToF Imaging of Organic Tissue with Continuous Primary Beam". In: *Journal of the American Society for Mass Spectrometry* 30.9, pp. 1801–1812. DOI: 10.1021/jasms.8b06094.

Jeromel, L., Siketić, Z., Ogrinc Potočnik, N., Vavpetič, P., Rupnik, Z., Bučar, K., and Pelicon, P. (2014): "Development of Mass Spectrometry by High Energy Focused Heavy Ion Beam: MeV SIMS with 8 MeV Cl7+ Beam". In: *Nuclear Instruments and Methods in Physics Research Section B: Beam Interactions with Materials and Atoms*. Proceedings of the 21st International Conference on Ion Beam Analysis 332, pp. 22–27. DOI: 10.1016/j.nimb.2014.02.022.

Johnson, R. E. and Evatt, R. (1980): "Thermal Spikes and Sputtering Yields". In: *Radiation Effects* 52.3-4, pp. 187–190. DOI: 10.1080/00337578008210031.

Johnson, R. E., Sundqvist, B. U. R., Hedin, A., and Fenyö, D. (1989): "Sputtering by Fast Ions Based on a Sum of Impulses". In: *Physical Review B* 40.1, pp. 49–53. DOI: 10.1103/PhysRevB.40.49.

Johnson, R. E. and Sundqvist, B. U. R. (1992): "Electronic Sputtering: From Atomic Physics to Continuum Mechanics". In: *Physics Today* 45, pp. 28–36. DOI: 10.1063/1.881332.

Jones, B. N. (2012): "The Development of MeV Secondary Ion Mass Spectrometry". Doctoral Thesis. University of Surrey. URL: https://ethos.bl.uk/OrderDetails.do?uin=uk.bl.ethos.580361 (visited on 02/21/2020).

Jones, B. N., Matsuo, J., Nakata, Y., Yamada, H., Watts, J., Hinder, S., Palitsin, V., and Webb, R. (2011): "Comparison of MeV Monomer Ion and keV Cluster ToF-SIMS". In: *Surface and Interface Analysis* 43.1-2, pp. 249–252. DOI: 10.1002/sia.3520.

Jones, B. N., Palitsin, V., and Webb, R. (2010): "Surface Analysis with High Energy Time-of-Flight Secondary Ion Mass Spectrometry Measured in Parallel with PIXE and RBS". In: *Nuclear Instruments and Methods in Physics Research Section B: Beam Interactions with Materials and Atoms*. Proceedings of the 19th International Conference on Ion Beam Analysis 268.11, pp. 1714–1717. DOI: 10.1016/j.nimb.2010.02.045.

Karas, M. and Hillenkamp, F. (1988): "Laser Desorption Ionization of Proteins with Molecular Masses Exceeding 10,000 Daltons". In: *Analytical Chemistry* 60.20, pp. 2299–2301. DOI: 10.1021/ac00171a028.

Keinonen, J. (2005): "Atomic Collisions in Matter". In: *Electrostatic Accelerators: Fundamentals and Applications*. Ed. by R. Hellborg. Particle Acceleration and Detection. Springer, pp. 486–505. DOI: 10.1007/3-540-27095-7_38.

Keller, B. O., Sui, J., Young, A. B., and Whittal, R. M. (2008): "Interferences and Contaminants Encountered in Modern Mass Spectrometry". In: *Analytica Chimica Acta*. Mass Spectrometry 627.1, pp. 71–81. DOI: 10.1016/j.aca.2008.04.043.

King, B. V., Tsong, I. S. T., and Lin, S. H. (1987): "Mechanisms of Ion-Induced Desorption of Large Molecules and Clusters". In: *International Journal of Mass Spectrometry and Ion Processes* 78, pp. 341–356. DOI: 10.1016/0168-1176(87)87059-3.

Kusakari, M., Gnaser, H., Fujii, M., Seki, T., Aoki, T., and Matsuo, J. (2015): "Molecular Cluster Emission in Sputtering of Amino Acids by Argon Gas-Cluster Ions". In: *International Journal of Mass Spectrometry* 383-384, pp. 31–37. DOI: 10.1016/j.ijms.2015.04.003.

Lai, T. L., Jacquet, D., Ribaud, I., Eller, M. J., Verkhoturov, D., Schweikert, E. A., Tizei, L. H. G., Shao, F., Bilgen, S., Mercier, B., Sattonnay, G., and Della Negra, S. (2020): "Enhanced Sputter and Secondary Ion Yields Using MeV Gold Nanoparticle Beams Deliv-

ered by the Andromede Facility". In: *Journal of Vacuum Science & Technology B* 38.4, p. 044008. DOI: 10.1116/6.0000173.

Laiko, V. V., Taranenko, N. I., Berkout, V. D., Yakshin, M. A., Prasad, C. R., Lee, H. S., and Doroshenko, V. M. (2002): "Desorption/Ionization of Biomolecules from Aqueous Solutions at Atmospheric Pressure Using an Infrared Laser at 3 Mm". In: *Journal of the American Society for Mass Spectrometry* 13.4, pp. 354–361. DOI: 10.1016/S1044-0305(02)00341-0.

Laskin, J., Heath, B. S., Roach, P. J., Cazares, L., and Semmes, O. J. (2012): "Tissue Imaging Using Nanospray Desorption Electrospray Ionization Mass Spectrometry". In: *Analytical Chemistry* 84.1, pp. 141–148. DOI: 10.1021/ac2021322.

Le Beyec, Y. (1998): "Cluster Impacts at keV and MeV Energies: Secondary Emission Phenomena". In: *International Journal of Mass Spectrometry and Ion Processes* 174.1-3, pp. 101–117. DOI: 10.1016/S0168-1176(97)00294-2.

Lima, N. W., Gutierres, L. I., Gonzalez, R. I., Müller, S., Thomaz, R. S., Bringa, E. M., and Papaléo, R. M. (2016): "Molecular Dynamics Simulation of Polymerlike Thin Films Irradiated by Fast Ions: A Comparison between FENE and Lennard-Jones Potentials". In: *Physical Review B* 94.19, p. 195417. DOI: 10.1103/PhysRevB.94.195417.

Long, J. V. P. (1965): "A Theoretical Assessment of the Possibility of Selected-Area Mass-Spectrometric Analysis Using a Focused Ion Beam". In: *British Journal of Applied Physics* 16.9, pp. 1277–1284. DOI: 10.1088/0508-3443/16/9/306.

Macfarlane, R. D. and Torgerson, D. F. (1976): "Californium-252 Plasma Desorption Mass Spectroscopy". In: *Science* 191.4230, pp. 920–925.

Matjacic, L. (2018): "Optimisation and Application of AP MeV SIMS." Doctoral Thesis. University of Surrey. URL: http://epubs.surrey.ac.uk/845938/ (visited on 02/21/2020).

Meinerzhagen, F., Breuer, L., Bukowska, H., Bender, M., Severin, D., Herder, M., Lebius, H., Schleberger, M., and Wucher, A. (2016): "A New Setup for the Investigation of Swift Heavy Ion Induced Particle Emission and Surface Modifications". In: *Review of Scientific Instruments* 87.1, p. 013903. DOI: 10.1063/1.4939899.

Miltenberger, K.-U., Schulte-Borchers, M., Döbeli, M., Müller, A. M., George, M., and Synal, H.-A. (2017): "MeV-SIMS Capillary Microprobe for Molecular Imaging". In: *Nuclear Instruments and Methods in Physics Research Section B: Beam Interactions with Materials and Atoms* 412, pp. 185–189. DOI: 10.1016/j.nimb.2017.09.024.

Morris, H. R., Panico, M., Barber, M., Bordoli, R. S., Sedgwick, R. D., and Tyler, A. (1981): "Fast Atom Bombardment: A New Mass Spectrometric Method for Peptide Sequence Analysis". In: *Biochemical and Biophysical Research Communications* 101.2, pp. 623–631. DOI: 10.1016/0006-291X(81)91304-8.

Nakajima, K., Nagano, K., Suzuki, M., Narumi, K., Saitoh, Y., Hirata, K., and Kimura, K. (2014): "Transmission Secondary Ion Mass Spectrometry Using 5 MeV C60+ Ions". In: *Applied Physics Letters* 104.11, p. 114103. DOI: 10.1063/1.4868655.

Nakajima, K., Miyashita, M., Suzuki, M., and Kimura, K. (2014): "Surface Sensitivity of Secondary Ion Mass Spectroscopy in the Electronic Sputtering Regime". In: *Nuclear Instruments and Methods in Physics Research Section B: Beam Interactions with Materials and Atoms*. Proceedings of the 21st International Conference on Ion Beam Analysis 332, pp. 373–376. DOI: 10.1016/j.nimb.2014.02.099.

Nakata, Y., Honda, Y., Ninomiya, S., Seki, T., Aoki, T., and Matsuo, J. (2008): "Yield Enhancement of Molecular Ions with MeV Ion-Induced Electronic Excitation". In: *Applied Surface Science*. Proceedings of the 16th International Conference on Secondary Ion Mass Spectrometry (SIMS XVI) 255.4, pp. 1591–1594. DOI: 10.1016/j.apsusc.2008.05.108.

Nakata, Y., Honda, Y., Ninomiya, S., Seki, T., Aoki, T., and Matsuo, J. (2009): "Matrix-Free High-Resolution Imaging Mass Spectrometry with High-Energy Ion Projectiles". In: *Journal of Mass Spectrometry* 44.1, pp. 128–136. DOI: 10.1002/jms.1482.

Nastasi, M., Mayer, J. W., Wang, Y., Mayer, J. W., and Wang, Y. (2014): *Ion Beam Analysis : Fundamentals and Applications*. CRC Press. DOI: 10.1201/b17310.

Nebiki, T., Sekiba, D., Yonemura, H., Wilde, M., Ogura, S., Yamashita, H., Matsumoto, M., Fukutani, K., Okano, T., Kasagi, J., Iwamura, Y., Itoh, T., Kuribayashi, S., Matsuzaki, H., and Narusawa, T. (2008): "Taper Angle Dependence of the Focusing Effect of High Energy Heavy Ion Beams by Glass Capillaries". In: *Nuclear Instruments and Methods in Physics Research Section B: Beam Interactions with Materials and Atoms*. Ion Beam Analysis 266.8, pp. 1324–1327. DOI: 10.1016/j.nimb.2008.01.022.

Nebiki, T., Yamamoto, T., Narusawa, T., Breese, M. B. H., Teo, E. J., and Watt, F. (2003): "Focusing of MeV Ion Beams by Means of Tapered Glass Capillary Optics". In: *Journal of Vacuum Science & Technology A* 21.5, pp. 1671–1674. DOI: 10.1116/1.1597889.

Nebiki, T., Kabir, M. H., and Narusawa, T. (2006): "In-Air PIXE Analysis by Means of Glass Capillary Optics". In: *Nuclear Instruments and Methods in Physics Research Section B: Beam Interactions with Materials and Atoms*. Proceedings of the 17th International Conference on Ion Beam Analysis 249.1–2, pp. 226–229. DOI: 10.1016/j.nimb.2006.04.003.

Ninomiya, S., Nakata, Y., Ichiki, K., Seki, T., Aoki, T., and Matsuo, J. (2007): "Measurements of Secondary Ions Emitted from Organic Compounds Bombarded with Large Gas Cluster Ions". In: *Nuclear Instruments and Methods in Physics Research Section B: Beam Interactions with Materials and Atoms* 256.1, pp. 493–496. DOI: 10.1016/j.nimb.2006.12.047.

Nobiling, R., Civelekoğlu, Y., Povh, B., Schwalm, D., and Traxel, K. (1975): "Collimation of Ion Beams to Micrometer Dimensions". In: *Nuclear Instruments and Methods* 130.2, pp. 325–334. DOI: 10.1016/0029-554X(75)90032-4.

Papaléo, R. M., Demirev, P., Eriksson, J., Håkansson, P., Sundqvist, B. U. R., and Johnson, R. E. (1996): "Measurement of MeV Ion Track Structure in an Organic Solid". In: *Physical Review Letters* 77.4, pp. 667–670. DOI: 10.1103/PhysRevLett.77.667.

Reimann, C. T. (1995): "Some Comments on Pressure-Pulse/Shock-Wave Desorption in a Real Material". In: *Nuclear Instruments and Methods in Physics Research Section B: Beam Interactions with Materials and Atoms* 95.2, pp. 181–191. DOI: 10.1016/0168-583X(94)00440-4.

Salehpour, M., Håkansson, P., Sundqvist, B., and Widdiyasekera, S. (1986): "Total Molecular Yields for Fast Heavy Ion Induced Desorption of Biomolecules". In: *Nuclear Instruments and Methods in Physics Research Section B: Beam Interactions with Materials and Atoms* 13.1, pp. 278–282. DOI: 10.1016/0168-583X(86)90514-8.

Säve, G., Håkansson, P., Sundqvist, B. U. R., and Jönsson, U. (1987): "Sample Film-Thickness Influence on Fast Heavy-Ion Induced Desorption Yields of Biomolecular Ions". In: *Nuclear Instruments and Methods in Physics Research Section B: Beam Interactions with Materials and Atoms* 26.4, pp. 571–577. DOI: 10.1016/0168-583X(87)90545-3.

Schulte-Borchers, M. (2016): "MeV SIMS Based on a Capillary Microprobe for Molecular Imaging". Doctoral Thesis. ETH Zurich. DOI: 10.3929/ethz-a-010736110.

Schulte-Borchers, M., Döbeli, M., Müller, A. M., George, M., and Synal, H.-A. (2016): "Time-of-Flight MeV-SIMS with Beam Induced Secondary Electron Trigger". In: *Nuclear Instruments and Methods in Physics Research Section B: Beam Interactions with Materials and Atoms* 380, pp. 94–98. DOI: 10.1016/j.nimb.2016.05.011.

Seiberling, L. E., Griffith, J. E., and Tombrello, T. A. (1980): "A Thermalized Ion Explosion Model for High Energy Sputtering and Track Registration". In: *Radiation Effects* 52.3-4, pp. 201–209. DOI: 10.1080/00337578008210033.

Seki, T., Kusakari, M., Fujii, M., Aoki, T., and Matsuo, J. (2016): "Ambient Analysis of Liquid Materials with Wet-SIMS". In: *Nuclear Instruments and Methods in Physics Research Section B: Beam Interactions with Materials and Atoms*. Proceedings of the 22nd International Conference on Ion Beam Analysis (IBA 2015) 371, pp. 189–193. DOI: 10.1016/j.nimb.2015.09.046.

Sekiba, D., Yonemura, H., Nebiki, T., Wilde, M., Ogura, S., Yamashita, H., Matsumoto, M., Kasagi, J., Iwamura, Y., Itoh, T., Matsuzaki, H., Narusawa, T., and Fukutani, K. (2008): "Development of Micro-Beam NRA for 3D-Mapping of Hydrogen Distribution in Solids: Application of Tapered Glass Capillary to 6 MeV 15N Ion". In: *Nuclear Instruments and*

Methods in Physics Research Section B: Beam Interactions with Materials and Atoms 266.18, pp. 4027–4036. DOI: 10.1016/j.nimb.2008.06.032.

Sigmund, P. (1969): "Theory of Sputtering. I. Sputtering Yield of Amorphous and Polycrystalline Targets". In: *Physical Review* 184.2, pp. 383–416. DOI: 10.1103/PhysRev.184.383.

Siketić, Z., Bogdanović Radović, I., Jakšić, M., Popović Hadžija, M., and Hadžija, M. (2015): "Submicron Mass Spectrometry Imaging of Single Cells by Combined Use of Mega Electron Volt Time-of-Flight Secondary Ion Mass Spectrometry and Scanning Transmission Ion Microscopy". In: *Applied Physics Letters* 107.9, p. 093702. DOI: 10.1063/1.4930062.

Simon, M. J., Zhou, C. L., Döbeli, M., Ikeda, T., Müller, A. M., Benyagoub, A., Grygiel, C., Guillous, S., Lebius, H., Mery, A., Monnet, I., Ropars, F., Shiromaru, H., and Cassimi, A. (2014): "Simulation of MeV Ion Transmission through Glass Micro-Capillaries". In: *Journal of Physics: Conference Series* 488.13, p. 132004. DOI: 10.1088/1742-6596/488/13/132004.

Simon, M. J., Döbeli, M., Müller, A. M., and Synal, H.-A. (2012): "In-Air STIM with a Capillary Microprobe". In: *Nuclear Instruments and Methods in Physics Research Section B: Beam Interactions with Materials and Atoms*. Proceedings of the 20th International Conference on Ion Beam Analysis 273, pp. 237–240. DOI: 10.1016/j.nimb.2011.07.084.

Simon, M. J., Zhou, C. L., Döbeli, M., Cassimi, A., Monnet, I., Méry, A., Grygiel, C., Guillous, S., Madi, T., Benyagoub, A., Lebius, H., Müller, A. M., Shiromaru, H., and Synal, H.-A. (2014): "Measurements and 3D Monte Carlo Simulation of MeV Ion Transmission through Conical Glass Capillaries". In: *Nuclear Instruments and Methods in Physics Research Section B: Beam Interactions with Materials and Atoms* 330, pp. 11–17. DOI: 10.1016/j.nimb.2014.03.016.

Simon, M. J. (2013): "Physikalische Grundlagen und Anwendungen einer Kapillaren - Mikrosonde". Doctoral Thesis. ETH Zurich. DOI: 10.3929/ethz-a-009796626.

Stoytschew, V., Bogdanović Radović, I., Demarche, J., Jakšić, M., Matjačić, L., Siketić, Z., and Webb, R. (2016): "MeV-SIMS Yield Measurements Using a Si-PIN Diode as a Primary Ion Current Counter". In: *Nuclear Instruments and Methods in Physics Research Section B: Beam Interactions with Materials and Atoms*. Proceedings of the 22nd International Conference on Ion Beam Analysis (IBA 2015) 371, pp. 194–198. DOI: 10.1016/j.nimb.2015.11.020.

Stoytschew, V., Bogdanović Radović, I., Siketić, Z., and Jakšić, M. (2017): "Influence of Experimental Parameters on Secondary Ion Yield for MeV-SIMS". In: *Nuclear Instruments and Methods in Physics Research Section B: Beam Interactions with Materials and Atoms*.

Proceedings of the 15th International Conference on Nuclear Microprobe Technology and Applications 404, pp. 110–113. DOI: 10.1016/j.nimb.2017.01.022.

Tadić, T., Bogdanović Radović, I., Siketić, Z., Cosic, D. D., Skukan, N., Jakšić, M., and Matsuo, J. (2014): "Development of a ToF SIMS Setup at the Zagreb Heavy Ion Microbeam Facility". In: *Nuclear Instruments and Methods in Physics Research Section B: Beam Interactions with Materials and Atoms*. Proceedings of the 21st International Conference on Ion Beam Analysis 332, pp. 234–237. DOI: 10.1016/j.nimb.2014.02.068.

Takáts, Z., Wiseman, J. M., Gologan, B., and Cooks, R. G. (2004): "Mass Spectrometry Sampling Under Ambient Conditions with Desorption Electrospray Ionization". In: *Science* 306.5695, pp. 471–473. DOI: 10.1126/science.1104404.

Tempez, A., Schultz, J. A., Della-Negra, S., Depauw, J., Jacquet, D., Novikov, A., Lebeyec, Y., Pautrat, M., Caroff, M., Ugarov, M., Bensaoula, H., Gonin, M., Fuhrer, K., and Woods, A. (2004): "Orthogonal Time-of-Flight Secondary Ion Mass Spectrometric Analysis of Peptides Using Large Gold Clusters as Primary Ions". In: *Rapid Communications in Mass Spectrometry* 18.4, pp. 371–376. DOI: 10.1002/rcm.1342.

Torgerson, D. F., Skowronski, R. P., and Macfarlane, R. D. (1974): "New Approach to the Mass Spectroscopy of Non-Volatile Compounds". In: *Biochemical and Biophysical Research Communications* 60.2, pp. 616–621. DOI: 10.1016/0006-291X(74)90285-X.

Toulemonde, M., Assmann, W., Dufour, C., Meftah, A., and Trautmann, C. (2012): "Nanometric Transformation of the Matter by Short and Intense Electronic Excitation: Experimental Data versus Inelastic Thermal Spike Model". In: *Nuclear Instruments and Methods in Physics Research Section B: Beam Interactions with Materials and Atoms*. Basic Research on Ionic-Covalent Materials for Nuclear Applications 277, pp. 28–39. DOI: 10.1016/j.nimb.2011.12.045.

Toulemonde, M., Assmann, W., Trautmann, C., and Grüner, F. (2002): "Jetlike Component in Sputtering of LiF Induced by Swift Heavy Ions". In: *Physical Review Letters* 88.5, p. 057602. DOI: 10.1103/PhysRevLett.88.057602.

Toulemonde, M., Paumier, E., and Dufour, C. (1993): "Thermal Spike Model in the Electronic Stopping Power Regime". In: *Radiation Effects and Defects in Solids* 126.1-4, pp. 201–206. DOI: 10.1080/10420159308219709.

Tsai, S.-T., Chen, C. W., Huang, L. C. L., Huang, M.-C., Chen, C.-H., and Wang, Y.-S. (2006): "Simultaneous Mass Analysis of Positive and Negative Ions Using a Dual-Polarity Time-of-Flight Mass Spectrometer". In: *Analytical Chemistry* 78.22, pp. 7729–7734. DOI: 10.1021/ac061213v.

Urbassek, H. M., Kafemann, H., and Johnson, R. E. (1994): "Atom Ejection from a Fast-Ion Track: A Molecular-Dynamics Study". In: *Physical Review B* 49.2, pp. 786–795. DOI: 10.1103/PhysRevB.49.786.

Urbassek, H. M. (1997): "Molecular-Dynamics Simulation of Sputtering". In: *Nuclear Instruments and Methods in Physics Research Section B: Beam Interactions with Materials and Atoms*. Nanometric Phenomena Induced by Laser, Ion and Cluster Beams 122.3, pp. 427–441. DOI: 10.1016/S0168-583X(96)00681-7.

Urbassek, M. and Sigmund, P. (1984): "A Note on Evaporation from Heated Spikes". In: *Applied Physics A* 35.1, pp. 19–25. DOI: 10.1007/BF00620295.

Verkhoturov, S. V., Gołuński, M., Verkhoturov, D. S., Czerwinski, B., Eller, M. J., Geng, S., Postawa, Z., and Schweikert, E. A. (2019): "Hypervelocity Cluster Ion Impacts on Free Standing Graphene: Experiment, Theory, and Applications". In: *The Journal of Chemical Physics* 150.16, p. 160901. DOI: 10.1063/1.5080606.

Vickerman, J. C. (2009): "Molecular Surface Mass Spectrometry by SIMS". In: *Surface Analysis – The Principal Techniques*. Ed. by J. C. Vickerman and I. S. Gilmore. John Wiley & Sons, Ltd, pp. 113–205. URL: http://onlinelibrary.wiley.com/doi/10.1002/9780470721582.ch4/summary (visited on 09/13/2016).

Voit, H., Frohlich, H., Duck, P., Nees, B., Nieschler, E., Bischof, W., and Tiereth, W. (1983): "Heavy Ion Induced Desorption of Biomolecules: Dependence on the Heavy Ion Parameters". In: *IEEE Transactions on Nuclear Science* 30.2, pp. 1759–1761. DOI: 10.1109/TNS.1983.4332635.

Westmore, J. B., Ens, W., and Standing, K. G. (1982): "Secondary Ion Mass Spectra of the Neuropeptides Leucine-Enkephalin and Methionine-Enkephalin". In: *Biomedical Mass Spectrometry* 9.3, pp. 119–124. DOI: 10.1002/bms.1200090309.

Widdiyasekera, S., Håkansson, P., and Sundqvist, B. U. R. (1988): "Initial Velocity Distributions of Secondary Ions in Electronic Sputtering of Biomolecules". In: *Nuclear Instruments and Methods in Physics Research Section B: Beam Interactions with Materials and Atoms* 33.1, pp. 836–839. DOI: 10.1016/0168-583X(88)90694-5.

Wien, K. (1989): "Fast Heavy Ion Induced Desorption". In: *Radiation Effects and Defects in Solids* 109.1-4, pp. 137–167. DOI: 10.1080/10420158908220529.

Ziegler, J. F., Biersack, J., and Littmark, U. (1985): *The Stopping and Range of Ions in Solids*. Vol. 1. New York.

Contributions

Present thesis

Unless otherwise mentioned, all work presented in this thesis was performed by myself. Some of the measurements in this thesis (for monoatomic primary ions species Au and Cu as well as Cu_n cluster ions) were performed together with Nicolas Brehm within the frame of his master thesis 'Yield and secondary ion fragmentation in MeV-SIMS' at ETH Zurich. All other measurements and the entire data analysis and interpretation was performed by myself.

Samples for measurements were provided by Prof. J. Matsuo, Kyoto University (arginine, leu-enkephalin and PEG), M. Oppliger and A. Stockklauser respectively the Quantum Device Lab group of Prof. A. Wallraff, D-PHYS ETH Zurich (Al/Au contact structure on GaAs) and M. Klöckner from the Laboratory Support Group at D-PHYS ETH Zurich (NaCl).

The initially used glass capillaries for collimation of the primary ion beam were produced and provided by M. Simon, ETH Zurich, who also instructed me on and helped with the capillary production process for the later used glass capillaries manufactured by myself. For the cutting of the capillaries microforge instruments provided by H. Spanke from the group for Soft and Living Materials of Prof. E. Dufresne, D-MATL ETH Zurich and M. Binelli from the group of Complex Materials of Prof. A.R. Studart, D-MATL ETH Zurich were used.

The mechanical construction of the ToF instrument and modifications to the instrument was performed in collaboration with J. Thut, LIP ETH Zurich. Custom parts were manufactured by the mechanical workshop of D-PHYS at ETH Zurich and installation and maintenance of the instrument was supported by R. Gruber, P. Vogel and A. Wagner, LIP ETH Zurich.

Publications

K.-U. Miltenberger et al. (2017): "MeV-SIMS Capillary Microprobe for Molecular Imaging". In: *Nuclear Instruments and Methods in Physics Research Section B: Beam Interactions with Materials and Atoms* 412, pp. 185–189. DOI: `10.1016/j.nimb.2017.09.024`

Conference contributions

Scientific Talks

Secondary ion yields in MeV-SIMS with heavy cluster ions
24th International Conference on Ion Beam Analysis, Antibes, France, October 2019

Secondary ion yield and fragmentation in MeV-SIMS performed on organic samples
Invited
25th International Conference on Applications of Accelerators in Research and Industry, Grapevine (TX), USA, August 2018

Exploring MeV-SIMS with a capillary microprobe
Annular DPG Spring Meeting (German Physical Society), Mainz, Germany, March 2017

Poster Presentations

A simultaneous dual-polarity ToF setup for MeV-SIMS
24th International Conference on Ion Beam Analysis, Antibes, France, October 2019

Exploring MeV-SIMS with CHIMP
Awarded 3rd place Best Poster Presentation
23rd International Conference on Ion Beam Analysis, Shanghai, China, October 2017

MeV-SIMS at ETH Zurich with CHIMP
Awarded Best Poster Presentation
Joint ICTP-IAEA Advanced Workshop on High Sensitivity 2D & 3D Characterization and Imaging with Ion Beams, Trieste, Italy, September 2016